

The US/UK World Magnetic Model for 2020-2025

Arnaud Chulliat
Patrick Alken
Manoj Nair
Adam Woods
Brian Meyer
Michael Paniccia (NGA)

William Brown
Ciarán Beggan
Grace Cox
Susan Macmillan

NOAA National Centers for
Environmental Information
325 Broadway
NOAA E/NE42
Boulder, CO 80305
USA

British Geological Survey
Geomagnetism Team
The Lyell Centre
Research Avenue South
Edinburgh, EH14 4AP
UK

Bibliographic Reference:

Chulliat, A., W. Brown, P. Alken, C. Beggan, M. Nair, G. Cox, A. Woods, S. Macmillan, B. Meyer and M. Paniccia, 2020. *The US/UK World Magnetic Model for 2020-2025: Technical Report*, National Centers for Environmental Information, NOAA. doi: [10.25923/ytk1-yx35](https://doi.org/10.25923/ytk1-yx35)



**British
Geological Survey**
Expert | Impartial | Innovative



ABSTRACT

This report contains a complete description of the World Magnetic Model (WMM) 2020. [Section 1](#) contains information that users of WMM2020 require in order to implement the model and software in navigation and heading systems, and to understand magnetic charts, poles and geomagnetic coordinate systems. [Section 2](#) contains a detailed summary of the data used and the modeling techniques employed. [Section 3](#) contains an assessment of the model uncertainties and a description of the error model provided with the WMM2020. [Section 4](#) contains charts of all the magnetic elements at 2020.0 and their expected annual rates of change between 2020.0 and 2025.0. These predicted changes are based upon the best knowledge of the geomagnetic main field evolution at the time the WMM was released.

Sponsored by the U.S. National Geospatial-Intelligence Agency (NGA) and the U.K. Defence Geographic Centre (DGC), the World Magnetic Model (WMM) is produced by the U.S. National Oceanic and Atmospheric Administration's National Centers for Environmental Information (NOAA/NCEI) and the British Geological Survey (BGS). It is the standard model used by the U.S. Department of Defense (DoD), the U.K. Ministry of Defence, the North Atlantic Treaty Organization (NATO) and the International Hydrographic Organization (IHO), for navigation, attitude and heading referencing systems using the geomagnetic field. It is also used widely in civilian navigation and heading systems.

The WMM2020 product release includes several software items by which the WMM2020 model may be computed and/or its subroutines incorporated into larger DoD systems. It is hoped that the software provided is useful for most occasions of DoD systems procurement and development.

CONTACTS

The model, associated software, digital charts and documentation are available at <https://www.ngdc.noaa.gov/geomag/WMM/> or by contacting NCEI, BGS, or NGA.

Please cite using these identifiers. Recommended usage and additional information available at:

Technical Report – doi: [10.25923/ytk1-yx35](https://doi.org/10.25923/ytk1-yx35)

Dataset – doi: [10.25921/11v3-da71](https://doi.org/10.25921/11v3-da71)

MODEL AND SOFTWARE SUPPORT

National Centers for Environmental Information

NOAA E/NE42
325 Broadway
Boulder, CO 80305
USA
Attention: Manoj Nair or Arnaud Chulliat
Phone: + (303) 497-4642 or -6522
Email: geomag.models@noaa.gov
Web: <https://www.ngdc.noaa.gov/geomag/WMM/>

British Geological Survey

The Lyell Centre
Research Avenue South
Edinburgh, EH14 4AP
UK
Attention: Susan Macmillan or William Brown
Phone: + 44 131 667 1000
Email: smac@bgs.ac.uk or wb@bgs.ac.uk
Web: <https://geomag.bgs.ac.uk/research/modelling/WorldMagneticModel.html>

APPLICABILITY WITHIN THE U.S. DEPARTMENT OF DEFENSE

National Geospatial-Intelligence Agency

Geomatics Office
NGA-SN, Mail Stop L-41
3838 Vogel Road
Arnold, MO 63010-6238
U.S.A.

Email: WGS84@nga.mil

APPLICABILITY WITHIN THE U.K. MINISTRY OF DEFENCE

Defence Geographic Centre

MacLeod Building, Elmwood Avenue
Feltham
Middlesex, TW13 7AH
UK

Chris Mundy
Email: Chris.Mundy601@mod.gov.uk

Matthew Shimell
Email: Matthew.Shimell113@mod.gov.uk

Giles André
Email: Giles.Andre562@mod.gov.uk

The NATO and military specifications for magnetic models are STANAG 7172 (NATO Standardization Agency, 2011) and MIL-PRF-89500B (Department of Defense, 2019). Magnetic model requirements that are more stringent than those set forth in these specifications should be addressed to NCEI and BGS (e.g., those that must include magnetic effects of the Earth’s crust, ionosphere, or magnetosphere and/or require greater spatial or temporal resolution on a regional or local basis).

ACKNOWLEDGEMENTS

This work was carried out under the sponsorship of the U.S. National Geospatial-Intelligence Agency (NGA) and the UK Ministry of Defence, Defence Geographic Centre (DGC). The maps of the geomagnetic elements were designed by Jesse Varner (NOAA/NCEI and Cooperative Institute for Research in the Environmental Sciences, University of Colorado Boulder). Thank you to Barbara Ambrose in the NCEI Communications team for helping with the formatting and for making sure this document is accessible by people with disabilities. Eric Kihn (NOAA/NCEI) is the U.S. manager for the WMM project, which is funded by NGA. NGA personnel oversee the WMM development, reviewed this report and contributed to the error analysis. Data from the Swarm satellite mission were provided by the European Space Agency (ESA), supported by ESA member states. Many institutes and agencies are involved in the operation of geomagnetic observatories around the world. In particular we would like to thank: Centre de Recherche en Astronomie Astrophysique et Geophysique, ALGERIA; Servicio Meteorologico Nacional, ARGENTINA; Universidad Nacional de la Plata, ARGENTINA; Geoscience Australia, AUSTRALIA; Zentralanstalt für Meteorologie und Geodynamik, AUSTRIA; Institut Royal Météorologique de Belgique, BELGIUM; CNPq-Observatório Nacional, BRAZIL; Academy of Sciences,

BULGARIA; Natural Resources Canada, CANADA; Centro Meteorológico Regional Pacifico, CHILE; Academy of Sciences, CHINA; China Earthquake Administration, CHINA; Instituto Geográfico Agustín Codazzi, COLOMBIA; University of Zagreb, CROATIA; Academy of Sciences, CZECH REPUBLIC; Danish Technical University, DENMARK; Addis Ababa University, ETHIOPIA; Finnish Meteorological Institute, FINLAND; Sodankylä Geophysical Observatory, FINLAND; Institut de Physique du Globe de Paris, FRANCE; Ecole et Observatoire des Sciences de la Terre, FRANCE; Ludwig Maximilians University Munich, GERMANY; Alfred-Wegener-Institute for Polar & Marine Research, GERMANY; Helmholtz Centre Potsdam, GERMANY; Universities of Karlsruhe and Stuttgart, GERMANY; Institute of Geology and Mineral Exploration, GREECE; Academy of Sciences, HUNGARY; Eötvös Loránd Geophysical Institute of Hungary, HUNGARY; University of Iceland, ICELAND; Indian Institute of Geomagnetism, INDIA; National Geophysical Research Institute, INDIA; Meteorological and Geophysical Agency, INDONESIA; The Irish Meteorological Service, IRELAND; Survey of Israel, ISRAEL; Instituto Nazionale di Geofisica e Vulcanologia, ITALY; Japan Coast Guard, JAPAN; Japan Meteorological Agency, JAPAN; Geographical Survey Institute, JAPAN; Institute of the Ionosphere, KAZAKHSTAN; Korean Meteorological Administration, KOREA; National Centre for Geophysical Research, LEBANON; Université d'Antananarivo, MADAGASCAR; Gan Meteorological Office, MALDIVES; Institute of Geological and Nuclear Sciences, NEW ZEALAND; University of Tromsø, NORWAY; Instituto Geofísico del Perú, PERU; Academy of Sciences, POLAND; Instituto Nacional de Geología, REPÚBLICA DE MOÇAMBIQUE; Geological Survey of Romania, ROMANIA; Academy of Sciences, RUSSIA; Institute of Solar-Terrestrial Physics, RUSSIA; Dept. of Agriculture, Forestry, Fisheries & Meteorology, SAMOA; Geomagnetic College Grocka, SERBIA & MONTENEGRO; Slovenska Akademia Vied, SLOVAKIA; National Research Foundation, SOUTH AFRICA; Observatori de l'Ebre, SPAIN; Real Instituto y Observatorio de la Armada, SPAIN; Instituto Geográfico Nacional, SPAIN; Sveriges Geologiska Undersökning, SWEDEN; Swedish Institute of Space Physics, SWEDEN; ETH Zurich, SWITZERLAND; Earthquake Research Institute, TURKEY; US Geological Survey, UNITED STATES OF AMERICA; British Geological Survey, UNITED KINGDOM; Academy of Sciences, UKRAINE; Ukrainian Antarctic Center, UKRAINE and National Centre for Science and Technology, VIETNAM. The INTERMAGNET program and ICSU World Data System (primarily the World Data Centre for Geomagnetism, Edinburgh) assist in the quality control and dissemination of observatory data. The magnetic activity indices Kp and Dst were computed and provided by Helmholtz Centre Potsdam (GFZ), Germany and World Data Center for Geomagnetism in Kyoto, respectively. We acknowledge use of NASA/GSFC's Space Physics Data Facility's ftp service, and OMNI data, particularly measurements from the NASA/ACE and NOAA/DSCOVR missions. This model could not have been produced without the efforts of all of these institutes.

TABLE OF CONTENTS

Abstract	i
Contacts	ii
Acknowledgements	iii
Table of Contents	v
1. The Model	1
1.1 Introduction	1
1.1.1 Magnetic Elements	2
1.1.2 Grid Variation	3
1.1.3 Range of the Magnetic Elements at the Earth's Surface	5
1.2 Relevant Model Equations	6
1.3 The WMM2020 Coefficients	12
1.4 Singularities at the Geographic Poles	13
1.5 Model Equations Numerical Example	14
1.6 Magnetic Poles and Geomagnetic Coordinate Systems	16
1.7 Blackout Zones	18
1.8 Supersession of the Models	21
1.9 Policy on Alternate Software for the U.S. Department of Defense	21
1.10 Description of Charts	22
1.11 Software, Online Calculators and Test Values	23
2. Construction of the Model	25
2.1 Background on the Geomagnetic Field	25
2.2 Data Acquisition and Quality Control	27
2.2.1 Satellite Data	27
2.2.2 Observatory Data	31
2.2.3 Other Data and Derived Products	37
2.3 Derivation of the Model	40
2.3.1 NCEI Extended Parent Model	41
2.3.2 BGS Extended Parent Model	44
2.3.3 Validation Process	48
3. Model Uncertainties	49
3.1 Sources of Uncertainty	49
3.2 Estimating Uncertainty	51
3.2.1 Formal Commission Error	51
3.2.2 Commission Error From Model Comparisons	52
3.2.3 Crustal Field Contribution – Method #1	58
3.2.4 Crustal Field Contribution – Method #2	61
3.2.5 Disturbance Field Contribution	64
3.3 Total Error Budget	66
3.4 Error Model	67
4. Charts	70
5. References and Bibliography	111

1. THE MODEL

1.1 INTRODUCTION

The Earth is like a giant magnet. At every location on or above the Earth, its magnetic field has a more or less well-known direction, which can be used to orient ships, aircraft, satellites, antennas, drilling equipment and handheld devices. At some places on the globe the horizontal direction of the magnetic field coincides with the direction of geographic north (“true” north), but in general this is not the case. The angular amount by which the horizontal direction of the magnetic field differs from true north is called the magnetic declination, or simply declination (D , see Figure 1). This is the correction required to convert between a magnetic bearing and a true bearing. The main utility of the World Magnetic Model (WMM) is to provide magnetic declination for any desired location on the globe. In addition to the magnetic declination, the WMM also provides the complete geometry of the field from 1 km below the World Geodetic System (WGS 84) ellipsoid surface to approximately 850 km above it (MIL-PRF-89500B, Department of Defense, 2019). The magnetic field extends deep into the Earth and far out into space, but the WMM is not valid at these extremes.

The Earth’s magnetism has several sources. All sources affect a scientific or navigational instrument but only some are represented in the WMM. The strongest contribution, by far, is the magnetic field produced by the Earth’s liquid-iron outer core, called the “core field”. Magnetic minerals in the crust and upper mantle make a further contribution that can be locally significant. Electric currents induced by the flow of conducting sea water through the ambient magnetic field make a further, albeit weak, contribution to the observed magnetic field. All of these are of “internal” origin and their large-scale components (see below) are included in the WMM. Deliberately excluded from the WMM by the data selection process and by other means (e.g., model co-estimation) are so-called “disturbance fields”. These are contributions arising from electric currents in the upper atmosphere and near-Earth space. These “external” magnetic fields are time-varying, and have a further effect. They induce electric currents in the Earth and oceans, producing secondary internal magnetic fields, which are considered part of the disturbance field and are not represented in the WMM.

The mathematical representation of the WMM is an expansion of the magnetic potential into spherical harmonic functions to degree and order 12. The minimum wavelength resolved is $360^\circ / \sqrt{12 \times 13} = 28.8^\circ$ in arc-length, corresponding to 3200 km at the Earth's surface (see section 3.6.3 of Backus et al., 1996). The WMM is a model of those internal magnetic fields that are not part of the disturbance field and have spatial wavelengths exceeding 30° in arc-length. This works out to be almost the entire core field and the long-wavelength portion of the crustal and oceanic fields. In this report, the term “main field” refers to the portion of the Earth's magnetic field at epoch 2020.0 that is modeled by the WMM.

The core field changes perceptibly from year to year. This effect, called secular variation (SV), is accounted for in the WMM by a linear SV model. Specifically, a straight line is used as the model of the time-dependence of each coefficient of the spherical harmonic representation of the magnetic potential (see [section 1.2](#)). Due to unpredictable non-linear changes in the core field, the values of the WMM coefficients have to be updated every five years. The revision described in this report, WMM2020, is valid from 2020.0 to 2025.0.

1.1.1 MAGNETIC ELEMENTS

The geomagnetic field vector, \mathbf{B}_m , is described by seven elements. These are the northerly intensity X , the easterly intensity Y , the vertical intensity Z (positive downwards) and the following quantities derived from X , Y and Z : the horizontal intensity H , the total intensity F , the inclination angle I , (also called the dip angle and measured from the horizontal plane to the field vector, positive downwards) and the declination angle D (also called the magnetic variation and measured clockwise from true north to the horizontal component of the field vector). In the descriptions of X , Y , Z , H , F , I and D above, the vertical direction is perpendicular to the WGS 84 ellipsoid model of the Earth, the horizontal plane is perpendicular to the vertical direction, and the rotational directions clockwise and counter-clockwise are determined by a view from above (see Figure 1).

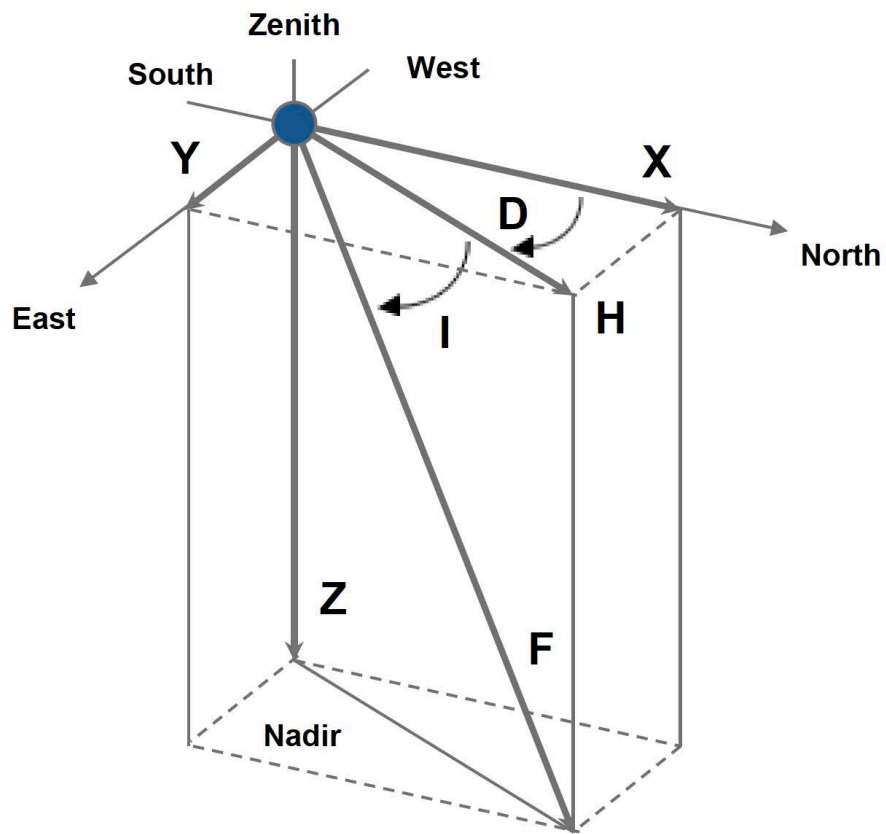


Figure 1: The seven elements of the geomagnetic field vector \mathbf{B}_m associated with an arbitrary point in space.

The quantities X , Y and Z are the sizes of perpendicular vectors that add vectorially to \mathbf{B}_m . Conversely, X , Y and Z can be determined from the quantities F , I and D (i.e., the quantities that specify the size and direction of \mathbf{B}_m).

1.1.2 GRID VARIATION

In the polar regions, or near the rotation axis of the Earth, the angle D changes strongly with a change in the longitude of the observer, and is therefore a poor measure of the direction of \mathbf{B}_m . For this reason, the WMM specification (MIL-PRF-89500B, Department of Defense, 2019) defines two

auxiliary angles, called grid variation north (GV_N) and south (GV_S), for the direction of \mathbf{B}_m in the horizontal plane in each polar region. Their definitions are:

$$\begin{aligned}GV_N &= D - \lambda \quad \text{for } \varphi > 55^\circ \\GV_S &= D + \lambda \quad \text{for } \varphi < -55^\circ\end{aligned}\tag{1}$$

where λ is the longitude and φ is the geodetic latitude.

The quantities GV_N and GV_S defined above are examples of a more general concept, namely grid variation (also called grid magnetic angle or grivation). At a location on the plane of a chosen horizontal grid coordinate system, grivation is the angle between grid north and magnetic north, i.e., the angle measured clockwise from the direction parallel to the grid's Northing axis to the horizontal component of the magnetic field at the observer's location. Grivation is useful for local surveys, where location is given by grid coordinates rather than by longitude and latitude. It is dependent on the map projection used to define the grid coordinates. In general, it is

$$GV_{grid} = D - C\tag{2}$$

where D is the magnetic declination and C is the "convergence-of-meridians" defined as the clockwise angle from the northward meridional arc to the grid Northing direction.

For example, large scale military topographic mapping routinely employs the Universal Transverse Mercator (UTM) grid coordinates for the map projection of the sheet, for the definition of a grid to overprint, and for a grivation calculation as defined above. Above 84°N and below 80°S , it employs the Universal Polar Stereographic (UPS) grid. For these two grids, the grid variation could be notated GV_{UTM} and GV_{UPS} , respectively.

In the WMM subroutine library, both GV_{UPS} and GV_{UTM} are provided within certain restrictions (see the software user's guide, <https://www.ngdc.noaa.gov/geomag/WMM/soft.shtml>).

1.1.3 RANGE OF THE MAGNETIC ELEMENTS AT THE EARTH'S SURFACE

Table 1 shows the expected range of the magnetic field elements and *GV* at the Earth's surface.

Table 1: Ranges of magnetic elements and *GV* at the Earth's surface.

Element	Name	Alternative Name	Range at Earth's Surface			
<i>X</i>	North component	Northerly intensity	-17000	43000	nT	North
<i>Y</i>	East component	Easterly intensity	-18000	17000	nT	East
<i>Z</i>	Down component	Vertical intensity	-67000	62000	nT	Down
<i>H</i>	Horizontal intensity		0	43000	nT	
<i>F</i>	Total intensity	Total field	23000	67000	nT	
<i>I</i>	Inclination	Dip	-90	90	Degree	Down
<i>D</i>	Declination	Magnetic variation	-180	180	Degree	East / Clockwise
<i>GV</i>	Grid variation	Grivation	-180	180	Degree	East / Clockwise

1.2 RELEVANT MODEL EQUATIONS

This section describes the representation of the magnetic field in the WMM and lists the equations needed to obtain the magnetic field elements for the desired location and time from the WMM coefficients. All variables in this section adhere to the following measurement conventions: angles are in radians, lengths are in meters, magnetic intensities are in nanoteslas (nT, where one tesla is one weber per square meter or one kg.s⁻².A⁻¹) and times are in years. The software may display these quantities in other units, which it will identify.

The main magnetic field \mathbf{B}_m is a potential field and therefore can be written in geocentric spherical coordinates (longitude λ , latitude φ' , radius r) as the negative spatial gradient of a scalar potential

$$\mathbf{B}_m(\lambda, \varphi', r, t) = -\nabla V(\lambda, \varphi', r, t) \quad (3)$$

where t is the time. This potential can be expanded in terms of spherical harmonics:

$$V(\lambda, \varphi', r, t) = a \sum_{n=1}^N \left(\frac{a}{r}\right)^{n+1} \sum_{m=0}^n (g_n^m(t) \cos(m\lambda) + h_n^m(t) \sin(m\lambda)) \check{P}_n^m(\sin \varphi') \quad (4)$$

where $N=12$ is the degree of the expansion of the WMM, a (6371200 m) is the geomagnetic reference radius (which is close to the mean Earth radius), (λ, φ', r) are the longitude, latitude and radius in a spherical geocentric reference frame, and $g_n^m(t)$ and $h_n^m(t)$ are the time-dependent Gauss coefficients of degree n and order m describing the Earth's main magnetic field. For any real number μ , $\check{P}_n^m(\mu)$ are the Schmidt semi-normalized associated Legendre functions defined as:

$$\begin{aligned} \check{P}_n^m(\mu) &= \sqrt{2 \frac{(n-m)!}{(n+m)!}} P_{n,m}(\mu) \text{ if } m > 0 \\ \check{P}_n^m(\mu) &= P_{n,m}(\mu) \text{ if } m = 0 \end{aligned} \quad (5)$$

Here, the definition of $P_{n,m}(\mu)$ is commonly used in geodesy and geomagnetism (e.g., Heiskanen and Moritz, 1967, equation 1-60; Langel, 1987, equation 8). Sample functions, for geocentric latitude φ' , are:

$$\begin{aligned}
 P_{3,0}(\sin \varphi') &= \frac{1}{2}(\sin \varphi')(5 \sin^2 \varphi' - 3) \\
 P_{3,1}(\sin \varphi') &= -\frac{3}{2}(\cos \varphi')(1 - 5 \sin^2 \varphi') \\
 P_{3,2}(\sin \varphi') &= 15(\sin \varphi')(1 - \sin^2 \varphi') \\
 P_{3,3}(\sin \varphi') &= 15 \cos^3 \varphi'
 \end{aligned} \tag{6}$$

These $P_{n,m}(\mu)$ are related to the $P_n^m(\mu)$ defined in Abramowitz and Stegun (1972, Chapter 8) or Gradshteyn and Ryzhik (1994, Chapter 8.7) by $P_{n,m}(\mu) = (-1)^m P_n^m(\mu)$.

WMM2020 comprises two sets of Gauss coefficients to degree and order $N=12$. One set provides a spherical harmonic main field model for 2020.0 in units of nT, the other set provides a predictive secular variation model for the period 2020.0 to 2025.0 in units of nT/year. The secular variation model was derived from geomagnetic data prior to 2020.0. Specifically, it is the average of two models: one representing the average change of the main field over a year starting at 2018.5; the other representing the extrapolated change of the main field in 2020.0. However, this represents our best knowledge of the geomagnetic main field evolution at the time of the WMM release, and is expected to yield geomagnetic main field values within defined uncertainty parameters for the lifetime of the model.

A step by step procedure is provided below for computing the magnetic field elements at a given location and time $(\lambda, \varphi, h_{MSL}, t)$, where λ and φ are the longitude and geodetic latitude, h_{MSL} is height above Mean Sea Level (MSL), and t is the time given in decimal years.

In the first step, the user provides the time, location and height above MSL at which the magnetic elements are to be calculated. The height above MSL is then converted to height h above the WGS 84 ellipsoid by using the geopotential model EGM96 (Lemoine et al., 1998). This is accomplished by interpolating a grid of the geoid height file with a spatial resolution of 15 arc-minutes. This stage of converting height above MSL to height above the WGS 84 ellipsoid has a very small effect on the resulting magnetic field values (of the order of 1 nT or less) and is unnecessary in the majority of implementations. Note that the user can also directly enter the height above the WGS 84 ellipsoid into the software.

The geodetic coordinates (λ, φ, h) are then transformed into spherical geocentric coordinates (λ, φ', r) by recognizing that λ is the same in both coordinate systems, and that (φ', r) is computed from (φ, h) according to the equations:

$$\begin{aligned}
 p &= (R_c + h) \cos \varphi \\
 z &= (R_c(1 - e^2) + h) \sin \varphi \\
 r &= \sqrt{p^2 + z^2} \\
 \varphi' &= \arcsin \frac{z}{r}
 \end{aligned} \tag{7}$$

Here, $p = \sqrt{x^2 + y^2}$, where x , y and z are the coordinates of a geocentric Cartesian coordinate system in which the positive x and z axes point in the directions of the prime meridian ($\lambda=0$) and the Earth's rotation axis, respectively. The semi-major axis A , reciprocal flattening $1/f$, eccentricity squared e^2 and radius of curvature of the prime vertical (also called normal section) R_c at the given latitude φ are given for the WGS 84 ellipsoid as

$$\begin{aligned}
 A &= 6378137 \text{ m} \\
 \frac{1}{f} &= 298.257223563 \\
 e^2 &= f(2 - f)
 \end{aligned} \tag{8}$$

$$R_c = \frac{A}{\sqrt{1 - e^2 \sin^2 \varphi}}$$

In the second step, the Gauss coefficients $g_n^m(t)$ and $h_n^m(t)$ are determined for the desired time t from the model coefficients $g_n^m(t_0)$, $h_n^m(t_0)$, $\dot{g}_n^m(t_0)$ and $\dot{h}_n^m(t_0)$ as

$$\begin{aligned} g_n^m(t) &= g_n^m(t_0) + (t - t_0) \dot{g}_n^m(t_0) \\ h_n^m(t) &= h_n^m(t_0) + (t - t_0) \dot{h}_n^m(t_0) \end{aligned} \quad (9)$$

where the time is given in decimal years and $t_0 = 2020.0$, the reference epoch of the model. The quantities $g_n^m(t_0)$ and $h_n^m(t_0)$ are called the main field coefficients and the quantities $\dot{g}_n^m(t_0)$ and $\dot{h}_n^m(t_0)$ are called the secular variation coefficients.

In the third step, the field vector components X' , Y' and Z' in geocentric coordinates are computed as

$$\begin{aligned} X'(\lambda, \varphi', r) &= -\frac{1}{r} \frac{\partial V}{\partial \varphi'} \\ &= -\sum_{n=1}^{12} \left(\frac{a}{r}\right)^{n+2} \sum_{m=0}^n (g_n^m(t) \cos m\lambda + h_n^m(t) \sin m\lambda) \frac{d\check{P}_n^m(\sin \varphi')}{d\varphi'} \end{aligned} \quad (10)$$

$$\begin{aligned} Y'(\lambda, \varphi', r) &= -\frac{1}{r \cos \varphi'} \frac{\partial V}{\partial \lambda} \\ &= \frac{1}{\cos \varphi'} \sum_{n=1}^{12} \left(\frac{a}{r}\right)^{n+2} \sum_{m=0}^n m (g_n^m(t) \sin m\lambda - h_n^m(t) \cos m\lambda) \check{P}_n^m(\sin \varphi') \end{aligned} \quad (11)$$

$$\begin{aligned}
Z'(\lambda, \varphi', r) &= \frac{\partial V}{\partial r} \\
&= -\sum_{n=1}^{12} (n+1) \left(\frac{a}{r}\right)^{n+2} \sum_{m=0}^n (\dot{g}_n^m(t) \cos m\lambda + \dot{h}_n^m(t) \sin m\lambda) \check{P}_n^m(\sin \varphi')
\end{aligned} \tag{12}$$

At this point, the secular variation of the field components can be computed as

$$\begin{aligned}
\dot{X}'(\lambda, \varphi', r) &= -\frac{1}{r} \frac{\partial \dot{V}}{\partial \varphi'} \\
&= -\sum_{n=1}^{12} \left(\frac{a}{r}\right)^{n+2} \sum_{m=0}^n (\dot{g}_n^m \cos m\lambda + \dot{h}_n^m \sin m\lambda) \frac{d\check{P}_n^m(\sin \varphi')}{d\varphi'}
\end{aligned} \tag{13}$$

$$\begin{aligned}
\dot{Y}'(\lambda, \varphi', r) &= -\frac{1}{r \cos \varphi'} \frac{\partial \dot{V}}{\partial \lambda} \\
&= \frac{1}{\cos \varphi'} \sum_{n=1}^{12} \left(\frac{a}{r}\right)^{n+2} \sum_{m=0}^n m (\dot{g}_n^m \sin m\lambda - \dot{h}_n^m \cos m\lambda) \check{P}_n^m(\sin \varphi')
\end{aligned} \tag{14}$$

$$\begin{aligned}
\dot{Z}'(\lambda, \varphi', r) &= \frac{\partial \dot{V}}{\partial r} \\
&= -\sum_{n=1}^{12} (n+1) \left(\frac{a}{r}\right)^{n+2} \sum_{m=0}^n (\dot{g}_n^m \cos m\lambda + \dot{h}_n^m \sin m\lambda) \check{P}_n^m(\sin \varphi')
\end{aligned} \tag{15}$$

$$\frac{d\check{P}_n^m(\sin \varphi')}{d\varphi'} = (n+1)(\tan \varphi') \check{P}_n^m(\sin \varphi') - \sqrt{(n+1)^2 - m^2} (\sec \varphi') \check{P}_{n+1}^m(\sin \varphi') \tag{16}$$

In the fourth step, the geocentric magnetic field vector components X' , Y' and Z' , are rotated into the ellipsoidal reference frame, using

$$\begin{aligned}
X &= X' \cos(\varphi' - \varphi) - Z' \sin(\varphi' - \varphi) \\
Y &= Y' \\
Z &= X' \sin(\varphi' - \varphi) + Z' \cos(\varphi' - \varphi)
\end{aligned} \tag{17}$$

Similarly, the time derivatives of the vector components, \dot{X} , \dot{Y} and \dot{Z} are rotated using

$$\begin{aligned}
\dot{X} &= \dot{X}' \cos(\varphi' - \varphi) - \dot{Z}' \sin(\varphi' - \varphi) \\
\dot{Y} &= \dot{Y}' \\
\dot{Z} &= \dot{X}' \sin(\varphi' - \varphi) + \dot{Z}' \cos(\varphi' - \varphi)
\end{aligned} \tag{18}$$

In the last step, the magnetic elements H , F , I and D are computed from the orthogonal components:

$$H = \sqrt{X^2 + Y^2}, \quad F = \sqrt{H^2 + Z^2}, \quad I = \arctan(Z, H), \quad D = \arctan(Y, X) \tag{19}$$

where $\arctan(a, b)$ is $\tan^{-1}(a/b)$, taking into account the angular quadrant, avoiding a division by zero, and resulting in a declination in the range of $-\pi$ to π and an inclination in the range of $-\pi/2$ to $\pi/2$. These angles in radians are then output by the WMM software in degrees.

The secular variation of these elements is computed using

$$\begin{aligned}
\dot{H} &= \frac{X \cdot \dot{X} + Y \cdot \dot{Y}}{H} \\
\dot{F} &= \frac{X \cdot \dot{X} + Y \cdot \dot{Y} + Z \cdot \dot{Z}}{F} \\
\dot{I} &= \frac{H \cdot \dot{Z} - Z \cdot \dot{H}}{F^2} \\
\dot{D} &= \frac{X \cdot \dot{Y} - Y \cdot \dot{X}}{H^2} \\
G\dot{V} &= \dot{D}
\end{aligned} \tag{20}$$

where \dot{I} , \dot{D} and $G\dot{V}$ are given in radians per year. The WMM software then outputs these angles in arc-minutes per year or decimal degrees per year.

1.3 THE WMM2020 COEFFICIENTS

The model coefficients, also referred to as Gauss coefficients, are listed in Table 2. These coefficients can be used to compute values for the field elements and their annual rates of change at any location near the surface of the Earth, and at any date between 2020.0 and 2025.0.

Table 2: Final coefficients for WMM2020. Units are nT for the main field, and nT per year for the secular variation. The index n is the degree and m is the order. Since $h_n^m(t_0)$ and $\dot{h}_n^m(t_0)$ are not defined for $m = 0$, the corresponding fields are left blank. (The corresponding coefficients are set to zero in the WMM2020 coefficient file.)

n	m	$g_n^m(t_0)$	$h_n^m(t_0)$	$\dot{g}_n^m(t_0)$	$\dot{h}_n^m(t_0)$
1	0	-29404.5		6.7	
1	1	-1450.7	4652.9	7.7	-25.1
2	0	-2500.0		-11.5	
2	1	2982.0	-2991.6	-7.1	-30.2
2	2	1676.8	-734.8	-2.2	-23.9
3	0	1363.9		2.8	
3	1	-2381.0	-82.2	-6.2	5.7
3	2	1236.2	241.8	3.4	-1.0
3	3	525.7	-542.9	-12.2	1.1
4	0	903.1		-1.1	
4	1	809.4	282.0	-1.6	0.2
4	2	86.2	-158.4	-6.0	6.9
4	3	-309.4	199.8	5.4	3.7
4	4	47.9	-350.1	-5.5	-5.6
5	0	-234.4		-0.3	
5	1	363.1	47.7	0.6	0.1
5	2	187.8	208.4	-0.7	2.5
5	3	-140.7	-121.3	0.1	-0.9
5	4	-151.2	32.2	1.2	3.0
5	5	13.7	99.1	1.0	0.5
6	0	65.9		-0.6	
6	1	65.6	-19.1	-0.4	0.1
6	2	73.0	25.0	0.5	-1.8
6	3	-121.5	52.7	1.4	-1.4
6	4	-36.2	-64.4	-1.4	0.9
6	5	13.5	9.0	0.0	0.1
6	6	-64.7	68.1	0.8	1.0
7	0	80.6		-0.1	
7	1	-76.8	-51.4	-0.3	0.5
7	2	-8.3	-16.8	-0.1	0.6
7	3	56.5	2.3	0.7	-0.7
7	4	15.8	23.5	0.2	-0.2
7	5	6.4	-2.2	-0.5	-1.2
7	6	-7.2	-27.2	-0.8	0.2
7	7	9.8	-1.9	1.0	0.3
8	0	23.6		-0.1	
8	1	9.8	8.4	0.1	-0.3
8	2	-17.5	-15.3	-0.1	0.7
8	3	-0.4	12.8	0.5	-0.2
8	4	-21.1	-11.8	-0.1	0.5
8	5	15.3	14.9	0.4	-0.3
8	6	13.7	3.6	0.5	-0.5
8	7	-16.5	-6.9	0.0	0.4
8	8	-0.3	2.8	0.4	0.1
9	0	5.0		-0.1	

n	m	$g_n^m(t_0)$	$h_n^m(t_0)$	$\dot{g}_n^m(t_0)$	$\dot{h}_n^m(t_0)$
9	1	8.2	-23.3	-0.2	-0.3
9	2	2.9	11.1	0.0	0.2
9	3	-1.4	9.8	0.4	-0.4
9	4	-1.1	-5.1	-0.3	0.4
9	5	-13.3	-6.2	0.0	0.1
9	6	1.1	7.8	0.3	0.0
9	7	8.9	0.4	0.0	-0.2
9	8	-9.3	-1.5	0.0	0.5
9	9	-11.9	9.7	-0.4	0.2
10	0	-1.9		0.0	
10	1	-6.2	3.4	0.0	0.0
10	2	-0.1	-0.2	0.0	0.1
10	3	1.7	3.5	0.2	-0.3
10	4	-0.9	4.8	-0.1	0.1
10	5	0.6	-8.6	-0.2	-0.2
10	6	-0.9	-0.1	0.0	0.1
10	7	1.9	-4.2	-0.1	0.0
10	8	1.4	-3.4	-0.2	-0.1
10	9	-2.4	-0.1	-0.1	0.2
10	10	-3.9	-8.8	0.0	0.0
11	0	3.0		0.0	
11	1	-1.4	0.0	-0.1	0.0
11	2	-2.5	2.6	0.0	0.1
11	3	2.4	-0.5	0.0	0.0
11	4	-0.9	-0.4	0.0	0.2
11	5	0.3	0.6	-0.1	0.0
11	6	-0.7	-0.2	0.0	0.0
11	7	-0.1	-1.7	0.0	0.1
11	8	1.4	-1.6	-0.1	0.0
11	9	-0.6	-3.0	-0.1	-0.1
11	10	0.2	-2.0	-0.1	0.0
11	11	3.1	-2.6	-0.1	0.0
12	0	-2.0		0.0	
12	1	-0.1	-1.2	0.0	0.0
12	2	0.5	0.5	0.0	0.0
12	3	1.3	1.3	0.0	-0.1
12	4	-1.2	-1.8	0.0	0.1
12	5	0.7	0.1	0.0	0.0
12	6	0.3	0.7	0.0	0.0
12	7	0.5	-0.1	0.0	0.0
12	8	-0.2	0.6	0.0	0.1
12	9	-0.5	0.2	0.0	0.0
12	10	0.1	-0.9	0.0	0.0
12	11	-1.1	0.0	0.0	0.0
12	12	-0.3	0.5	-0.1	-0.1

1.4 SINGULARITIES AT THE GEOGRAPHIC POLES

The World Magnetic Model has singularities at the North and South geographic poles. This is a mathematical issue, not a geophysical phenomenon, stemming from the ambiguity of longitude at a Pole and at any altitude over a Pole. Related to this, the North-East-Down (NED) frame of unit vectors to which the X' , Y' , Z' quantities are referred is defined everywhere except at or over a Pole. This section extends these concepts. The North Pole is discussed in the following, with similar implications for the South Pole.

To most comprehensively appreciate the model equations, let the arbitrariness of the North Pole's longitude disambiguate the North Pole's NED frame. In other words, if the Pole is assigned a longitude of λ , then the NED frame at the Pole is to be oriented so that the unit vector "N" of NED has the same direction as for a point approaching the pole along the λ -meridian, the unit vector "D" is directed downward, and the unit vector "E" is directed so that NED is right-handed. This is equivalent to requiring the NED frame at longitude λ and latitude 90° to be the limit of NED frames as the latitude approaches 90° and the longitude and altitude remain fixed.

On 1 January 2020, directly above the North (resp. South) Pole at 6,371,200 meters from the Earth's center, the magnetic field vector lies in the half-plane of the 176.68°W (resp. 30.83°W) meridian. If the Pole is assigned $\lambda = 0^\circ$, the components X' , Y' , Z' (also the components X , Y , Z) are 1797.7 nT, 104.3 nT, and 56386.7 nT respectively at the North Pole, 14276.5 nT, -8520.4 nT and -51671.3 nT respectively at the South Pole. A change in the longitude assigned to the Pole is equivalent to a rotation of the NED frame about the polar axis.

The model equations of [section 1.2](#) support the above pole calculation and others like it provided the equation for Y' is extended by continuity as follows to ameliorate the factor $\cos(\varphi')$ in the denominator. As φ' approaches 90° , the function $(\check{P}_n^m(\sin \varphi')) / \cos \varphi'$ approaches zero if $m > 1$. It approaches certain non-zero finite limits if $m = 1$. It multiplies a zero coefficient and can be ignored if $m = 0$. For $m = 1$ and $1 \leq n \leq 12$ respectively, the limits are:

1	2	3	4	5	6	7	8	9	10	11	12
1	$\sqrt{3}$	$\sqrt{6}$	$\sqrt{10}$	$\sqrt{15}$	$\sqrt{21}$	$2\sqrt{7}$	6	$3\sqrt{5}$	$\sqrt{55}$	$\sqrt{66}$	$\sqrt{78}$

1.5 MODEL EQUATIONS NUMERICAL EXAMPLE

A software implementation of the relevant model equations is provided with this report. Most software developers should find the C programs and/or C subroutines to be sufficient for their purposes, after adaptations are made to their own software structures.

To aid software developers who need to re-implement the model equations for special requirements, Tables 3a to 3c provide a numerical example showing the intermediate calculations of [section 1.2](#). For the purpose of verifying the correct implementation of the equations, the tables display many more digits than are warranted by the accuracy of the WMM.

The output in Table 3c includes grivation calculations for four grid systems, whether or not the grid system is commonly used in that part of the world. This is helpful for the purposes of verifying correct implementation of the mathematics in the software, and if not used the unwanted grid systems may be ignored.

Table 3a: High-precision numerical example, given values for time, altitude, latitude and longitude.

Time	2022.5000 0000	yr
Height-above-Ellipsoid	100.0000 0000	km
Latitude	-80.0000 0000	deg
Longitude	240.0000 0000	deg

Table 3b: High-precision numerical example, computations of the magnetic field elements

1	lambda	4.18879 02048	rad
2	phi	-1.39626 34016	rad
3	h	1 00000.00000 00000	m
4	t	2022.50000 00000	yr
5	phi-prime	-1.39512 89589	rad
6	r	64 57402.34844 73705	m
7	g(1,0,t)	-29387.75000 00000	nT
8	g(1,1,t)	-1431.45000 00000	nT
9	g(2,0,t)	-2528.75000 00000	nT
10	g(2,1,t)	2964.25000 00000	nT
11	g(2,2,t)	1671.30000 00000	nT
12	h(1,0,t)	0.00000 00000	nT
13	h(1,1,t)	4590.15000 00000	nT
14	h(2,0,t)	0.00000 00000	nT
15	h(2,1,t)	-3067.10000 00000	nT
16	h(2,2,t)	-794.55000 00000	nT
17	Xprime	5758.51760 8019	nT
18	Yprime	14802.96638 39328	nT
19	Zprime	-49761.87672 16040	nT
20	Xprime-dot	28.13532 15304	nT/yr
21	Yprime-dot	1.39706 24624	nT/yr
22	Zprime-dot	85.59909 04809	nT/yr
23	X	5814.96588 86215	nT
24	Y	14802.96638 39328	nT
25	Z	-49755.31199 39183	nT
26	Xdot	28.03819 61827	nT/yr
27	Ydot	1.39706 24624	nT/yr
28	Zdot	85.63095 33031	nT/yr
29	F	52235.35884 49608	nT
30	H	15904.13914 83373	nT
31	D	1.19649 11054	rad
32	I	-1.26141 35720	rad
33	Fdot	-78.04814 71753	nT/yr
34	Hdot	11.55182 44235	nT/yr
35	Ddot	-0.00160 87687	rad/yr
36	I dot	0.00070 97775	rad/yr

Table 3c: High-precision numerical example, grivation calculations. Angles are in degrees.

Grid System	UPS	UPS	UTM	UTM
Grid zone	North	South	10	11
TrueN-to-GridN	240.00000 00000	-240.00000 00000	-2.95450 46801	2.95450 46801
GridN-to-MagN	-171.44610 94350	308.55389 05650	71.50839 52451	65.59938 58849
TrueN-to-MagN	68.55389 05650	68.55389 05650	68.55389 05650	68.55389 05650

1.6 MAGNETIC POLES AND GEOMAGNETIC COORDINATE SYSTEMS

There are different ways of defining magnetic poles. The most common understanding is that they are the positions on the Earth's surface where the geomagnetic field is perpendicular to the ellipsoid, that is, vertical (assuming the deflection of the vertical is negligible). These positions are called *dip poles*, and the north and south dip poles do not have to be (and are not now) antipodal. In principle the dip poles can be found by experiment, conducting a magnetic survey to determine where the field is vertical (Newitt et al., 2009). In practice the geomagnetic field is vertical on oval-shaped loci traced on a daily basis, with considerable variation from one day to the next.

Other magnetic pole definitions originate from models of the geomagnetic field (Table 4). The WMM representation of the field includes a magnetic dipole at the center of the Earth. This dipole defines an axis that intersects the Earth's surface at two antipodal points. These points are called *geomagnetic poles*. The geomagnetic poles, otherwise known as the dipole poles, can be computed from the first three Gauss coefficients of the WMM. Based on the WMM2020 coefficients for 2020.0 the geomagnetic north pole is at 72.68°W longitude and 80.59°N geocentric latitude (80.65°N geodetic latitude), and the geomagnetic south pole is at 107.32°E longitude and 80.59°S geocentric latitude (80.65°S geodetic latitude). The axis of the dipole is currently inclined at 9.41° to the Earth's rotation axis. The same dipole is the basis for the simple geomagnetic coordinate system of geomagnetic latitude and longitude (see [section 4](#), Geomagnetic longitude and latitude in Mercator projection). The geomagnetic equator is at geomagnetic latitude 0°.

The WMM can also be used to calculate dip pole positions. These *model dip poles* are computed from all the Gauss coefficients using an iterative method. In 2020.0 the north dip pole computed from WMM2020 is located at longitude 164.04°E and geodetic latitude 86.50°N and the south dip pole at longitude 135.88°E and geodetic latitude 64.07°S. Past, current and future dip pole positions are available at <https://www.ngdc.noaa.gov/geomag/GeomagneticPoles.shtml> and <https://geomag.bgs.ac.uk/education/poles.html>. Over the next five years, the WMM2020 predicts a very slow drift of the south dip pole, at about 9 km/year on average, and a faster (yet gradually decelerating) drift of the north dip pole, at about 41 km/year.

Scientists, map makers and polar explorers have an interest in the dip and geomagnetic pole locations. Although geomagnetic pole observations cannot be made to indicate their positions, these poles are arguably of greater significance than the dip poles. Auroral ovals, which are approximately 5° latitude bands where aurorae are likely to be seen, are approximately centered on the geomagnetic poles. They are usually displaced slightly to the night-side of the geomagnetic poles and greatly vary in size: bands of greatest activity occur between 15° and 25° from the geomagnetic poles.

A further concept is that of *eccentric dipole*, or off-centered dipole. The location of the center of the eccentric dipole (sometimes known as magnetic center), computed using the first eight Gauss coefficients for 2020.0 (Langel, 1987, p. 386), is at $(r, \varphi', \lambda) = (591 \text{ kilometers}, 22.67^\circ\text{N}, 136.97^\circ\text{E})$. The axis of the eccentric dipole is parallel to the axis of the (centered) dipole field.

Table 4: Computed pole positions based on the WMM2020.

	Date	North	South
Geomagnetic Poles	2020.0	72.68° W 80.59° N (geocentric) 80.37° S (geodetic)	107.32° E 80.59° S (geocentric) 80.37° S (geodetic)
Model Dip Poles	2020.0	164.04° E 86.50° N (geodetic)	135.88° E 64.07° S (geodetic)
Eccentric Dipole	2020.0	$r = 591 \text{ km}; \varphi' = 22.67^\circ\text{N}; \lambda = 136.97^\circ\text{E}$	

1.7 BLACKOUT ZONES

In an effort to provide better guidance to navigators and users, a new product has been created for WMM2020 called the “Blackout Zone” (BoZ). BoZs are generated for, both, the north and south magnetic poles. The BoZs provide improved geographic delineation to navigators as to where they can trust their compass. In the Blackout Zone, WMM declination values are not accurate and compasses are not to be trusted. In addition, BoZ Caution Zones surround the BoZs to alert navigators of increasingly unreliable compass accuracy (see Figure 2). Requirements for the BoZs are described in MIL-PRF-89500B (Department of Defense, 2019).

Previously, the United States Department of Defense (DoD) Safety of Navigation (SoN) guidance included the following warning on all polar maps and charts (Defense Mapping Agency, 1981):

“The compass becomes increasingly unreliable approaching the magnetic pole from a distance of approximately 1000 miles”.

Since the magnetic poles move significantly over time and paper products may not be updated to reflect this information, the warning was stamped on all maps and charts that covered areas within 1000 miles of the geographic poles (see Figure 2). With the prevalence of easily updatable digital maps, DoD has taken steps to provide the new BoZs for polar SoN.

Compass needles align with the horizontal magnetic field lines allowing users to see where magnetic north is from their current location. Over most of the globe, the magnetic field lines are near parallel to the Earth’s surface. However, at the magnetic poles the magnetic field lines are vertical, which is why a compass will not work well. The needle in the compass will want to point vertically and the result is a spinning needle. The BoZs are calculated to cover regions of the Earth where the horizontal component of the magnetic field is significantly weaker than the vertical component of the magnetic field.

Specifically, the BoZs are defined as constantly moving regions of the WGS 84 ellipsoid where the horizontal intensity (H) is less than 2000 nT. Each BoZ is surrounded by a Caution Zone where the horizontal intensity is less than 6000 nT. The BoZ regions are provided to users in the form of shapefiles available at <ftp://ftp.ngdc.noaa.gov/geomag/wmm/wmm2020/shapefiles/>, and are plotted on some maps for visualization purposes (see [section 1.10](#)). In addition, both NGA

products and the online calculators provided by NCEI include warnings to navigators approaching the BoZs.

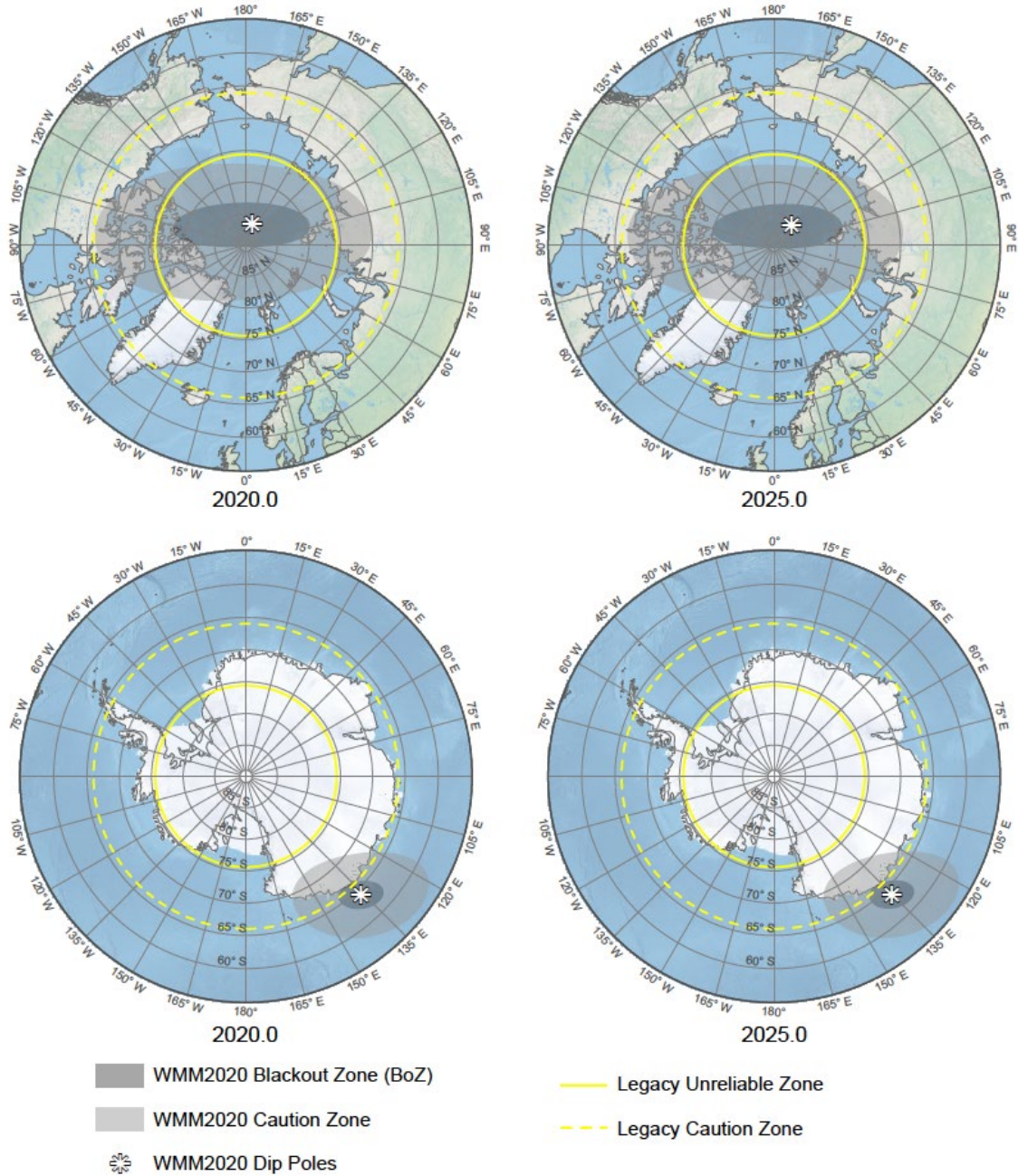


Figure 2: BoZ refinement against legacy warning zones. BoZ and Caution Zone shown at epoch 2020.0 in the Northern (top) and Southern (bottom) Hemispheres.

NCEI Warnings: “Warning: location is in the blackout zone around the magnetic pole as defined by the WMM military specification (<https://www.ngdc.noaa.gov/geomag/WMM/data/MIL-PRF-89500B.pdf>). Compass accuracy is highly degraded in this region.” [triggered if $H < 2000$ nT]

“Caution: location is approaching the blackout zone around the magnetic pole as defined by the WMM military specification (<https://www.ngdc.noaa.gov/geomag/WMM/data/MIL-PRF-89500B.pdf>). Compass accuracy may be degraded in this region.” [triggered if $H \geq 2000$ nT and $H < 6000$ nT]

NGA Warning: “This location is, either approaching or within the magnetic blackout zone defined by the World Magnetic Model (WMM) military specification, MIL-PRF-89500B. Compass accuracy is increasingly unreliable approaching the blackout zone where declination errors exceed 1 degree; and highly degraded within the blackout zone where declination errors of up to 180 degrees will occur. The large declination errors are a result of weak horizontal magnetic intensity and proximity of the magnetic pole.”

There are two important facts to note regarding the new BoZs that must be understood before implementation in navigation systems. First, the BoZs will move over time with the magnetic poles. WMM2020 provides the location of the BoZs until December 2024 and it will be the user’s responsibility to utilize the correct BoZ for the current time.

The second important fact to note is that the BoZs denote regions where compass reliability gets increasingly worse, not hard limits on where a compass cannot be used. In other words, the compass will not work perfectly 1 meter outside the BoZ and fail 1 meter within. The Caution Zone provides a buffer to assist navigators in this regard.

Figure 2 and Table 5 show the refinement of the BoZs compared against legacy paper map guidance. For the Arctic Region, the area of unreliability is reduced by over 6 million square kilometers and the area of caution is reduced by over 14 million square kilometers. The Antarctic Region reduces the area of unreliability and area of caution significantly more, and more appropriately portrays the warning zone near the magnetic pole not the geographic pole.

Table 5: BoZ size reduction against legacy warning zones. All surface areas in square kilometers on the WGS 84 ellipsoid. WMM2020 values calculated at epoch 2020.0.

	Arctic	Antarctic
Legacy Unreliable Zone	8,093,922	8,093,922
WMM2020 BoZ (Unreliable Zone)	1,546,593	279,633
Difference	6,547,329	7,814,289
Legacy Caution Zone	22,221,903	22,221,903
WMM2020 Caution Zone	7,912,969	2,311,451
Difference	14,308,934	19,910,452

1.8 SUPERSESSION OF THE MODELS

WMM2020 supersedes WMM2015 (Chulliat et al., 2015) and WMM2015v2 (Chulliat et al., 2019) and should replace them in navigation and other systems. Also included with the model is software for computing the magnetic field components X , Y , Z , H , F , I , D and auxiliary angles GV_N and GV_S as defined above, as well as the blackout zone products and the model uncertainty on each component (see [section 3](#)). WMM2020 is to be used from 1 January 2020, to 31 December 2024. In December of 2024, barring unforeseen circumstances, the U.S. and U.K. agencies will replace WMM2020 with a new degree and order 12 main field model, and a new degree and order 12 predictive secular-variation model.

1.9 POLICY ON ALTERNATE SOFTWARE FOR THE U.S. DEPARTMENT OF DEFENSE

The WMM2020 product release includes several software items by which the WMM2020 model may be computed and/or its subroutines incorporated into larger U.S. Department of Defense (DoD) systems. It is hoped that the software provided is useful for most occasions of DoD systems procurement and development.

If there are special requirements, and the model equations must be implemented anew or a separate interpolation algorithm invented, the software developer may use the label WMM2020 for the resulting product provided the resulting software agrees with the relevant model equations within the following tolerances:

Between latitudes 89.992°S and 89.992°N,

Quantities in nanotesla (nT) shall be correct to within 0.1 nT

Quantities in nanotesla (nT) per year shall be correct to within 0.1 nT/year

(see [section 1.4](#) for the computation problems exactly at the Poles).

This policy is designed to promote interoperability and to track departures from consistency when necessary. It permits systems developers to display as many digits as needed and not display unneeded digits. It also allows that the computations be taken to less than full double precision accuracy and the software retain the WMM2020 label. This policy refers to the allowed computational error in the software, not to the accuracy or limitations of the science or the geomagnetic model.

If there are special requirements, and the model equations are implemented anew or separate interpolation algorithm invented, and accuracy is sacrificed for speed of computation such that the above tolerances are not met, the label WMM2020 may not be applied to the resulting product. In this situation, the DoD entity or contractor is urged to apply to NGA or NCEI acting on behalf of NGA, for the label to adopt to indicate that this is a modification of WMM2020.

1.10 DESCRIPTION OF CHARTS

Charts of magnetic elements and their annual rates of change, and of grid variation, are available from the NOAA WMM web site (<https://www.ngdc.noaa.gov/geomag/WMM/image.shtml>). Some charts are replicated in [section 4](#). They are also available at the BGS WMM web site (<http://www.geomag.bgs.ac.uk/research/modelling/WorldMagneticModel.html>).

The following charts are available:

- Main field magnetic elements X , Y , Z , H , F , I and D on the Miller projection between geodetic latitudes 90°S and 90°N .
- Main field magnetic elements X , Y , Z , H , F , I and D on the north and south polar stereographic projection for geodetic latitudes northward of 55°N and southward of 55°S .
- Secular variation of X , Y , Z , H , F , I and D on the Miller projection between geodetic latitudes 90°S and 90°N .
- Secular variation of X , Y , Z , H , F , I and D on the north and south polar stereographic projection for geodetic latitudes northward of 55°N and southward of 55°S .
- Grid variation (GV) on the north and south polar stereographic projection for geodetic latitudes northward of 55°N and southward of 55°S .
- Geomagnetic latitude and longitude on the Miller projection between geodetic latitudes 90°S and 90°N .

Each chart comes in two versions: with blackout zone and without.

1.11 SOFTWARE, ONLINE CALCULATORS AND TEST VALUES

The WMM coefficient file, software that computes WMM values, and several derived products are distributed by NOAA/NCEI and BGS both online and offline on behalf of NGA and DGC. They are available from <https://www.ngdc.noaa.gov/geomag/WMM/soft.shtml>.

WMM online calculators allow users to compute values of the magnetic field at any point within the spatial domain of validity of the model, and at any time between the model release and 2025.0. Various input and output formats are available, as well as web-based application programming interfaces (API). The calculators are available at

- <https://www.ngdc.noaa.gov/geomag/WMM/calculators.shtml>
- https://geomag.bgs.ac.uk/data_service/models_compass/wmm_calc.html

To verify the correctness of a coefficient update or new software installation, Table 6 provides test values to validate software output.

Table 6: WMM2020 test values. The computation was carried out with double precision arithmetic. Single precision arithmetic can cause differences of up to 0.1 nT. Heights are with respect to the WGS 84 Ellipsoid. Grid Variation is with respect to the Grid North of the Universal Polar Stereographic Projection.

Date	Height (km)	Lat (deg)	Lon (deg)	X (nT)	Y (nT)	Z (nT)	H (nT)	F (nT)	I (deg)	D (deg)	GV (deg)
2020.0	0	80	0	6570.4	-146.3	54606.0	6572.0	55000.1	83.14	-1.28	-1.28
2020.0	0	0	120	39624.3	109.9	-10932.5	39624.4	41104.9	-15.42	0.16	
2020.0	0	-80	240	5940.6	15772.1	-52480.8	16853.8	55120.6	-72.20	69.36	-50.64
2020.0	100	80	0	6261.8	-185.5	52429.1	6264.5	52802.0	83.19	-1.70	-1.70
2020.0	100	0	120	37636.7	104.9	-10474.8	37636.9	39067.3	-15.55	0.16	
2020.0	100	-80	240	5744.9	14799.5	-49969.4	15875.4	52430.6	-72.37	68.78	-51.22
2022.5	0	80	0	6529.9	1.1	54713.4	6529.9	55101.7	83.19	0.01	0.01
2022.5	0	0	120	39684.7	-42.2	-10809.5	39684.7	41130.5	-15.24	-0.06	
2022.5	0	-80	240	6016.5	15776.7	-52251.6	16885.0	54912.1	-72.09	69.13	-50.87
2022.5	100	80	0	6224.0	-44.5	52527.0	6224.2	52894.5	83.24	-0.41	-0.41
2022.5	100	0	120	37694.0	-35.3	-10362.0	37694.1	39092.4	-15.37	-0.05	
2022.5	100	-80	240	5815.0	14803.0	-49755.3	15904.1	52235.4	-72.27	68.55	-51.47
Date	Height (km)	Lat (deg)	Lon (deg)	Xdot (nT/yr)	Ydot (nT/yr)	Zdot (nT/yr)	Hdot (nT/yr)	Fdot (nT/yr)	Idot (deg/yr)	Ddot (deg/yr)	
2020.0	0	80	0	-16.2	59.0	42.9	-17.5	40.5	0.02	0.51	
2020.0	0	0	120	24.2	-60.8	49.2	24.0	10.1	0.08	-0.09	
2020.0	0	-80	240	30.4	1.8	91.7	12.4	-83.5	0.04	-0.10	
2020.0	100	80	0	-15.1	56.4	39.2	-16.8	36.9	0.02	0.51	
2020.0	100	0	120	22.9	-56.1	45.1	22.8	9.8	0.07	-0.09	
2020.0	100	-80	240	28.0	1.4	85.6	11.4	-78.1	0.04	-0.09	
2022.5	0	80	0	-16.2	59.0	42.9	-16.2	40.7	0.02	0.52	
2022.5	0	0	120	24.2	-60.8	49.2	24.2	10.5	0.08	-0.09	
2022.5	0	-80	240	30.4	1.8	91.7	12.6	-83.4	0.04	-0.09	
2022.5	100	80	0	-15.1	56.4	39.2	-15.5	37.1	0.02	0.52	
2022.5	100	0	120	22.9	-56.1	45.1	23.0	10.2	0.07	-0.09	
2022.5	100	-80	240	28.0	1.4	85.6	11.6	-78.0	0.04	-0.09	

2. CONSTRUCTION OF THE MODEL

2.1 BACKGROUND ON THE GEOMAGNETIC FIELD

The Earth's magnetic field (\mathbf{B}) is a vector quantity varying in space (\mathbf{r}) and time (t). The field, as measured by a magnetic sensor on or above the Earth's surface, is actually a composite of several magnetic field contributions, generated by a variety of sources. These fields are superimposed and the sources and fields interact through inductive processes with each other. The most important of these geomagnetic sources are:

- Core field, \mathbf{B}_{core} , generated in Earth's conducting, fluid outer core;
- Crustal field, $\mathbf{B}_{\text{crust}}$, from Earth's crust/upper mantle;
- Combined disturbance field, $\mathbf{B}_{\text{disturbance}}$, from electrical currents flowing in the upper atmosphere and magnetosphere, which also induce electrical currents in the sea and the ground

The observed magnetic field is a sum of contributions:

$$\mathbf{B}(\mathbf{r}, t) = \mathbf{B}_{\text{core}}(\mathbf{r}, t) + \mathbf{B}_{\text{crust}}(\mathbf{r}) + \mathbf{B}_{\text{disturbance}}(\mathbf{r}, t) \quad (21)$$

\mathbf{B}_{core} dominates the field, accounting for over 95% of the field strength at the Earth's surface. *Secular variation* is the slow change in time of \mathbf{B}_{core} . The field arising from magnetized crustal rocks, $\mathbf{B}_{\text{crust}}$, varies spatially, but is nearly constant for the time-scales considered here. In most locations $\mathbf{B}_{\text{crust}}$ is much smaller in magnitude than \mathbf{B}_{core} but can have significant local impact on magnetic compass devices. The field arising from currents flowing in the ionosphere and magnetosphere and their resultant induced currents in the Earth's mantle and crust, $\mathbf{B}_{\text{disturbance}}$, varies both with location and time.

$\mathbf{B}_{\text{crust}}$ has spatial variations on the order of meters to thousands of kilometers and cannot be fully modeled with low degree spherical harmonic models. Therefore, the WMM does not include contributions from the crust except for those of very long wavelength. $\mathbf{B}_{\text{crust}}$ is usually smaller at sea than on land, and decreases with increasing altitude (like the core field, but much more rapidly as its sources are near the Earth's surface and its power encompasses a wide range of

spatial scales). The rock magnetization resulting in B_{crust} may be either induced by the core field or remnant from the time of formation, or be a combination of both.

Figure 3 shows the various current systems flowing in the magnetosphere. The disturbance field can vary regularly, with fundamental periods of one day and one year, as well as irregularly on time scales of seconds to days. The regular variations are both diurnal and annual, and are essentially generated by the daylit atmosphere at altitudes of 100-130 kilometers, ionized by the Sun's radiation and, moved in the Earth's magnetic field by winds and tides, thus producing the necessary conditions (motion of a conductor in a magnetic field) for a dynamo to operate. Further daily and annual variations are caused by the rotation of the Earth in the magnetospheric field, which is approximately fixed in orientation relative to the Sun. The irregular variations in the disturbance field are due to magnetic storms and sub-storms. Magnetic storms generally have three phases: an initial phase, often with a sudden commencement and increased horizontal field at mid-latitudes; a main phase; and a recovery phase. The main phase involves an intensification of the ring current (Figure 3) from the plasma sheet.

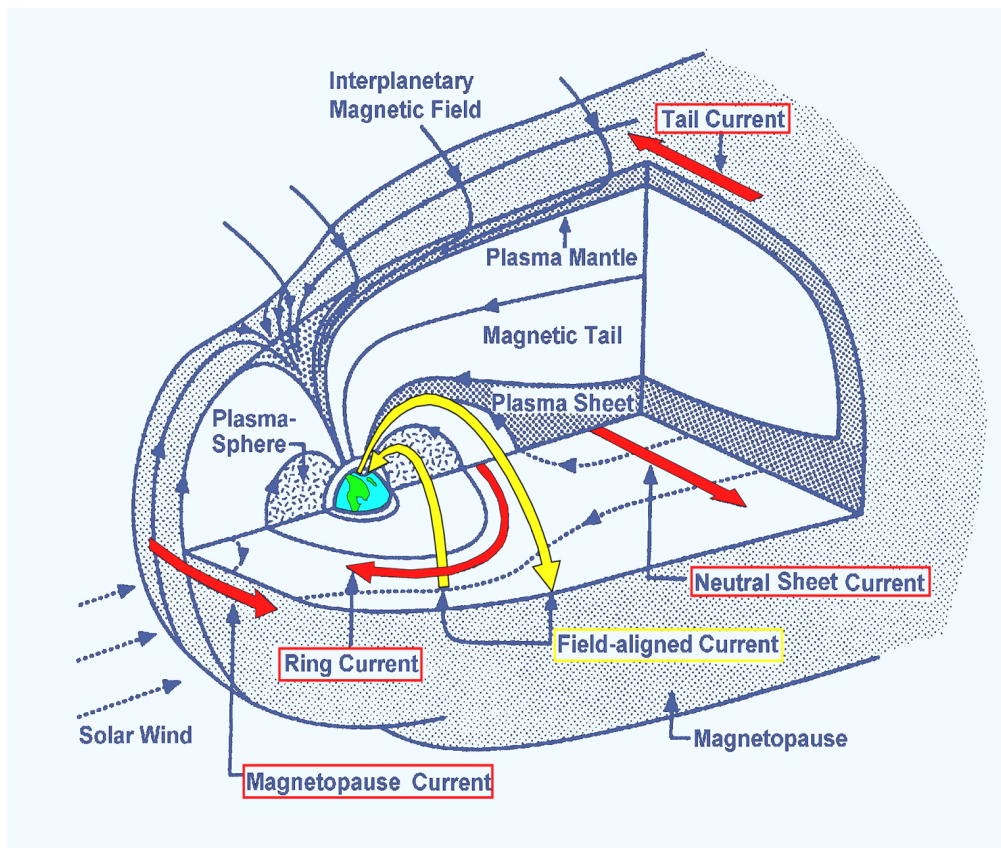


Figure 3: Current systems of the magnetosphere

During the recovery phase the ring current returns to normal over a number of days and associated sub-storms subside. Magnetic storm and sub-storm effects are generally more severe at high geomagnetic latitudes where the ionized region of the upper atmosphere (i.e., the ionosphere) is coupled to the magnetosphere by field-aligned currents. They are therefore strongly influenced by the interplanetary magnetic field and current systems in the magnetotail. Both the regular and irregular disturbance field variations are modulated by season and the solar magnetic activity cycle. The primary disturbance field is often known as the external field, as its main sources, the ionosphere and magnetosphere, are external to the surface of the Earth where geomagnetic measurements have been traditionally observed. However, this term can be confusing when using satellite data, as the ionospheric dynamo region (100-130 kilometers) is below satellite altitude and therefore effectively internal to the orbital region. For further information about the crustal and disturbance fields, and general information about geomagnetism, see Merrill et al. (1996) and Parkinson (1983).

2.2 DATA ACQUISITION AND QUALITY CONTROL

To create an accurate magnetic field model, it is necessary to have vector component measurements with good global coverage and low noise levels. The three satellites of the European Space Agency (ESA) Swarm mission, launched in November 2013, are presently the most suitable global magnetic field observing system. Ground observatory hourly mean data are also available. Although poorer in spatial coverage, the observatory data can provide valuable constraints on the time variations of the geomagnetic field.

2.2.1 SATELLITE DATA

The principal characteristic of satellite data is global coverage using consistent instrumentation collected within a relatively short time span. The inclination of the orbit (the angle between the plane containing the satellite's path and the Earth's equatorial plane) determines the latitudinal extent of the data coverage: an inclination of 90° provides 100% coverage, an inclination of slightly less or slightly more than 90° results in gaps with no data for small regions around the geographic poles. Another important characteristic of satellite data is that localized, small-scale

crustal magnetization and electromagnetic induction effects close to the Earth surface are strongly attenuated at satellite altitude, resulting in a cleaner magnetic environment for measuring the main field.

The three Swarm satellites slowly drift in local time (details below) with the Earth rotating beneath them. Thus, they provide a crude picture of the entire Earth within 24 hours. During this time each satellite completes about 15 orbits, with a longitudinal spacing of around 24 degrees. Swarm data were used in the production of the WMM2020.

2.2.1.1 SWARM

Swarm

(http://www.esa.int/Our_Activities/Observing_the_Earth/The_Living_Planet_Programme/Earth_Explorers/Swarm) is an ESA mission designed for studying all aspects of the Earth's magnetic field. Swarm is composed of three satellites, two of which fly in a constellation at a lower altitude while the third flies higher and is not synchronized with the lower pair (Friis-Christensen et al., 2006). The Swarm satellites were built by Astrium and launched on 22 November 2013 from Plesetsk in Russia on a Rockot launcher into a low Earth orbit. The planned mission duration was four years; however, funding for the lifetime of the satellite has been extended until the end of 2021.

SATELLITE AND ORBIT

Swarm is composed of three satellites (A, B, C) which all fly in near-polar orbits. The lower pair (A and C) have inclinations of 87.4° and altitudes of about 450 km in late 2019, while the higher satellite (B) has an inclination of about 88° and an altitude of about 500 km. The satellites complete an orbit in approximately 90 minutes at a speed of about 8 km/s. Each satellite weighed 468 kg at launch and is just over 9 m in length with the boom deployed.

MAGNETOMETERS

Each Swarm satellite carries a Vector Field Magnetometer (VFM) mid-boom (Figure 4), built by the Danish Technical University. The VFMs are tri-axis fluxgate magnetometers sampling the field at 50 Hz. Once calibrated, they have an accuracy better than 1 nT. Additionally, there is an

Absolute Scalar Magnetometer (ASM) at the tip of the boom used to perform an absolute calibration of the vector instruments. Each ASM has a redundant sensor. These were built by the French Atomic Energy Commission - Laboratoire d'Electronique de Technologie et d'Instrumentation (CEA-Leti), under a contract with the French National Center for Space Studies (CNES). The scalar magnetometers are optically-pumped metastable helium-4 magnetometers, sampling the field at 1 Hz in nominal mode, and at 250 Hz in a so-called “burst” mode. They have a resolution of 0.1 nT and an absolute accuracy better than 0.3 nT.

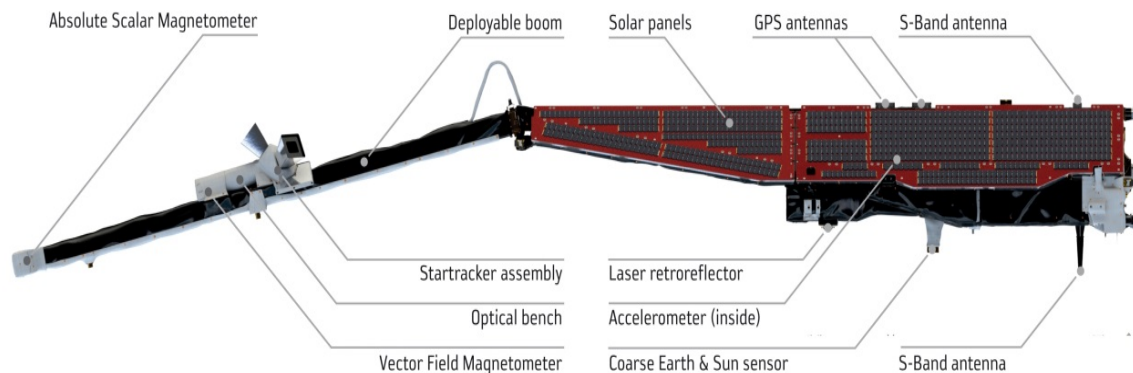


Figure 4: Swam instruments. On each satellite, the scalar magnetometer is located at the top of the boom. The vector fluxgate magnetometer is located mid-boom, about 1.6 m from them, and is co-mounted with the star imagers.

STAR IMAGERS

A star imager, developed and supplied by the Danish Technical University, provides satellite attitude control. An ultra-stable optical bench connects the star imager and the vector magnetometer. Attitude uncertainty is the largest source of error in satellite vector magnetic data. Star imagers are often blinded by the sun or moon and provide unreliable attitude with regard to rotations about their direction of vision (bore sight). For this reason, Swarm is equipped with a triple-head star imager, while earlier magnetic satellites were equipped with single-head (Ørsted) or dual-head (CHAMP) star imagers.

GLOBAL POSITIONING SYSTEM (GPS) RECEIVERS

Each Swarm satellite is equipped with a dual frequency GPS receiver providing precise positioning and time-tagging of the data acquired by the instruments. Precise positioning is also used for spacecraft control. The GPS receivers were provided by ESA.

DATA PRODUCTS

Swarm's standard data products are labeled from level-0 to level-2, according to the amount of processing applied to the original data. Level-0 products are raw measurements from the onboard instruments. Level-1 products are processed raw measurements that are in physical units, as well as having transformations applied so that they are in useful coordinate systems (e.g., geographic). Level-2 refers to scientific products (e.g., field models) which make direct use of the Level-1 data. The data used for the WMM comes from the most recent Level-1(b) Swarm dataset (version 0505 and later), which is freely provided by ESA at <https://earth.esa.int/web/guest/swarm/data-access>.

2.2.1.2 IN-ORBIT CALIBRATION OF SATELLITE MAGNETOMETERS

Experience with several satellite missions shows that calibration parameters can change significantly during deployment into space. Furthermore, calibration parameters exhibit gradual changes over the life of the mission. Regular in-flight calibration and updates of the respective parameters is therefore essential. To enable a successful calibration in orbit, it is of critical importance that the instruments be built in such a way that they can be described by a linear model with constant (over one day) calibration parameters. While these parameters may change slowly over the mission lifetime, they must be independent of strength or direction of the ambient magnetic field. In particular, past satellite magnetic missions have shown that it is not possible to perform an in-orbit scalar calibration of a vector magnetometer when the component readings suffer from a “transverse field effect” (Brauer et al., 1997).

The linear instrument model used for Swarm is similar to the one previously used to successfully calibrate the Danish Ørsted satellite (Olsen et al., 2003). It can be formulated as a linear transform from the desired quantity \mathbf{B} , the magnetic field vector in the reference frame of the star tracker, to the instrument output vector \mathbf{E} as

$$\mathbf{E} = \mathbf{S} \mathbf{P} \mathbf{R} \mathbf{B} + \mathbf{b} \quad (22)$$

where \mathbf{S} is a diagonal matrix of scale factors, \mathbf{P} corrects for non-orthogonalities of the sensor elements, \mathbf{R} rotates from the star tracker reference frame into the vector magnetometer frame, and \mathbf{b} is the offset vector. Each of these corrections generally has three parameters which have to be determined in the calibration. (The Swarm calibration incorporates the characterization of a Sun-driven disturbance field which includes more parameters, see Tøffner-Clausen et al., 2016).

The scalar in-orbit calibration is based on a comparison between the readings of the scalar and vector magnetometer. In a least-squares estimation procedure, the nine calibration parameters of a fluxgate can be determined. Here, the synthetic laboratory test field is replaced by the natural ambient field recorded over a day. This allows for regular verification of the offset vector \mathbf{b} , non-orthogonalities \mathbf{P} , and scale factors \mathbf{S} .

The calibration parameters of the matrix \mathbf{R} , namely the three rotation angles between the magnetometer and star tracker reference systems, are determined in a final, independent step. To determine these angles, one makes use of the fact that $\text{div}(\mathbf{B})$ is zero, and chooses measurements outside of the auroral current regions, where $\text{curl}(\mathbf{B})$ is also zero. Under these circumstances, the effect of misalignments of the star tracker and vector magnetometer reference system can be separated cleanly from genuine magnetic fields, and the three calibration parameters of the matrix \mathbf{R} can be determined by a least-squares inversion. This calibration can only succeed if the vector magnetometer and the star tracker are co-mounted onto an optical bench with sufficient rigidity and temperature stability.

2.2.2 OBSERVATORY DATA

One of the principal characteristics of observatory data is the long-term continuous coverage over time. The spatial distribution of observatories is largely determined by the location of habitable land and by the availability of local expertise, funds and energy supply. While the distribution is uneven and sparse compared to that of satellite data, it has been reasonably constant in time (Figure 5).

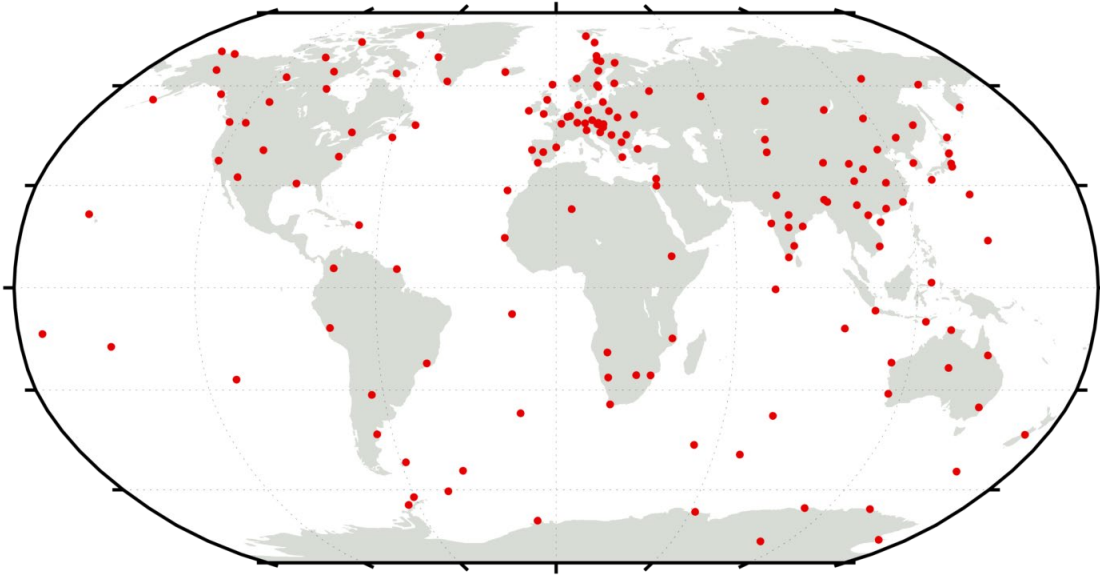


Figure 5: Locations of observatories whose data contributed to BGS parent model.

INSTRUMENTATION

There are three categories of instruments at an observatory. The first category comprises variometers, which make continuous measurements of elements of the geomagnetic field vector. Both analog and digital variometers require temperature-controlled environments, extremely stable platforms, and can generally operate without manual intervention. Today, the most common type of variometer is the tri-axial fluxgate magnetometer.

The second category comprises absolute instruments that can make measurements of the magnetic field in terms of absolute physical basic units or universal physical constants. The most common types of absolute instrument are the fluxgate theodolite, for measuring D and I , and the proton precession magnetometer for measuring F . In the former instrument the basic unit of measurement is an angle. To determine these angles, the fluxgate sensor mounted on the telescope of a non-magnetic theodolite is used to detect when it is perpendicular to the magnetic field vector. With the fluxgate sensor operating in this null-field mode, the stability of the sensor and its electronics is maximized. To complete the determination of D and I , true north is found by reference to a fixed mark of known azimuth, usually by astronomical observations. In a proton precession absolute magnetometer, the universal physical constant is the gyromagnetic ratio of the proton. Measurements with a fluxgate theodolite can only be made manually while a proton magnetometer can operate automatically.

The third category comprises semi-absolute instruments. These instruments measure deviations from a field, which is determined on a regular basis using an absolute instrument. One example is a proton vector magnetometer where artificial orthogonal bias fields are applied to a proton precession magnetometer sensor, located at the center of a set of coils through which currents can be passed, to obtain the components of the field vector. Like variometers, these instruments are temperature-sensitive and require stable platforms. For more information on magnetic instrumentation and operation of magnetic observatories, see Macmillan (2007), Jankowski and Sucksdorff (1996) and Chulliat et al. (2017).

DATA COLLECTION AND QUALITY CONTROL

BGS and NOAA actively collect observatory data through their involvement in the World Data Center (WDC) system. They maintain databases suitable for magnetic field modeling, maintain contacts with organizations operating magnetic observatories, and collaborate with other WDCs. Each year BGS sends requests to all organizations with operating observatories for the latest data and other relevant information. The WDCs for geomagnetism benefit greatly from the efforts of INTERMAGNET, an organization whose objectives are to establish a global network of cooperating digital magnetic observatories, to adopt modern standard specifications for measuring and recording equipment, and to facilitate data exchange and the production of geomagnetic products in close to real time. In addition to operating nine of the observatories shown in Figure 5, BGS runs one of five INTERMAGNET GINs (Geomagnetic Information Node), and plays a leading role in the organization (<https://intermagnet.github.io/>).

The hourly means used in the WMM were selected from definitive data held at <https://wdc.bgs.ac.uk/> and from recent quasi-definitive data (Peltier and Chulliat, 2010; Clarke et al., 2013) produced primarily by INTERMAGNET observatories. The quality of the data an observatory produces is the responsibility of the operator. The most important aspect of the quality for global modeling is the stability of the baseline, the difference between the calibrated variometer data and the absolute observations. A baseline with many points, low scatter, few drifts and offsets is an indicator of good quality. Baseline plots for the INTERMAGNET observatories are available along with their definitive data.

Quality assurance and control measures, other than those carried out by the observatory operators, are also accomplished by INTERMAGNET through its observatory standardization program, the WDCs, and by participation in the International Association of Geomagnetism and Aeronomy (IAGA) Observatory Workshops.

Final quality control procedures prior to deriving the WMM are completed by BGS. For the hourly means this involves plotting all data to identify typographical errors and large offsets, and then plotting residuals to hourly models to identify remaining measurement artefacts such as noise, small offsets and trends. Hourly spherical harmonic models of degree 9 and order 1 are fit to residuals after estimates of the core, crustal and ionospheric fields are removed from the observatory hourly means, the details of which are in Macmillan and Olsen (2013). (Although these models are not realistic magnetospheric field models, they help reduce signals that are coherent in time and space.) Observatories used in the production of WMM2020 are listed in Table 7.

Table 7: Observatories used in production of BGS parent model. An asterisk (*) with the IAGA code indicates observatories for which the record contains an unquantified jump, about which data series are split and treated as independent series. Number of data indicates number of vector triples or scalar values used from each location.

IAGA code	Latitude	Longitude	Altitude (km)	Number of data
AAA	43.250	76.917	1.300	528
AAE*	9.033	38.767	2.441	245
ABG*	18.633	72.867	0.007	1378
ABK	68.350	18.817	0.380	1457
AIA	-65.250	295.750	0.010	889
AMS	-37.800	77.567	0.048	250
API*	-13.800	188.217	0.002	1091
ARS	56.433	58.567	0.290	773
ASC	-7.950	345.617	0.177	1498
ASP	-23.767	133.883	0.557	1610
BDV	49.083	14.017	0.496	1274
BEL	51.833	20.800	0.180	1273
BFO	48.333	8.317	0.641	883
BGY	31.717	35.083	0.750	450
BJN	74.500	19.200	0.020	1467
BLC	64.333	263.967	0.030	1075
BMT*	40.300	116.200	0.183	1124
BOU	40.133	254.767	1.650	1669
BOX	58.067	38.217	0.115	1197
BRW	71.300	203.383	0.012	1638
BSL*	30.350	270.367	0.008	1167

CBB	69.117	254.967	0.020	655
CBI	27.100	142.183	0.155	696
CDP*	31.000	103.700	0.653	1127
CKI	-12.183	96.833	0.003	1525
CLF	48.017	2.267	0.145	1401
CMO*	64.867	212.133	0.197	1658
CNB	-35.317	149.367	0.859	1580
CNH*	43.833	125.300	0.234	1132
COI	40.217	351.583	0.099	636
CSY*	-66.283	110.533	0.040	1560
CTA	-20.083	146.267	0.370	1441
CTS	46.050	11.650	1.175	987
CYG	36.367	126.850	0.165	1269
CZT	-46.433	51.867	0.155	675
DED	70.367	211.200	0.010	950
DLT	11.917	108.417	1.583	1205
DOB*	62.067	9.117	0.660	1455
DOU	50.100	4.600	0.225	1363
DRV	-66.667	140.017	0.030	439
EBR	40.957	0.333	0.053	1430
ELT	29.667	34.950	0.250	659
ESA	39.233	141.350	0.396	912
ESK	55.317	356.800	0.245	1489
EYR	-43.400	172.400	0.120	868
FCC	58.783	265.917	0.015	1155
FRD	38.217	282.633	0.069	1672
FRN	37.083	240.283	0.331	1549
FUQ	5.467	286.267	2.543	258
FUR	48.167	11.283	0.572	1275
GAN	-0.700	73.150	0.002	868
GCK	44.633	20.767	0.231	780
GDH	69.250	306.467	0.024	1237
GLM	36.400	94.900	2.802	1094
GNG	-31.350	115.717	0.050	1563
GUA	13.583	144.867	0.150	1616
GUI*	28.317	343.567	0.868	970
GZH	22.967	112.450	0.014	1131
HAD	51.000	355.517	0.095	1484
HBK	-25.883	27.700	1.522	1329
HER	-34.417	19.233	0.026	1417
HLP	54.600	18.817	0.001	1391
HON	21.317	202.000	0.004	1631
HRB*	47.867	18.183	0.120	1274
HRN	77.000	15.550	0.015	1284
HUA	-12.050	284.667	3.312	1202
HYB	17.417	78.550	0.500	920
IPM	-27.167	250.583	0.083	998
IQA*	63.750	291.483	0.067	1087
IRT	52.167	104.450	0.460	1393
IZN	40.500	29.733	0.256	1222
JAI	26.867	75.817	0.437	899
JCO	70.350	211.200	0.020	1688

KAK	36.233	140.183	0.036	1600
KDU	-12.683	132.467	0.014	1598
KEP	-54.283	323.500	0.007	1566
KHB	47.617	134.683	0.092	1521
KIR	67.850	20.417	0.395	982
KIV	50.717	30.300	0.140	1078
KMH*	-26.533	18.117	1.065	935
KNY	31.417	130.883	0.107	1543
KNZ	35.250	139.950	0.342	1136
KOU	5.217	307.283	0.010	1525
KPG	-10.200	123.667	0.240	618
KSH*	39.500	76.000	1.321	1117
LER	60.133	358.817	0.085	1490
LIV	-62.667	299.600	0.019	878
LMM	-25.917	32.583	0.047	329
LON	45.400	16.667	0.095	1284
LRM	-22.217	114.100	0.004	1589
LRV	64.183	338.300	0.005	1491
LVV*	49.900	23.750	0.326	1006
LYC	64.617	18.750	0.270	1456
LZH*	36.083	103.850	1.560	1363
MAB	50.300	5.683	0.440	1377
MAW	-67.600	62.883	0.012	1427
MBO	14.400	343.050	0.007	1156
MCQ	-54.500	158.950	0.008	1548
MEA	54.617	246.650	0.700	1478
MGD	60.117	151.017	0.226	1525
MIZ	39.117	141.200	0.125	1066
MMB	43.917	144.183	0.042	1612
MZL	49.600	117.400	0.682	1138
NAQ	61.167	314.567	0.004	1415
NCK	47.633	16.717	0.153	1028
NEW	48.267	242.883	0.770	1696
NGK	52.067	12.683	0.078	1460
NGP*	21.133	79.033	0.334	476
NMP	-15.100	39.250	0.374	828
NUR	60.500	24.650	0.105	863
NVS	54.850	83.233	0.130	1576
ORC	-60.733	315.217	0.003	101
OTT	45.400	284.450	0.075	1472
PAF*	-49.350	70.267	0.035	439
PAG	42.517	24.183	0.556	867
PEG	38.083	23.933	0.380	258
PET	52.967	158.250	0.050	1669
PHU*	21.033	105.967	0.005	620
PIL	-31.667	296.117	0.336	489
PLR	-6.967	106.550	0.054	294
PND	12.017	79.850	0.036	482
PPT	-17.567	210.433	0.357	725
PST	-51.700	302.100	0.135	1524
QGZ*	19.000	109.800	0.227	912
QIX*	34.550	108.200	0.730	700

QZH	24.900	118.600	0.010	1090
RES	74.683	265.100	0.030	1435
SBA	-77.850	166.783	0.010	1422
SBL	43.933	299.983	0.005	1543
SFS	36.467	353.800	0.000	1438
SHL	25.567	91.867	0.000	466
SHU	55.350	199.533	0.080	1620
SIL*	24.933	92.817	0.000	468
SIT	57.067	224.667	0.024	1651
SJG	18.117	293.850	0.424	1088
SOD	67.367	26.633	0.178	865
SPT	39.550	355.650	0.922	1381
STJ	47.600	307.317	0.100	1267
SUA*	44.683	26.250	0.084	1290
TAM	22.800	5.533	1.373	1457
TDC	-37.067	347.683	0.042	795
THJ	24.000	102.700	1.820	1130
THL	77.483	290.833	0.057	1473
THY	46.900	17.900	0.187	1028
TIR*	8.667	77.817	0.034	478
TND	1.283	124.950	0.704	533
TRO	69.667	18.950	0.105	1474
TRW	-43.267	294.617	0.015	213
TSU	-19.200	17.583	1.100	769
TUC*	32.167	249.267	0.946	1619
UPS	59.900	17.350	0.050	1457
VAL	51.933	349.750	0.014	1057
VIC	48.517	236.583	0.197	1466
VNA	-70.650	351.750	0.040	1147
VOS*	-78.450	106.867	3.500	645
VSK*	17.733	83.333	0.020	418
VSS	-22.400	316.350	0.457	478
WHN	30.533	114.567	0.042	1140
WIC	47.933	15.867	1.088	877
WIK	48.267	16.317	0.400	631
WNG	53.750	9.067	0.050	1234
YAK*	61.967	129.667	0.100	1127
YKC	62.483	245.517	0.198	611

2.2.3 OTHER DATA AND DERIVED PRODUCTS

Other magnetic data and products used in the production of the WMM are various magnetic activity indices derived from observatory data, and solar wind data measured by the ACE satellite

(<http://www.srl.caltech.edu/ACE>). These are used to either select the data for input to the model or to form part of the input to the model.

INDEX K_P

The planetary K_p ("Planetarische Kennziffer") index (<https://www.gfz-potsdam.de/en/kp-index/>) is based on the K-index, a local index of the three-hourly range in magnetic activity of the two horizontal field components (X and Y) relative to an assumed quiet-day curve for the geomagnetic observatory. Local disturbance levels are determined by measuring the range (difference between the highest and lowest values) during three-hour time intervals for the most disturbed magnetic field component. The range is then converted into a local K-index according to a pseudo-logarithmic scale, which is station specific, in an attempt to normalize the frequency of the different disturbance sizes. The three-hourly K_p index is the average of local K values from 13 selected subauroral stations and is expressed in a scale of thirds (28 values). The IAGA station codes (in order of geomagnetic latitude) are: LER, MEA, SIT, ESK, UPS, OTT, BFE, HAD, WNG, NGK, FRD, CNB and EYR. Prior to the averaging, the K values are standardized according to station and season. Also CNB and EYR are averaged first, as are UPS and BFE and then used as single points in the overall average of eleven. The K_p index is used to select measurements during magnetically undisturbed times.

INDICES DST AND RC

Charged particles trapped by the geomagnetic field in the magnetosphere drift around the Earth at a distance of 3-8 Earth radii creating a westward electric ring current whose field opposes the main geomagnetic field. The strength of this field is on the order of tens of nT during quiet times and several hundred nT during magnetic storms. Magnetopause, tail and partial ring currents represent additional contributions leading to asymmetries in the field which increase during storms. The symmetric part of this composite disturbance field is tracked by the Dst (disturbance storm-time) index (Sugiura, 1964; <http://wdc.kugi.kyoto-u.ac.jp/dstdir>) and the RC (ring current) index (Olsen et al., 2014; <http://www.spacecenter.dk/files/magnetic-models/RC/current>). The Dst index is derived from measurements collected at four low-latitude observatories. The RC index is derived from measurements at 21 mid- and low-latitude observatories and is generally thought to more accurately track the quiet-time ring current field at ground and low Earth orbit altitude. The Dst and RC indices and their time derivatives are used for data selection.

INTERPLANETARY MAGNETIC FIELD

The solar wind drives electric currents in the Earth's magnetosphere and ionosphere. An interplanetary magnetic field (IMF) is carried by the plasma of the solar wind. Relevant for the response of the magnetosphere is the speed of the solar wind and the direction and strength of the IMF. These solar wind parameters are monitored by NASA's Advanced Composition Explorer (ACE) satellite (<http://www.srl.caltech.edu/ACE>) and NOAA's Deep Space Climate Observatory (DSCOVR) satellite (<https://www.nesdis.noaa.gov/content/dscovr-deep-space-climate-observatory>). Using magnetospheric models, the ACE solar wind measurements are projected downstream onto the magnetospheric bow shock (the boundary between the solar wind and the magnetosphere) and are made available by NASA as 1-minute readings in geocentric magnetospheric coordinates at <https://omniweb.gsfc.nasa.gov/hw.html>. The IMF is used both for data selection and as a quantitative parameter to correct for magnetospheric disturbance fields.

MERGING ELECTRIC FIELD E_M

The merging electric field, derived from the IMF and solar wind speed (<https://omniweb.gsfc.nasa.gov/hw.html>), is a parameter suitable for describing the variation of the magnetospheric tail current field. Following Kan and Lee (1979), the merging electric field, E_m , is calculated as

$$E_m = v_{SW} (B_y^2 + B_z^2)^{1/2} \sin^2 \frac{\Theta}{2} \quad (23)$$

where v_{SW} is the solar wind velocity, B_y and B_z are the IMF components in the Geocentric Solar Magnetospheric (GSM) frame and Θ is the clock angle of the IMF (i.e., the angle made by the B_y and B_z components of the IMF in the vertical plane to the ecliptic, counted from 0 when IMF B_z is north). Here we use a revised definition of the merging electric field, following Newell et al. (2007) and Olsen et al. (2014):

$$E_m = 0.33 v_{sw}^{4/3} (B_y^2 + B_z^2)^{2/3} \sin^{8/3} \frac{\theta}{2} \quad (24)$$

The merging electric field is used for data selection.

2.3 DERIVATION OF THE MODEL

Since the WMM only describes the long-wavelength internal part of the geomagnetic field, it is important to separate unrelated contributions to the field, which would otherwise contaminate the WMM coefficients. A successful modeling strategy relies on four elements:

1. DATA SELECTION

Measurements during daytime and during periods of strong solar activity are contaminated by external current systems, which are difficult to accurately model. Therefore, only nighttime data measured during magnetically quiet periods, as inferred from the above-described indices, were used in estimating the WMM coefficients.

2. DATA CORRECTIONS

Some contributions to the measured magnetic field, such as the crustal magnetic field, can be accurately modeled and corrected for prior to the estimation of the WMM main field coefficients.

3. DATA WEIGHTING

The disturbance field includes features that, even after careful data selection, cannot be modelled. Also, polar orbiting satellites collect more data per unit area at high-latitudes than at low-latitudes. Data including these features are downweighted in the estimation of the WMM coefficients.

4. USE OF EXTENDED PARENT MODELS

To account for contributions that have not been removed in the previous three steps, an extended set of model parameters is co-estimated with the WMM model coefficients. These account for smaller-wavelength internal magnetic field contributions (spherical harmonic degree larger than 12), higher time derivatives (e.g., secular acceleration) and contributions from currents external to the Earth. The set of WMM coefficients plus the extended model parameters is called a *parent model* of the WMM. Two separate parent models were produced, reflecting different modeling strategies employed by NCEI and BGS.

2.3.1 NCEI EXTENDED PARENT MODEL

The NCEI main field and secular variation coefficients for WMM2020 were derived from an extended parent model. The parent model was built entirely from Swarm satellite data, and included a parameterization of the time-dependent part of the internal field to spherical harmonic degree and order 15, a parameterization of the static (time-independent) part of the internal field to spherical harmonic degree and order 50, and a set of a time-varying alignment parameters describing the rotation between the fluxgate magnetometer instrument frame and the star camera frame on Swarm. Swarm's attitude is provided by a set of three star camera instruments which together define a common reference frame (CRF). The fluxgate axes, however, are not aligned with the CRF axes, and so an additional rotation must be specified between these two frames. Additionally, thermal effects can cause these two frames to vary with respect to each other over time, and so we allow these rotation alignment parameters to slowly vary in time. In the following sections, we further describe the data selection and preprocessing, data weighting, and model parameters used in the NCEI parent model.

DATA SELECTION

When modeling Earth's core field, it is important to minimize contributions from external fields originating in the ionosphere and magnetosphere. This is accomplished by using data only during certain local time periods when ionospheric contributions are minimal. We also use indices designed to track disturbed periods of geomagnetic activity. These indices are derived from a combination of satellite and ground observations. We additionally attempt to detect and remove erroneous Swarm measurements from our dataset, which could occur for example during satellite

maneuvers, star camera blinding, or other instrument errors. This is accomplished by comparing measurements from every Swarm orbit against an *a priori* core field model. Orbital tracks which show large deviations from the model prediction are discarded. The data selection criteria employed for the NCEI parent model are shown in Table 8.

After the data selection is performed according to Table 8, we additionally downsample the Swarm data to one sample every 30 seconds. Swarm nominally samples the geomagnetic field at 1 Hz, which is a far higher resolution than is needed for the WMM.

Table 8: Data selection criteria for Swarm satellite data used when producing the NCEI parent model.

Parameter	Description	Minimum Value	Maximum Value
LT < 55° QD latitude	Local time of ascending/descending node equatorward of 55° quasi-dipole latitude	00:00	05:00
Kp, Kp _{-3h}	3-hour planetary K index at datum and in preceding 3-hour interval	0	2
dRC/dt , dRC/dt _{-1h}	Temporal change in RC (ring current) index at datum and in preceding 1-hour interval	0 nT/hr	3 nT/hr
Zenith angle > 55° QD latitude	Solar zenith angle is a better indicator of darkness/sunlight at high-latitudes (poleward of 55° quasi-dipole latitude)	110°	-

DATA WEIGHTING

The NCEI parent model assigned weights to each individual datum. Since polar orbiting satellites sample the polar regions more densely than the low-latitudes, we applied the weighting scheme of Alken et al. (2014), which is designed to upweight more sparsely sampled equatorial regions, and downweight the densely sampled polar regions, in order to achieve a uniform weighting at all latitudes. Despite careful data selection and preprocessing, inevitably a small number of erroneous measurements are included in the model, and so we perform several iterations of model fitting, assigning additional weights at each iteration to detect and downweight these

erroneous outliers. This is done following the procedure of Huber (1996), the so-called robust Huber weighting.

MODEL DESCRIPTION

The NCEI parent model uses Swarm A and B data between November 3, 2016 and November 2, 2019 to determine the WMM2020. The model co-estimates several sets of parameters, as described below:

1. Time-dependent internal field: each Gauss coefficient to spherical harmonic degree and order 15 is parameterized as a quadratic polynomial, accounting for the main field, secular variation, and secular acceleration over the three year time interval. This yields a total of 765 time-dependent internal field parameters.
2. Time-independent internal field: each Gauss coefficient between spherical harmonic degrees 16 and 50 is parameterized as a single static parameter. These parameters account primarily for the higher resolution lithospheric field. There are a total of 2,345 such parameters in the model.
3. Time-dependent alignment parameters: the model estimates a set of alignment parameters between the fluxgate magnetometer instrument frame and the star camera common reference frame. These are parameterized as quadratic splines with knot intervals of 30 days over the 3 year time period. There are a total of 228 alignment parameters in the model.
4. The total number of model parameters estimated is 3,338.

The NCEI parent model does not co-estimate a large-scale magnetospheric field. Instead, it removes the CHAOS external field model from the Swarm measurements, which is parameterized by the RC index (Olsen et al., 2014; Finlay et al., 2016). The model was estimated using robust iteratively re-weighted least squares with a Levenberg-Marquardt approach. The model was also regularized by minimizing the secular variation in the radial field component, averaged over the core mantle boundary. The regularization parameter was chosen to achieve a converging secular variation power spectrum to spherical harmonic degree 15.

2.3.2 BGS EXTENDED PARENT MODEL

The BGS estimates of the main field and secular variation coefficients for WMM2020 were derived from an extended parent model. This parent model includes smaller wavelength spatial features, higher time derivatives of variations, and additional modelled contributions to Earth's observed field. From this parent model, the large-scale internal field and its secular variation could be more accurately extracted. The procedure for selecting, correcting and weighting data to produce the parent model, parameterizing the model, and extracting the desired coefficients, is described in the following sections.

DATA SELECTION

Two data sources were used to construct the parent model: (1) the ESA Swarm mission, and (2) the ground observatory network.

Data were collected from available ground observatory locations for the period from 1st January 2013 to 15th October 2019. The distribution of locations is shown Figure 5, and observatory details are summarized in Table 7. Vector observations were used at low- and mid-geomagnetic dipole latitudes (GMDL), while for high GMDL, a unit vector given by a prior BGS model of the internal geomagnetic field was used to project the vector observations to a pseudo-scalar field value in the prior unit vector direction. The projection of scalar data onto a prior model direction creates a linear relation between these data and the model coefficients for which we wish to solve. All data were transformed from the reported geodetic coordinate system to a geocentric coordinate system, and subject to selection for geomagnetically quiet, local night times, as summarised in Table 9. Observatory records that contained any unquantified jumps were split about these times and treated as independent data series. Such records are indicated with asterisks in Table 7.

Swarm data from the Alpha, Bravo and Charlie satellites were collected for the period from mission start on 25th November 2013 to 15th October 2019. The latest available data baselines were used, up to version 0507. Vector observations were used at all latitudes, with scalar observations only used when vector data were not available. All data were subjected to a rigorous selection procedure for geomagnetically quiet periods. Low- and mid-GMDL data were used only

during local night times to avoid the influence of solar-driven fields in the ionosphere, while high GMDL data were used at all local times to avoid seasonal gaps in the data. The data selection procedure is summarized in Table 9.

Table 9: Data selection criteria for Swarm satellite and ground observatory data used when producing the BGS parent model.

Filter	Description	Satellite	Observatory
Sampling		Every 20 th 1Hz datum	Hourly mean
Kp, Kp _{-3h}	3-hour planetary K index at datum and in preceding 3-hour interval	$\leq 2_0, \leq 2_0$	$\leq 2_+$
$ D_{st} $ [nT], $ dD_{st}/dt $ [nT·h ⁻¹]	Storm time disturbance and its rate of change per hour at datum	$\leq 30, \leq 2$	$-, \leq 5$
IMF $ B_x , B_y B_z$ [nT]	Projected Interplanetary Magnetic Field at datum	$\leq 10, \leq 3, 0 \leq x \leq 6$	$-, -, \geq -2$
v_{sw} [km·s ⁻¹]	Projected solar wind velocity at datum	≤ 450	–
LT (< 55°GMD)	Local time at GMD latitudes below 55°	$23:00 \leq x \leq 05:00$	$01:00 \leq x \leq 02:00$
$ d-d_{prior} $ [nT]	Absolute difference between datum and a prior BGS field model estimation	≤ 100	–
$ F- B $ [nT]	Absolute difference between ASM and magnitude of VFM data	≤ 2	–
E_{min} (> 55°GMD) [mV·m ⁻¹]	Hourly mean of 1-minute merging electric field (calculated after Olsen et al., 2014) at GMD latitudes above 55°	≤ 0.8	–

DATA CORRECTION AND WEIGHTING

A prior BGS crustal field model was removed from all satellite and observatory data. Doing so allows the parent modelling process to perform a less complex calculation, solving only for the larger-scale and time varying parts of the observed field.

Data weights (variances) were assigned to each datum to account for local and global, small- and large-scale sources of uncertainty, following the scheme of Thomson et al. (2010). For satellite data, these weights were:

- Along-track standard deviation over each 20-second orbit segment
- Disturbance field activity as measured at the geographically nearest ground observatories (LAVA index, Thomson et al., 2010)
- Spatially uniform noise, scaled by a function of solar zenith angle
- Data density per unit area relative to the mean data density

For observatory data, these weights were:

- Spatially uniform noise, scaled by a function of solar zenith angle, with a higher base value assigned to pseudo-scalar data at high GMDL, than for vector data at mid- to low-GMDL
- Data density per unit area relative to the mean data density

A final scaling was applied to these weights such that the sum of the total weights of observatory data was approximately 10% of the sum of the total weights assigned to satellite data.

MODEL DESCRIPTION

The BGS parent model co-estimates several field sources, and is parameterized as follows.

- Core field:
 - Spherical harmonic (SH) degree and order 15
 - Order 6 B-spline time dependence, with 6 month spaced knots from 2012.75 to 2020.75
 - Regularized time integral of the 3rd time derivative of the radial magnetic field over the core-mantle boundary (CMB)
 - Regularised 2nd time derivative of the radial magnetic field over the CMB, at the spline end knots
- Large-scale crustal field correction:
 - Static in time, described from SH degrees 16 to 30
 - Variation relative to the prior crustal field model used to correct data
- Large-scale slowly varying external field:
 - SH degree and order 1

- order 2 B-spline time dependence, with 3 month spaced knots from 2012.75 to 2020.25
- Large-scale rapidly varying external and induced field:
 - SH degree and order 1
 - Order 2 B-spline time dependence governed by the VMD index (Thomson and Lesur, 2007) with 3 month spaced knots from 2012.75 to 2020.25
- Periodic variations:
 - Sine and cosine terms accounting for external and induced, annual and semi-annual variations
 - External sine and cosine terms accounting for diurnal variations, parameterised by sun-synchronous longitude
- Local crustal biases:
 - static offsets at each observatory location to account for small-scale crustal field

The model was fit by robust iteratively-reweighted least-squares, and converged within three iterations. Damping was chosen to balance the fit to the data against the level of temporal smoothing applied to the core field by the regularisation.

DERIVATION OF BGS MAIN FIELD AND SECULAR VARIATION COEFFICIENTS FOR WMM2020

The BGS secular variation coefficients for 2020 to 2025 were taken to be the mean of the instantaneous secular variation coefficients of the parent model, from 2018.5 to 2019.5 in 0.1 year increments, inclusive. This period was chosen to be as up-to-date as possible given the data used, while avoiding end-effects of the temporal B-spline parameterisation. These secular variation coefficients were then used to calculate the BGS main field coefficients at 2020.0, by propagating the instantaneous main field coefficients of the parent model at 2019.5 forward in time by six months.

2.3.3 VALIDATION PROCESS

Each parent model was validated by comparing it to other similar recent models (developed by NCEI, BGS and other organizations, e.g. for the International Geomagnetic Reference Field) and to a global set of geomagnetic observatory data. Inter-comparison of NCEI and BGS parent models provided a semi-independent validation of each model, as both models were derived using slightly different datasets and methods, and fully independent algorithms. The final coefficients were obtained by averaging the NCEI and BGS coefficients for the main field and the secular variation. The final model was again validated using the same approach as above before being approved for public release.

3. MODEL UNCERTAINTIES

The WMM2020 is valid for the period 1 January 2020 to 31 December 2024, from 1 km below the WGS 84 ellipsoid surface to approximately 850 km above it. Like any physical model, it contains uncertainties that must be carefully considered by its users. This section discusses the various sources of uncertainty for the WMM2020 and quantifies the uncertainties associated with each source at or near the Earth's surface. The uncertainties are then combined into a total error budget, which forms the basis of a simple error model providing the uncertainty for each component of the field. Note that the uncertainties are estimated at the Earth's surface so the WMM vertical validity range is approximate.

3.1 SOURCES OF UNCERTAINTY

Apart from human-made disturbances of the measurement, which are not discussed here, there are two sources of disagreement between magnetic field observations and the WMM. The first is due to inaccuracies in the model coefficients and is often referred to as the *commission* error. The second is due to the fact that the WMM does not account for all of the contributions to the observed magnetic field and is often referred to as the *omission* error.

The commission error is the sum of errors due to inaccuracies in main field coefficients, describing the field in 2020.0, and predictive secular variation coefficients, describing the linear part of the field variation from 2020.0 to 2025.0. Since the early 2000s, inaccuracies have been much reduced due to a series of high-precision magnetic survey satellites. However, in the case of the secular variation there is an additional error due to the fact that the true secular variation is not exactly linear. This is because changes of the fluid flow in the Earth's outer core lead to slightly nonlinear changes in the Earth's magnetic field. The nonlinear part of the secular variation is currently unpredictable, but, fortunately, it is small compared to the linear secular variation. It follows that, by surveying the field for several years, one can precisely map the present field and its rate of change, and then linearly extrapolate the rate out into the future for several years. Provided that suitable satellite magnetic observations are available, the prediction of the WMM is highly accurate on its release date and then subsequently deteriorates towards the end of the 5-year epoch, when it has to be updated with revised values of the model coefficients.

Non-linear core field variations are often related to short-lived, global increases in the power of the second order time derivative of the core field, a phenomenon referred to as a “secular acceleration pulse”. Over the past 20 years, high-quality, low-Earth orbit satellite data have provided an increasingly detailed picture of acceleration pulses (e.g., Chulliat and Maus, 2014). At least four pulses have been detected; these pulses were centered near 2006, 2009, 2012 and 2016 and lasted two to three years. They were strongest at mid-to-low latitudes and had spatially and temporally alternating polarity (i.e., for example, a positive secular acceleration in 2006 was followed by a negative one in 2009). At many magnetic observatories, pulses were preceded and/or followed by so-called “geomagnetic jerks”, or sudden changes in the secular variation rate of change at a given location. Geomagnetic jerks have long been observed and are ubiquitous in observatory data (e.g., Brown et al., 2013). Recent research suggests that acceleration pulses and at least some geomagnetic jerks might be related to hydromagnetic waves in the Earth’s core (e.g., Aubert and Finlay, 2019). When a large pulse occurs just after the release of the WMM, non-linear core field variations can lead to significant errors in the WMM predictions after a few years. Such was the case during the WMM2015 cycle; the issue was fixed by releasing an out-of-cycle update of the WMM (Chulliat et al., 2019).

The omission error is due to portions of the geomagnetic field that cannot be described by the WMM because either their spatial scale is too small or their time scale is too short. Most of these contributions are generated in the Earth’s crust and upper mantle, and in the ionosphere and magnetosphere, whereas the long-wavelength portion of the Earth’s magnetic field represented by the WMM originates within the Earth’s fluid outer core. Sources in the crust and upper mantle produce static spatial anomalies, and sources in the ionosphere and magnetosphere produce rapidly varying disturbance fields, either global or regional. The omission error is the largest contributor to the total error (see [section 3.2](#)) and can reach very large values in some locations and at certain times. For example, differences between the observed declination and the WMM can exceed 10 degrees. Anomalies of this magnitude are uncommon but do exist. Declination anomalies on the order of 3 or 4 degrees are not uncommon but are usually of small spatial or temporal extent.

On land, spatial anomalies are produced by mountain ranges, ore deposits, cloud to ground lightning, geological faults, etc. The corresponding deviations are usually smaller at sea, increase with increasing latitude, and decrease with increasing altitude of an air- or spacecraft. In ocean areas these anomalies occur most frequently along continental margins, near seamounts, and near ocean ridges, trenches and fault zones, particularly those of volcanic origin.

Since the crustal field is almost constant in time, it can be inferred from all available satellite, marine and aeromagnetic measurements of the past decades. These data have been compiled into a spherical harmonic degree-790 Enhanced Magnetic Model (EMM), available at <https://www.ngdc.noaa.gov/geomag/EMM>. Developed as research models for NGA, the EMM2017 provides consistent global representation of the magnetic field, including the crustal field, down to wavelengths of approximately 51 kilometers. The WMM subroutine library was designed so that it can be used with the EMM. Use of the EMM should be considered in applications with higher demands in pointing accuracy.

3.2 ESTIMATING UNCERTAINTY

Various approaches were used to estimate the WMM2020 uncertainty. Some approaches provide the uncertainties associated with one type of error and/or one omitted source, while others provide combined uncertainties for different sources. It is important to recognize that the omission error, particularly the one associated to the crustal field, dominates over the commission error, and that the omitted sources are only partially sampled in space and time. Therefore, it is not possible to precisely estimate the WMM2020 uncertainty in every location at the Earth's surface. What is achievable is a global estimate of the uncertainty, based upon a statistical analysis of the differences between the WMM2020 and its predecessors and independent geomagnetic measurements in as many locations as possible at the Earth's surface.

3.2.1 FORMAL COMMISSION ERROR

The errors on the Gauss coefficients of the WMM2020 can be formally estimated from the variance-covariance matrix of these coefficients, defined as

$$\underline{C} = (\underline{J}^T \underline{W} \underline{J})^{-1} \quad (25)$$

where \underline{J} is the Jacobian matrix of the nonlinear least squares penalty function used when calculating the NCEI parent model, and \underline{W} is a diagonal weighting matrix whose entries are given by $w_i = 1/\sigma_i^2$, with σ_i the error of the i -th measurement. The measurement error is the sum of the instrument error and the error caused by un-modeled fields at satellite altitude. A total measurement error σ was estimated using the final Gauss coefficients of the model as the RMS

(root mean square) of the differences between measurements and model predictions. This total error was assigned to each measurement in the weighting matrix.

The errors on the Gauss coefficients were then propagated to errors in magnetic field elements X , Y , Z , H , F , I and D . Taking for example the X element, and computing its model prediction as a set of points all over the Earth's surface will yield a vector X . This vector is linearly related to the Gauss coefficients (see equations 10, 11 and 12 in [section 1.2](#)) and so we can write $X = \underline{A} g$ for a matrix \underline{A} . The variance-covariance matrix of the X element will then be

$$\underline{C}_X = \underline{A} \underline{C} \underline{A}^T \quad (26)$$

Similar expressions exist for the Y and Z elements. The diagonal elements of this matrix then give us estimates of the commission error for our chosen set of measurement points. The X , Y and Z errors can then be propagated to obtain the errors in H , F , I , D and GV (north and south). The global RMS commission errors are given in Table 10.

Table 10: Formal commission errors at Earth's surface.

Row		X (nT)	Y (nT)	Z (nT)	H (nT)	F (nT)	I (°)	D (°)	GV (°)
1	Formal commission error at 2020.0	0.13	0.20	0.25	0.13	0.24	0.00	0.00	0.00
2	Formal commission error at 2025.0	0.49	0.76	0.92	0.49	0.88	0.02	0.00	0.02

3.2.2 COMMISSION ERROR FROM MODEL COMPARISONS

As different data and modelling approaches are used by BGS and NOAA, some insight into the errors arising from incorrect modelling and prediction of the core field signal up to degree 12 can be gained by inter-comparing their respective models and by comparing preliminary and final WMM2020 with WMM2015 (original version, referred to as WMM2015v1 in what follows) and WMM2015v2 (out-of-cycle update, cf. Chulliat et al., 2019). These comparisons are done by computing the component values on a 1° latitude/longitude grid (defined using geocentric latitude),

and calculating RMS differences weighted by the cosine of the latitude. The north and south BoZs (as defined in [section 1.7](#)) are excluded from declination and grid variation (north and south) calculations. Table 11 lists these differences.

Note the large GV_N and GV errors at the end of the 2015-2020 interval (Table 11, rows 3a and 6a) for the WMM2015v1 model, compared to the same errors for WMM2010 at 2015.0 (row 6c). These errors were related to the fast drift of the north magnetic dip pole during the 2015-2020 cycle, and the occurrence of a geomagnetic jerk at the beginning of that cycle. GV_S errors were much smaller, reflecting a slower drift of the south dip pole. The detection of large grid variation errors as part of the regular performance assessment of WMM2015v1 prompted the development and release of the WMM2015v2 out-of-cycle update. The new model significantly reduced the commission error for all components, including GV_N and GV (rows 3b and 6b). Note also the significantly larger errors for all components incurred by the WMM after ten years (rows 7a, 7b and 8).

Table 11: RMS differences at Earth's surface. These approximate the core field contributions to overall errors. Note increase in error if model not updated every 5 years (rows 7 and 8).

Row		Date	X (nT)	Y (nT)	Z (nT)	H (nT)	F (nT)	I (°)	D (°)	GV (°)	GV_N (°)	GV_S (°)
1	NOAA prelim 3 Oct – BGS prelim 3 Oct	2020.0	4	4	7	4	5	0.01	0.02	0.03	0.04	0.02
2	NOAA prelim 3 Oct – BGS prelim 3 Oct	2025.0	32	37	58	30	36	0.08	0.12	0.20	0.20	0.19
3a	WMM2020prelim – WMM2015v1	2020.0	45	56	89	47	67	0.12	0.22	0.42	0.57	0.16
3b	WMM2020prelim – WMM2015v2	2020.0	9	14	20	9	11	0.03	0.04	0.06	0.07	0.05
4	NOAA final – BGS final	2020.0	3	3	5	3	4	0.01	0.01	0.03	0.04	0.02
5	NOAA final – BGS final	2025.0	24	24	40	23	27	0.06	0.10	0.20	0.24	0.16
6a	WMM2020 – WMM2015v1	2020.0	46	56	89	47	67	0.12	0.22	0.41	0.56	0.16

6b	WMM2020 – WMM2015v2	2020.0	9	15	21	9	11	0.03	0.04	0.06	0.07	0.04
6c	WMM2015- WMM2010	2015.0	46	50	79	47	60	0.10	0.17	0.35	0.42	0.25
7a	WMM2020 – WMM2015v1	2025.0	108	136	213	111	157	0.28	0.53	0.98	1.33	0.42
7b	WMM2020 – WMM2015v2	2025.0	40	64	92	40	43	0.14	0.17	0.26	0.31	0.19
8	WMM2020 – WMM2010	2020.0	104	120	186	109	154	0.25	0.49	1.02	1.36	0.49

The differences between WMM2015v1 and WMM2015v2 and WMM2020 predictions for the magnetic field at 2020.0 are shown in Figures 6 and 7. The spatial distribution of differences is not necessarily an indication of where the largest errors will occur in the future. However, the largest errors in declination and grid variation will again be concentrated near the magnetic poles where the strength of the horizontal component of the field is lowest.

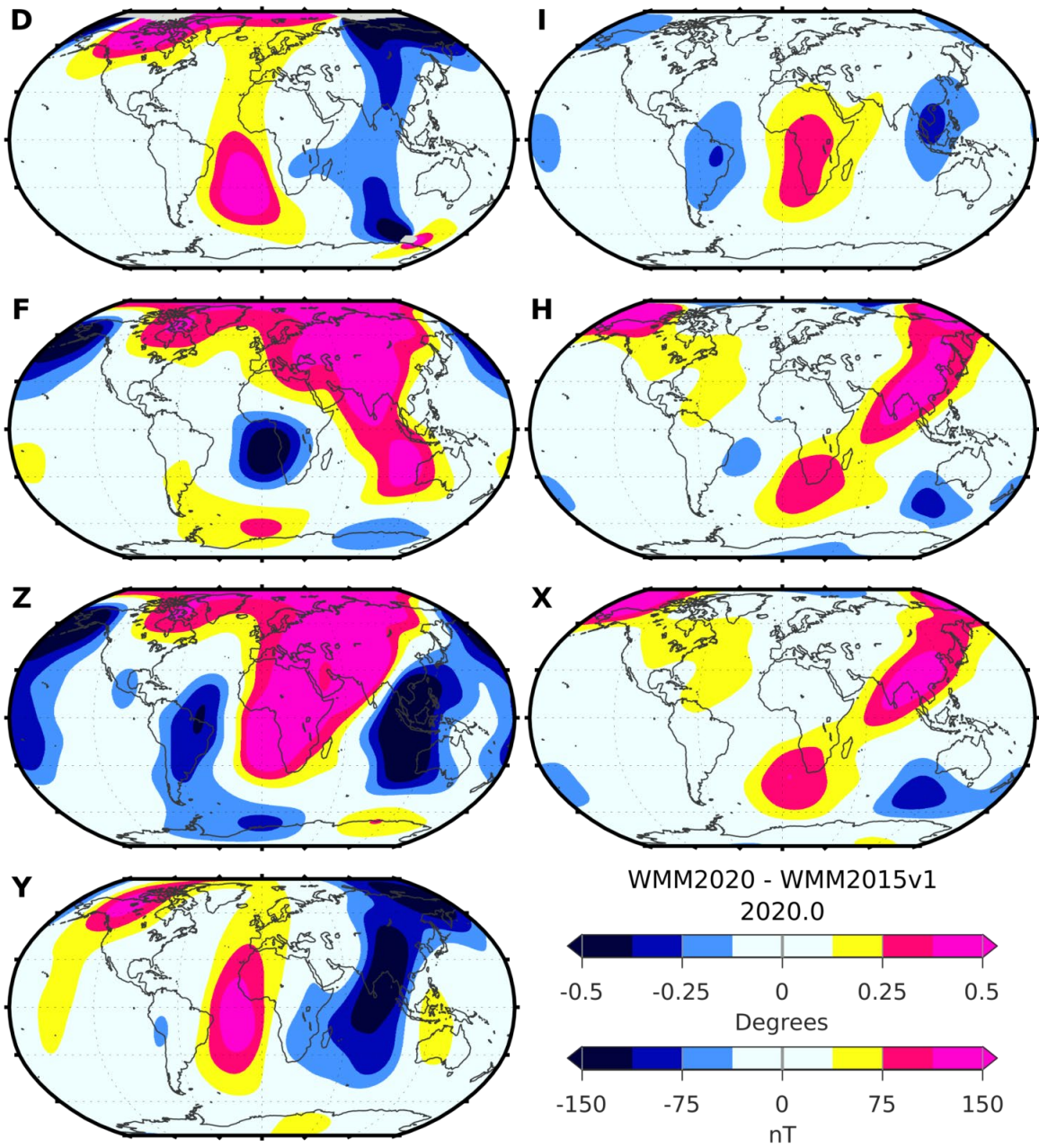


Figure 6: Differences between WMM2020 and WMM2015v1 at mean Earth radius, at 2020.0. BoZ is shown as light grey areas around dip poles in declination map.

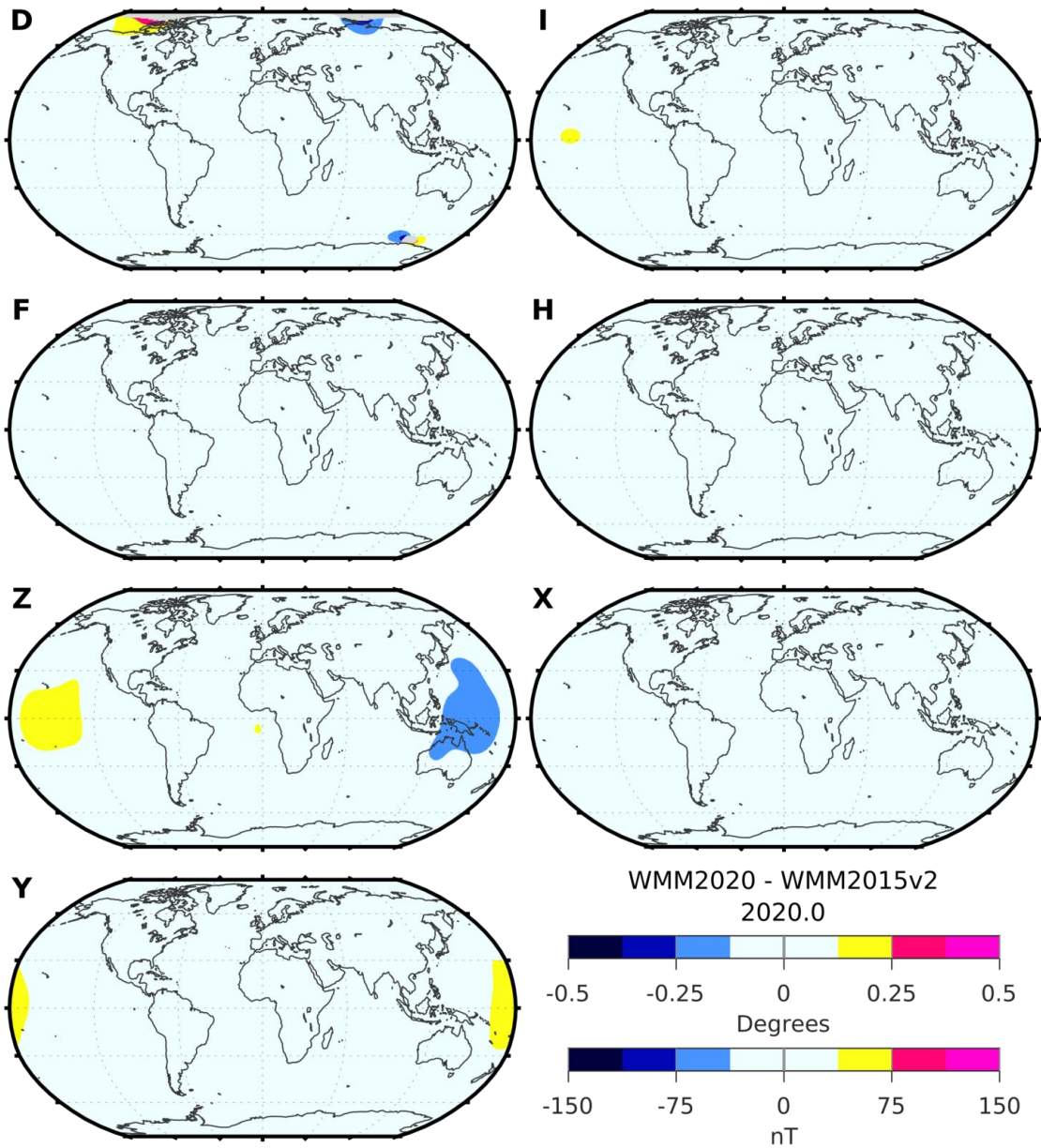


Figure 7: Differences between WMM2020 and WMM2015v2 at mean Earth's radius, at 2020.0. BoZ is shown as light grey areas around dip poles in declination map.

To further demonstrate the difficulty in modelling declination near the magnetic poles the differences in declination between the two parent models from BGS and NOAA, truncated at degree 12, at 2020.0 and 2025.0 are shown in Figures 8 and 9.

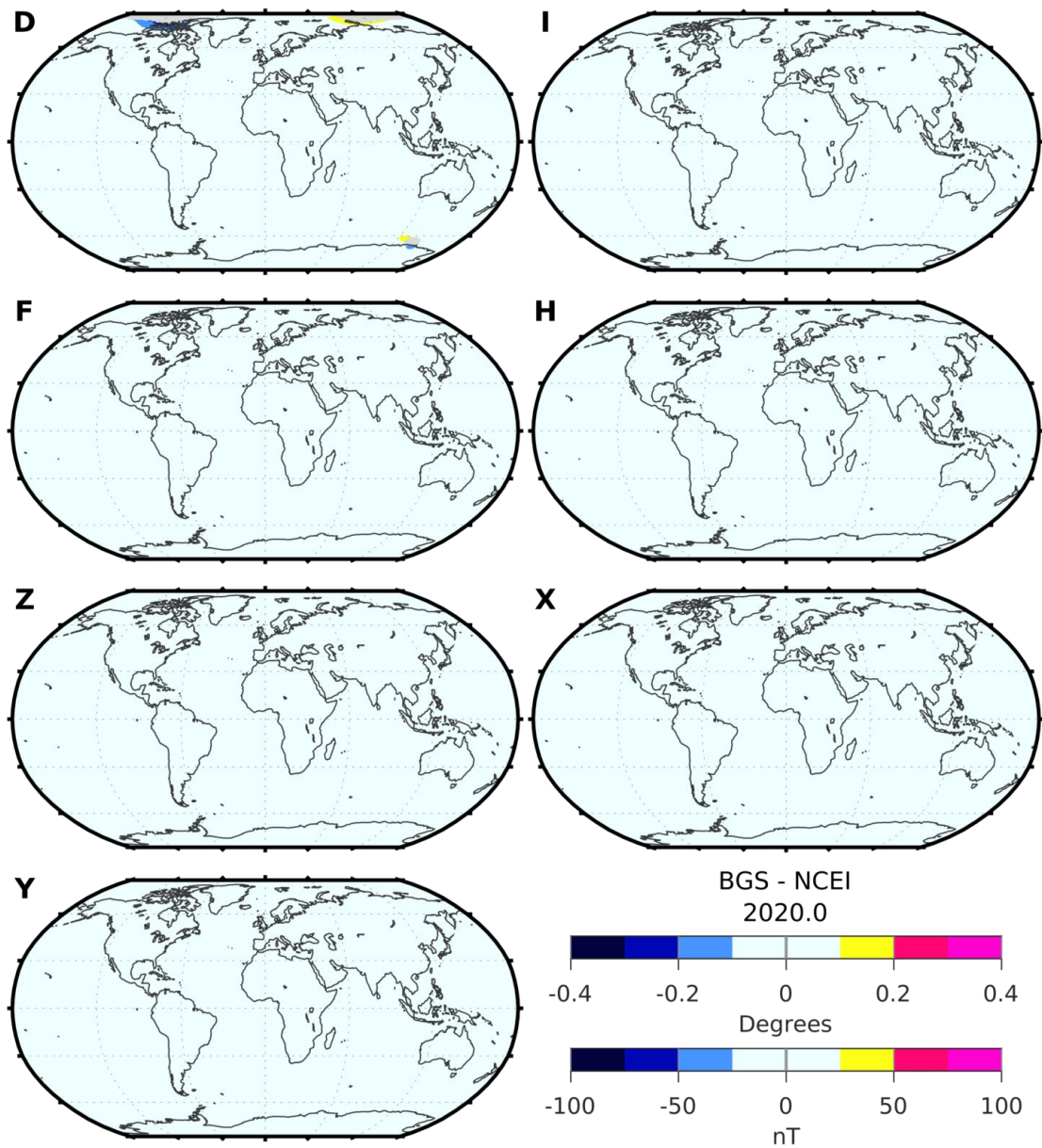


Figure 8: Differences between BGS and NCEI final main field models at mean Earth's radius, at 2020.0. BoZ is shown as light grey areas around dip poles in declination map.

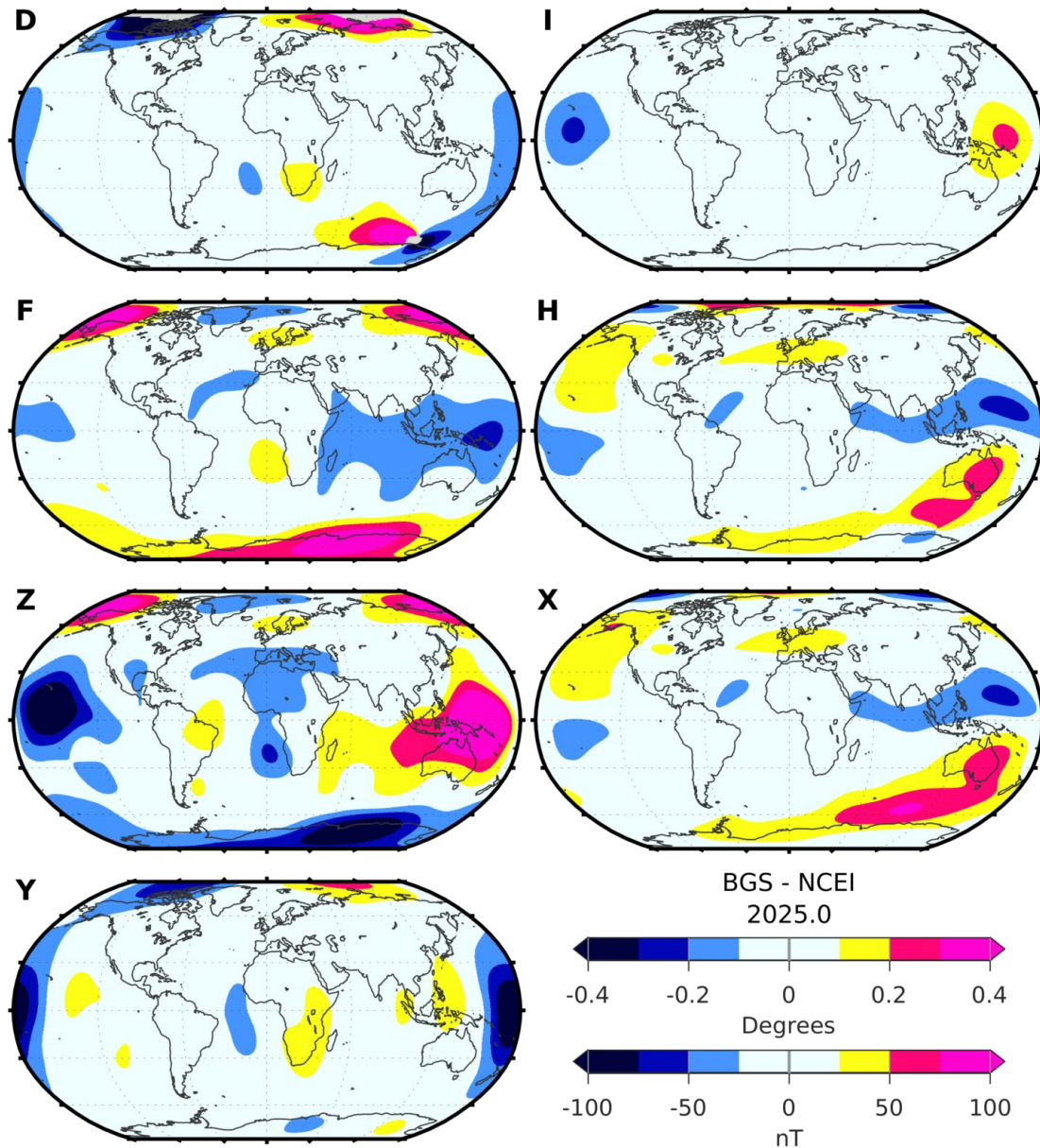


Figure 9: Differences between BGS and NCEI final main field models at mean Earth's radius, at 2025.0. BoZ is shown as light grey areas around dip poles in declination map.

3.2.3 CRUSTAL FIELD CONTRIBUTION – METHOD #1

The crustal field is the largest source of uncertainty of the WMM near the Earth's surface. Although high resolution crustal field models (such as the EMM) exist, they only describe the largest spatial scales of the crustal field. Therefore, any rigorous attempt to quantify the crustal field contribution to the omission error should rely on actual field measurements. A first method

for estimating the crustal field error consisted in comparing past WMM predictions with (a) trackline data from 189 aeromagnetic and marine surveys archived in NGDC's GEODAS (GEOphysical DATA System) and collected over 2000-2014, and (b) data from 175 geomagnetic observatories archived at BGS's World Data Centre for Geomagnetism in Edinburgh and collected over 2000-2018. (Step (a) is identical to the error analysis reported in the WMM2015 Technical Report; step (b) is an updated and improved version.)

Trackline data have several advantages compared to observatory data when investigating the crustal field error. First, they sample the crustal field at a much larger number of points. The GEODAS dataset used for this analysis includes a total of 6,857,662 data points at different locations, to be compared with 175 observatory locations. Second, trackline data are typically acquired a few kilometers above the crustal field sources (due to the plane altitude or the depth of the ocean below the survey vessel), which reduces the amplitude of the smallest spatial scales of the field, including very local human-made anomalies. There are disadvantages, however, as only total field data are available from marine and aeromagnetic surveys and it is generally impossible to separate the crustal field from the external field in such data. The following analysis is an attempt at combining advantages from both trackline and observatory datasets.

As a first step, residuals between trackline data and past WMM predictions over 2000-2014 were calculated and sorted according to absolute corrected geomagnetic latitude. Overall, the residuals were found to be normally distributed. RMS values of residuals within each 10 degrees latitudinal bin were then calculated. The obtained values (Figure 10) include both the commission error (mostly the error due to incorrect prediction of the secular variation over each WMM five-year time interval, see [section 3.2.2](#)) and the omission error, with contributions from both the crustal field and the external field. There is a small but clear dependence of the error with latitude, partly due to an increase of the crustal field strength with latitude, as shown by models such as the degree-790 Enhanced Magnetic Model (EMM), and partly due to the effect of the external field which becomes larger on average near 65° geomagnetic latitude (see [section 3.2.5](#)).

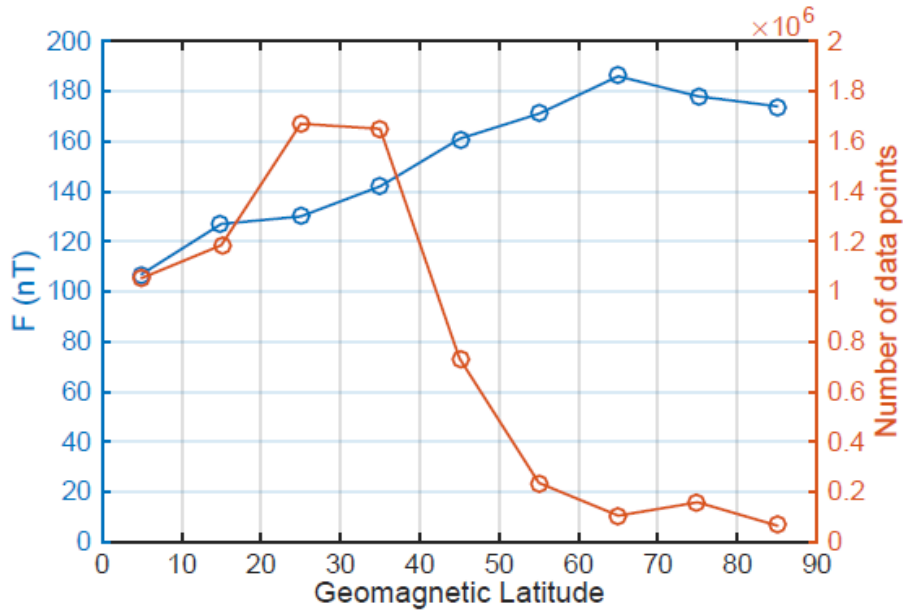


Figure 10: RMS differences between trackline data and WMM for years 2000-2014, sorted according to absolute corrected geomagnetic latitude (Richmond, 1995), and corresponding number of data in each 10 degrees latitudinal bin.

As a second step of the analysis, hourly mean values from 175 observatories over 2000-2018 were least-square fitted by cubic splines with knots every year. This procedure removes most of the external field, which varies with timescales smaller than one year, except for some small external fields varying with the 11-year solar cycle. Each spline fit therefore represents the sum of the crustal and core fields at the observatory location. RMS differences between spline fits and WMM predictions were then calculated for each component within 10° latitudinal bins. The RMS error on F was found much larger than the one from trackline data; for example, the RMS error for the 10 to 50 degrees latitude bin (i.e., the four 10 degrees latitude bins between 10 and 50 degrees) is 383 nT, compared to 137 nT from trackline data. This result reflects the very heterogeneous spatial distribution of the global observatory network, which includes observatories located on top of large amplitude but small size crustal field anomalies such as basaltic islands. In order to circumvent this limitation, observatory data were selected so that the resulting RMS error on F matches the one obtained from trackline data in the 10 to 50 degrees latitude bin. This bin is where the external field is expected to have its smallest contribution to trackline data and where most data are available. A robust outlier detection algorithm was used to achieve this observatory selection, leading to the selection of 86 out of 112 observatories in the 10 to 50 degrees bin, and a total of 134 out of 175 observatories for all latitudes. The weighted RMS error values for each component are given in Table 12 (rows 1 and 2). Note that grid variation north (GV_N) and south (GV_S) are not separated in Table 12 as (a) the dominant source of error is the unmodeled crustal field which is assumed to be of the same order of magnitude in both hemispheres, and (b) there was not enough data to robustly

separate GV_N and GV_S . Observatories in the north and south BoZs (as defined in [section 1.7](#)) were excluded from this analysis.

In order to separate error contributions from the crustal field and the secular variation, RMS differences between spline fits and WMM predictions were calculated on the first day of each model epoch (2000.0, 2005.0, 2010.0 and 2015.0), and for the same 134 out of 175 observatories selected when calculating RMS differences over the full 2000-2018 interval. The results are crustal field only error values and are provided in Table 12 (row 3). Corresponding secular variation error values (row 4) were obtained by subtracting row 3 from row 2 in quadrature.

Table 12: RMS differences between observatory data and WMM for years 2000-2018 (rows 1 and 2) and for epochs 2000.0, 2005.0, 2010.0 and 2015.0 (row 3), after selection of observatories such that the RMS error on F is the same as that from trackline data in the 10 to 50 degrees corrected geomagnetic latitude bin. Row 4 is obtained by subtracting row 3 from row 2 in quadrature.

Row		X (nT)	Y (nT)	Z (nT)	H (nT)	F (nT)	I (°)	D (°)	GV (°)
1	Crustal field and secular variation; 86/112 observatories in the 10-50 degrees corrected geomagnetic latitudes bin	159	70	155	158	137	0.22	0.18	N/A
2	Crustal field and secular variation; 134/175 observatories at all latitudes	151	94	153	152	143	0.20	0.38	0.71
3	Crustal field only; 134/175 observatories at all latitudes	147	91	133	146	130	0.18	0.38	0.71
4	Inferred secular variation; 134/175 observatories at all latitudes	35	24	76	42	60	0.09	0.01	0.03

3.2.4 CRUSTAL FIELD CONTRIBUTION – METHOD #2

World Magnetic Models/World Chart Models since 1980 (the first time charts were produced jointly between U.K. and U.S.) were compared with compilations of ground-based vector data. Each of the seven models comprises main-field coefficients at a base epoch and predictive

secular variation coefficients valid for the following five years. Two data compilations were used in the comparison: (1) repeat station and land survey data and (2) observatory annual means. Both compilations are from the World Data Centre for Geomagnetism (Edinburgh) and have only modest contamination from external fields, as data are mostly reduced to quiet night time or annual mean equivalents in (1) and annual averaging smooths out much of the unwanted signal in (2). The reason for going so far back in time was to achieve a better spatial coverage. This is still far from ideal but is shown in Figure 11.

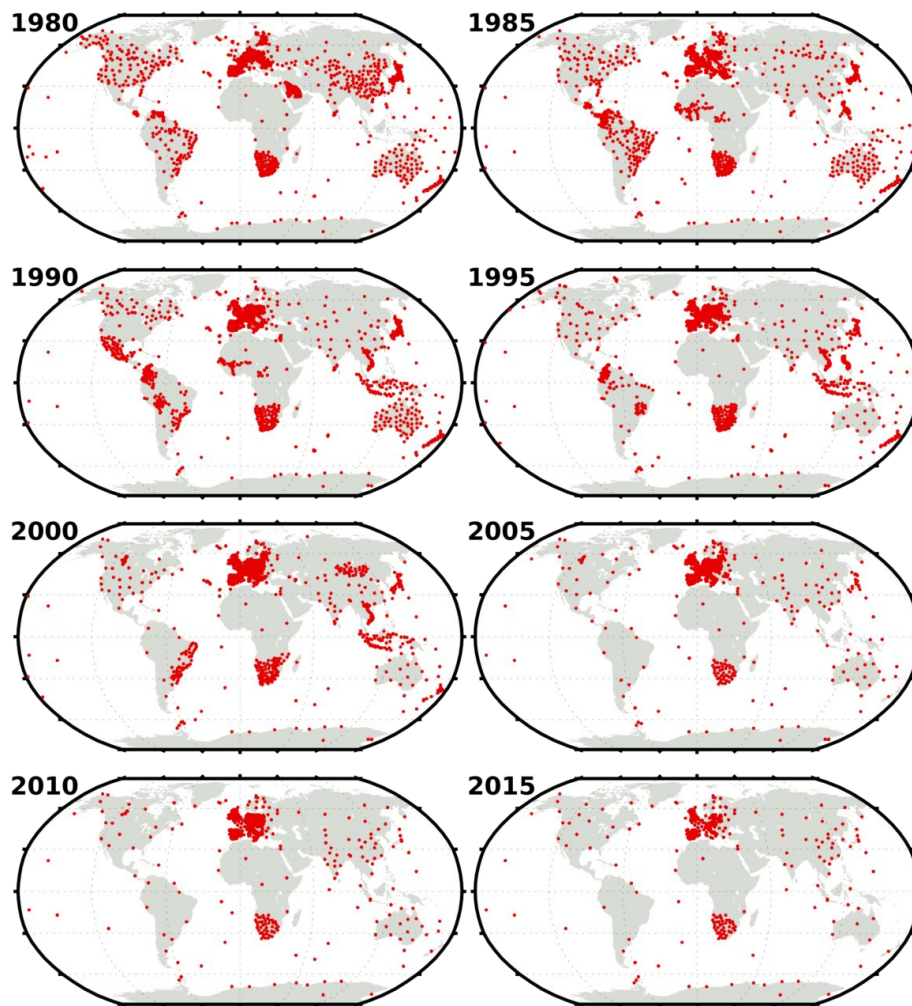


Figure 11: The locations of repeat stations, vector land surveys and observatories that provided data for model comparisons. Maps show locations of data in the 5 year WMM period from each date shown.

RMS differences were computed for all seven elements, and for each of the eight models after elimination of outliers (any differences greater than 3 standard deviations). The sample sizes vary according to the element but are greater than 20000. Table 13 (row 1) lists these RMS

differences. Note that there was not enough data to robustly separate grid variation north (GV_N) and south (GV_S) in this analysis. Also, no data were used in the north and south BoZs (as defined in [section 1.7](#)). In an approach similar to that used in [section 3.2.3](#), RMS differences were calculated on the first year of each model epoch to determine the contribution to the error from the crustal field only. The results are reported in Table 13 (row 2).

The contribution to the overall error budget for the WMM from the crustal field estimated here using vector data collected on land is conservative, i.e. over-cautious. One way of justifying the use of lower values is to employ near-surface scalar data, i.e., total intensity. These data are plentiful as they are relatively easy to collect from ships and aircraft and, importantly, they cover both land and sea. Global scalar anomaly compilations have been made in recent years, for example the World Digital Magnetic Anomaly Map (WDMAM, Lesur et al., 2016) and NOAA’s Earth Magnetic Anomaly Grids EMAG2 (Maus et al., 2009) and EMAG2v3 (Meyer et al., 2017). The mean absolute differences for F derived from the land-based vector observations can be compared with those from global compilations. For WDMAM (version 2) the mean absolute anomaly in F is 107 nT, for EMAG2 it is 105 nT and for EMAG2v3 it is 83 nT. These are likely to be underestimates at the Earth’s surface because these compilations are above the surface at 5 km and 4 km, respectively. However, even if these were to be downward-continued to the Earth’s surface they would not be as high as the value from the repeat stations and observatories (201 nT). Another source of scalar data is NOAA’s GEODAS (GEOphysical DATA System), as described in [section 3.2.3](#). For 2000 onwards, the spatial distribution of these data is not as good as that of the WDMAM and EMAG2, but they are collected at the Earth’s surface. The RMS difference between these data over 2000-2014 and the relevant WMM is 137 nT.

Following the same approach as in the WMM2015 Technical Report, the values from the repeat stations and observatories are scaled according to the mean of the RMS difference from EMAG2 and the GEODAS surveys (121 nT) and are shown in Table 13 (row 3).

Table 13: RMS differences between observations and models in World Magnetic Model series since 1980, using all data (row 1) or only data collected on the same year as the model epoch (row 2). Row 3 is obtained by rescaling row 2 values so that the RMS difference on the F component is equal to 121 nT. (All components are rescaled using the same ratio.)

Row		X (nT)	Y (nT)	Z (nT)	H (nT)	F (nT)	I (°)	D (°)	GV (°)
1	Crustal field and secular variation; repeat stations plus	165	146	306	158	193	0.33	0.41	0.57

	observatories WMM1980 onwards								
2	Crustal field only; repeat stations plus observatories WMM1980 onwards 1 st year only	161	125	255	157	201	0.36	0.36	0.51
3	Rescaled crustal field only, according to information from EMAG2 and GEODAS	97	75	154	95	121	0.22	0.22	0.31

3.2.5 DISTURBANCE FIELD CONTRIBUTION

The disturbance field is the sum of the contributions of ionospheric and magnetospheric electric currents, plus the corresponding contributions from currents induced by the external time-varying magnetic fields in the Earth and oceans. The strength of the disturbance field is modulated by the 11-year solar cycle. Periods of strong magnetic activity (magnetic storms) occur primarily at solar maximum, although they tend to lag behind the solar cycle by about two years. The epoch of WMM2020 starts in the quietest part of the solar cycle (near the end of Solar Cycle 24) and extends into an increasingly more active part (the ascending phase of Solar Cycle 25).

The contribution from the disturbance field to the WMM uncertainty was estimated from hourly mean values recorded at 175 magnetic observatories over 2000-2018 (see [section 3.2.3](#)). RMS residuals between the data and the cubic spline fit over 2000-2018 were calculated for each observatory and each component. The obtained variation with latitude (Figure 12) is in good agreement the known properties of the external field. Near the geomagnetic equator, the northern external field is enhanced by the so-called equatorial electrojet, a strong electrical current flowing at 110 km altitude along the equator. At higher latitudes, near 65° geomagnetic latitude, intense auroral electrojets can lead to variations as large as several thousands of nT during geomagnetic storms. However, on average, the contribution of the external field to the total error is much smaller than that of the crustal field and for this reason its latitude dependency is neglected in what follows. The global RMS error values for each component are given in Table 14.

Table 14: RMS residuals, attributed to the external field, between observatory data and spline fits for each component and for the years 2000-2018.

Row		X (nT)	Y (nT)	Z (nT)	H (nT)	F (nT)	I (°)	D (°)	GV (°)
1	RMS external field contribution from 175 observatories at all latitudes	37	23	27	37	29	0.04	0.22	0.44

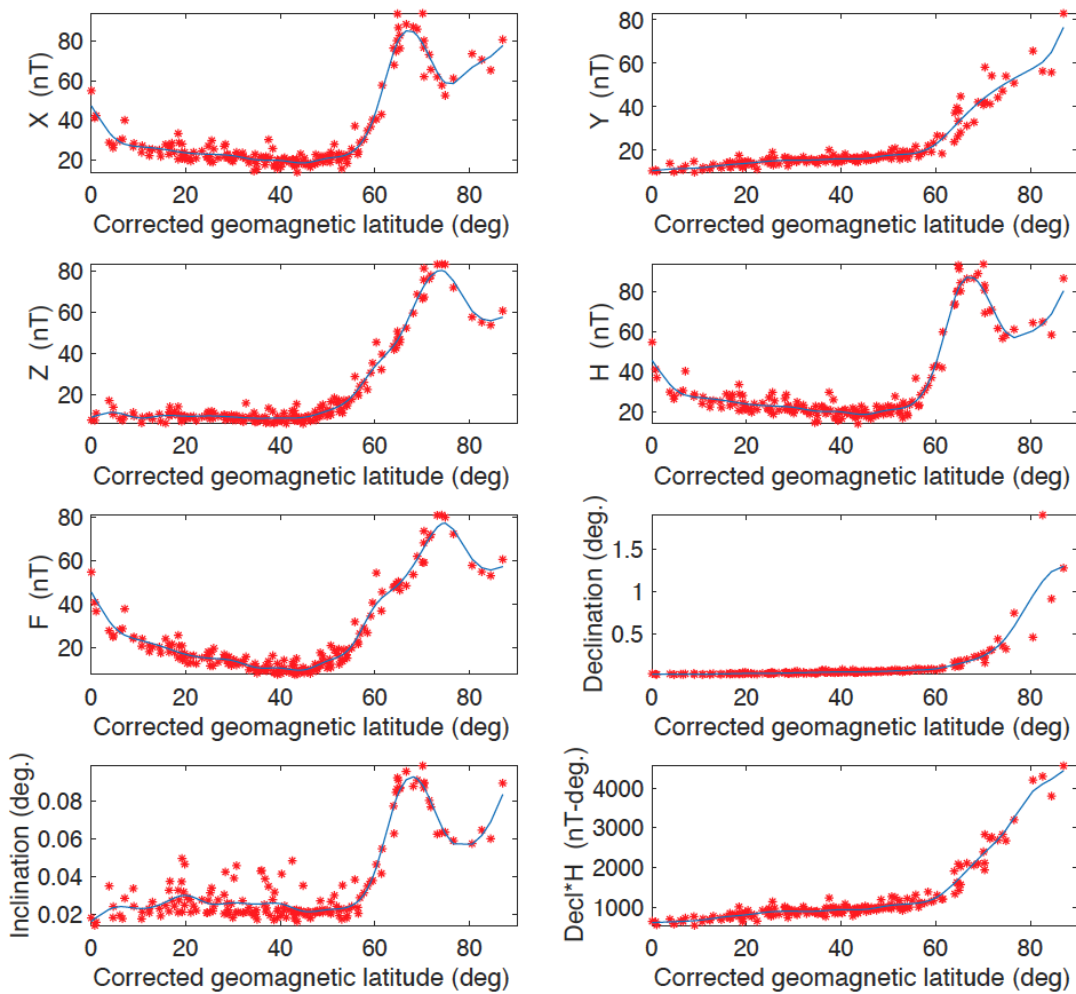


Figure 12: Variation with corrected geomagnetic latitude of the RMS residuals between observatory data and spline fits for the various field components and for the years 2000-2018.

3.3 TOTAL ERROR BUDGET

The results of the error analysis are summarized in Table 15:

- Although a formal commission error can be calculated (Table 10), a more realistic estimate of the commission error at 2020.0 (Table 15, row 2) is provided by taking RMS differences of the final NOAA and BGS models for that epoch (Table 11, row 9).
- The commission error at 2025.0 (Table 15, row 3), which is dominated by the secular variation forecasting error over the next five years, is obtained by averaging the RMS differences between WMM2020 and WMM2015v1 at 2020.0 (Table 11, row 6a), and the RMS differences between WMM2015 and WMM2010 at 2015.0 (Table 11, row 6c). These quantities correspond to the true secular variation forecasting errors over each of the past two WMM cycles for each component.
- The two methods used for obtaining the crustal field contribution have complementary merits and limitations. Therefore, we averaged the results from both methods (Table 12, row 3 and Table 13, row 3) to obtain a final estimate for the crustal field omission error (Table 15, row 4).
- The disturbance field omission error (Table 15, row 5) is the one reported in Table 14.

Since these errors are statistically independent, the expected total errors at 2020.0 (row 6) and 2025.0 (row 7) are calculated as the root of the sum of squares of rows 2, 4 and 5, and rows 3, 4 and 5, respectively. For example, the total error at 2020.0 between the observed and modeled declination is estimated to be

$$\sqrt{0.01^2 + 0.30^2 + 0.22^2} = 0.37^\circ \quad (27)$$

Note that all error values increase between 2020 and 2025 due to the secular variation forecasting error at the end of the WMM validity interval. The largest relative increase occurs for GV_N ; it is related to the fast drift of the north magnetic dip pole, as noted in [section 3.2.2](#).

The accuracy requirements for the WMM are detailed in the military specification MIL-W-89500B (Department of Defense, 2019) and are provided in row 1 of Table 15. In summary, the requirement is that the global RMS difference between the WMM and the observed magnetic field on the WGS 84 ellipsoid surface should be within 1° for D , I , GV_N and GV_S , within 200 nT for H and within 280 nT for F for the entire 5-year lifetime of the model. We find that the combined error values (rows 6 and 7) are all lower than the required values. During the WMM cycle, NCEI and

BGS regularly update the combined error estimates using the most recent data available to ensure that the model remains within specification.

Table 15: Estimated global RMS errors in WMM2020. Higher values of GV (compared to D) reflect the larger uncertainties of the declination at high latitudes, the only regions where GV is defined. Higher values of GV_N compared to GV_S reflect the faster drift of the north dip pole compared to the south dip pole.

Row		X (nT)	Y (nT)	Z (nT)	H (nT)	F (nT)	I (°)	D (°)	GV (°)	GV_N (°)	GV_S (°)
1	Military specification MIL-W-89500B	N/A	N/A	N/A	200	280	1.00	1.00	N/A	1.00	1.00
2	Commission error at 2020.0	3	3	5	3	4	0.01	0.01	0.03	0.04	0.02
3	Commission error at 2025.0	46	53	84	47	64	0.11	0.20	0.38	0.49	0.21
4	Crustal field omission error	122	83	143	120	126	0.20	0.30	0.51	0.51	0.51
5	Disturbance field omission error	37	23	27	37	29	0.04	0.22	0.44	0.44	0.44
6	Combined error at 2020.0	127	86	146	126	129	0.20	0.37	0.67	0.67	0.67
7	Combined error at 2025.0	135	101	168	134	144	0.23	0.42	0.77	0.83	0.70

3.4 ERROR MODEL

The WMM2020 comes with an error model providing uncertainty estimates for every geomagnetic element (X , Y , Z , H , F , I and D) and every location on the WGS 84 ellipsoid surface. This model is built upon the results of the error analysis (see [section 3.3](#)), while taking into account the geometrical relationships between the various components [formulas (19) in [section 1.2](#)].

The first part of the error model was built by taking the average of rows 6 and 7 of Table 15 as variances of the X , Y and Z components, and assuming that off-diagonal terms of the variance-covariance matrix for (X, Y, Z) are zero:

$$\delta X = 131 \text{ nT} \quad (28)$$

$$\delta Y = 94 \text{ nT} \quad (29)$$

$$\delta Z = 157 \text{ nT} \quad (30)$$

The error in (X, Y, Z) was then propagated onto (F, I, D, H) by linearizing the relationships (19) between (F, I, D, H) and (X, Y, Z) and neglecting the off-diagonal terms:

$$\delta H = \sqrt{[(\delta X)^2(\cos D)^2 + (\delta Y)^2(\sin D)^2]} \quad (31)$$

$$H \delta D = \sqrt{[(\delta X)^2(\sin D)^2 + (\delta Y)^2(\cos D)^2]} \quad (32)$$

$$\delta F = \sqrt{[(\delta H)^2(\cos I)^2 + (\delta Z)^2(\sin I)^2]} \quad (33)$$

$$F \delta I = \sqrt{[(\delta H)^2(\sin I)^2 + (\delta Z)^2(\cos I)^2]} \quad (34)$$

In order to remove non-physical variations in δH , δF and δI , these quantities were averaged over the WGS 84 ellipsoid yielding:

$$\delta H = 128 \text{ nT} \quad (35)$$

$$\delta F = 145 \text{ nT} \quad (36)$$

$$\delta I = 0.21^\circ \quad (37)$$

As expected, these values are close to the error budget values (Table 15), which suggests that the error analysis is consistent.

The case of δD is different, as H goes to zero at the North and South magnetic poles and therefore δD goes to infinity there. Adopting a global average for δD would thus seriously underestimate the declination error near the poles. To address this difficulty, the following formula was built:

$$\delta D = \sqrt{(0.26)^2 + (5625/H)^2} \quad (38)$$

where δD is expressed in degrees. This formula is such that:

- (1) At low-latitudes (i.e., for large H values), δD is close to the propagated δD averaged over all locations where $H \geq 5000$ nT (i.e., excluding areas where δD becomes very large due to the geometrical effect), which is equal to 0.30° . Specifically, 0.26° is obtained by taking $\sqrt{(0.30)^2 - (5625/41802)^2}$, so that $\delta D = 0.30^\circ$ where $H = 41802$ nT (maximum value at the Earth's surface).
- (2) Near the poles (i.e., for small H values), δD varies like the global average of the propagated $H \delta D$, which is equal to 5625 nT, divided by H .

A global map of the corresponding declination error is provided in Figure 13. At mid- to low-latitudes, the error is close to or slightly lower than the average of the 2020.0 and 2025.0 error budget values (0.37° and 0.42° , respectively, cf. Table 15, rows 6 and 7). The error becomes larger near the magnetic dip poles and in an area close to South Africa where the horizontal field is very low. The average value of the D error from equation (38) is equal to 0.43° which is close to the error budget value.

The final error model is thus made of equations (28)-(30) and (35)-(38). The uncertainties in X , Y , Z , H , F and I are assumed to be constant over the globe, while the uncertainty in D is assumed to vary with location. All uncertainties are assumed to be constant with altitude in the model validity range (from 1 km below the WGS 84 ellipsoid surface to approximately 850 km above it).

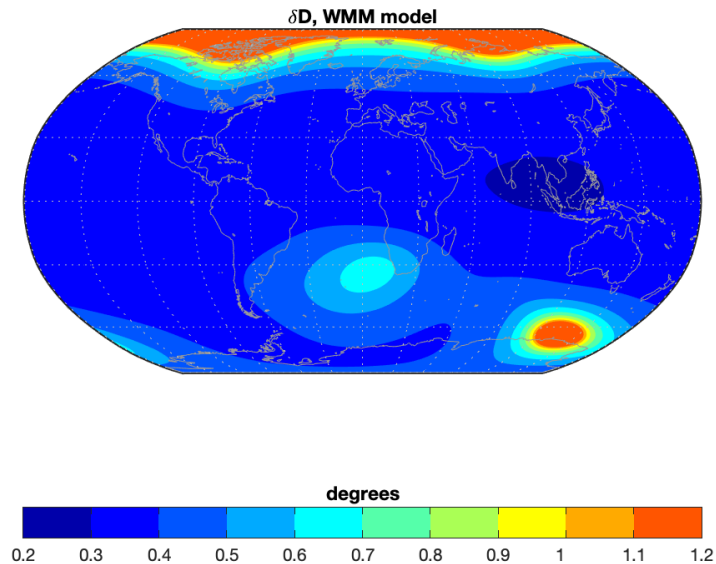


Figure 13: Global distribution of the declination error provided by the WMM2020 error model. The color scale is limited to a maximum value of 1.2° ; the error becomes larger than this near magnetic poles.

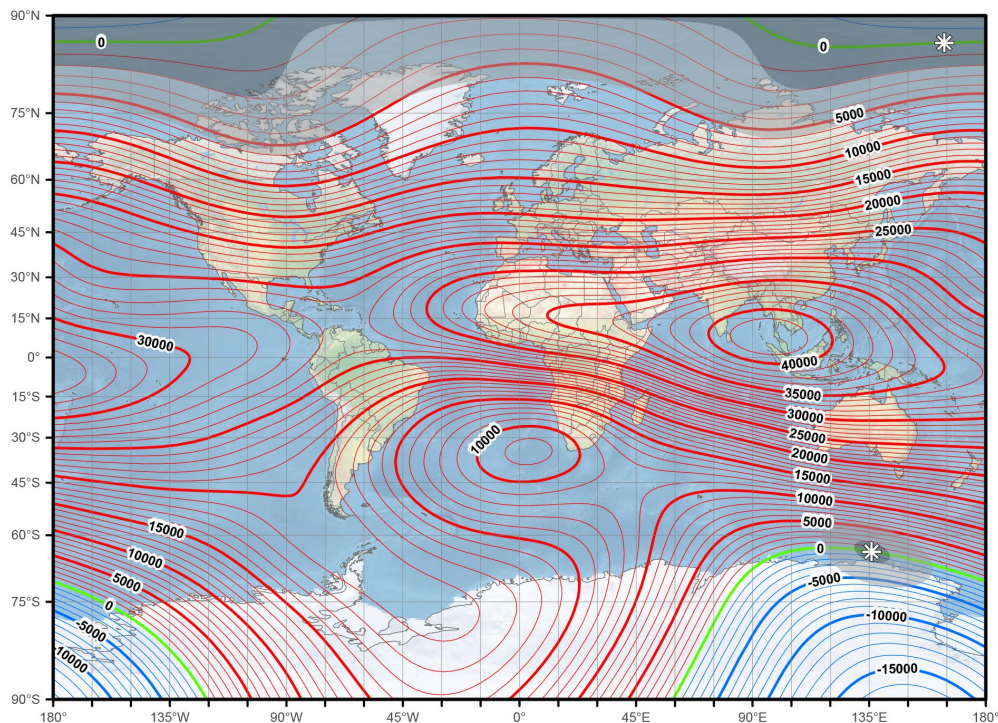
4. CHARTS

This section provides the WMM2020 charts in the following order:

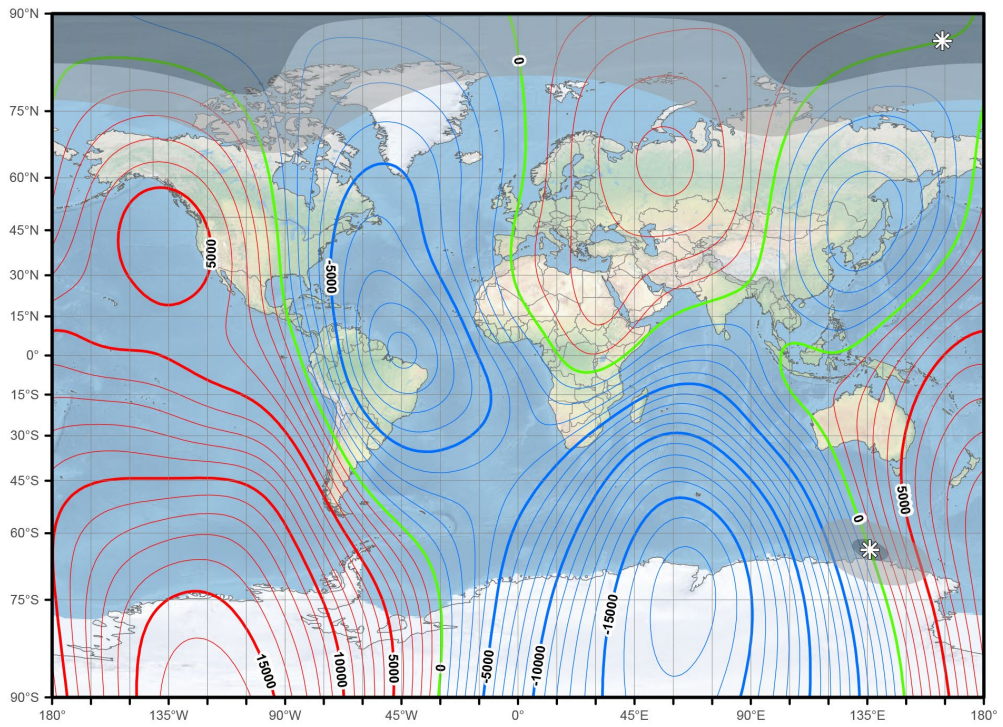
- Main field maps for 2020.0 in Miller projection for *X*, *Y*, *Z*, *H*, *F*, *I* and *D* (see pgs. 70-73)
- Main field maps in north polar stereographic projection (see pgs. 74-80)
- Main field maps in south polar stereographic projection (see pgs. 81-87)
- Secular variation maps for 2020.0 – 2025.0 in Miller projection for *X*, *Y*, *Z*, *H*, *F*, *I* and *D* (see pgs. 88-91)
- Secular variation maps in north polar stereographic projection (see pgs. 92-98)
- Secular variation maps in south polar stereographic projection (see pgs. 99-105)
- Grid variation maps in polar stereographic projection (see pgs. 106-109)
- Geomagnetic longitude and latitude in Miller projection (see pg. 110)

The white stars on the maps indicate the 2020.0 positions of the dip poles. The blackout (resp. caution) zones are shown as dark (resp. light) shaded areas.

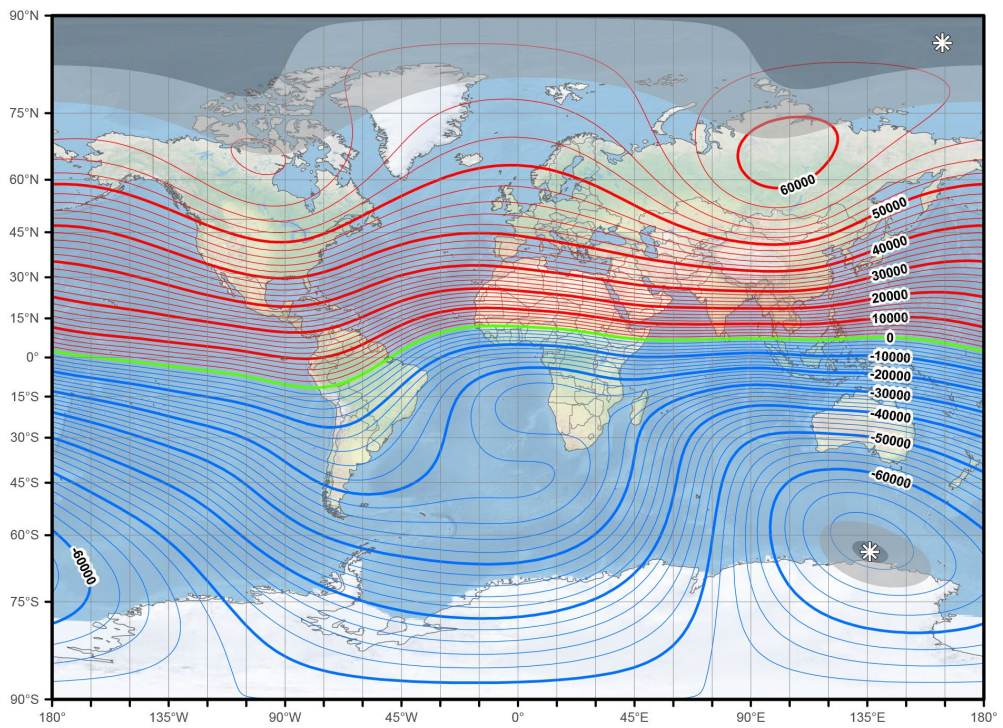
MAIN FIELD MAPS: MILLER PROJECTION



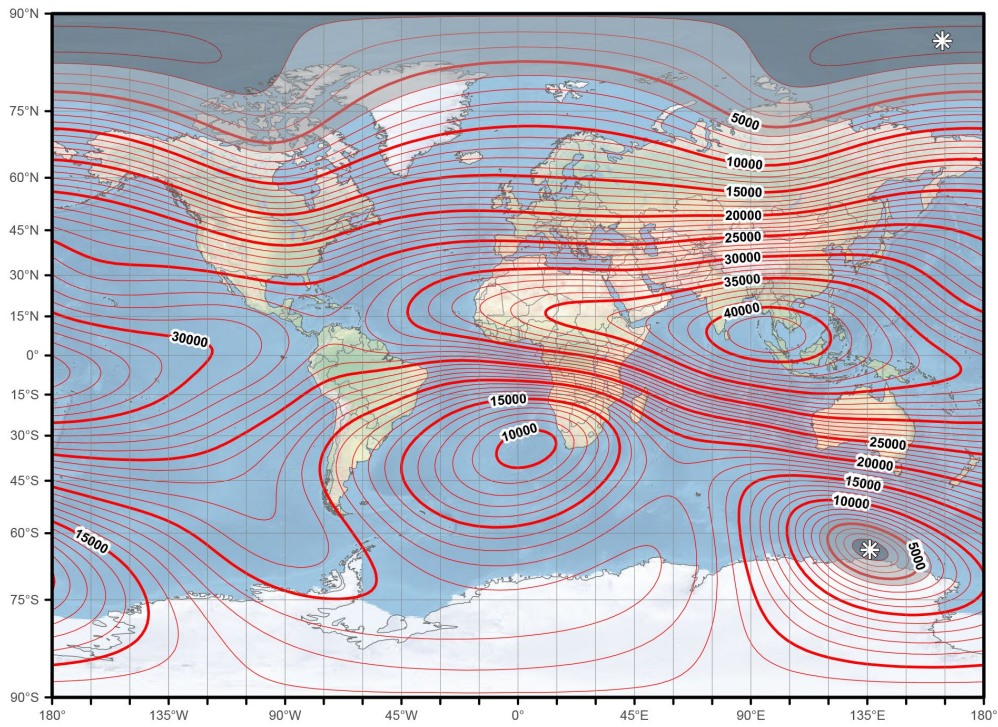
Main field north component (*X*). Contour interval is 1000 nT. Miller projection.



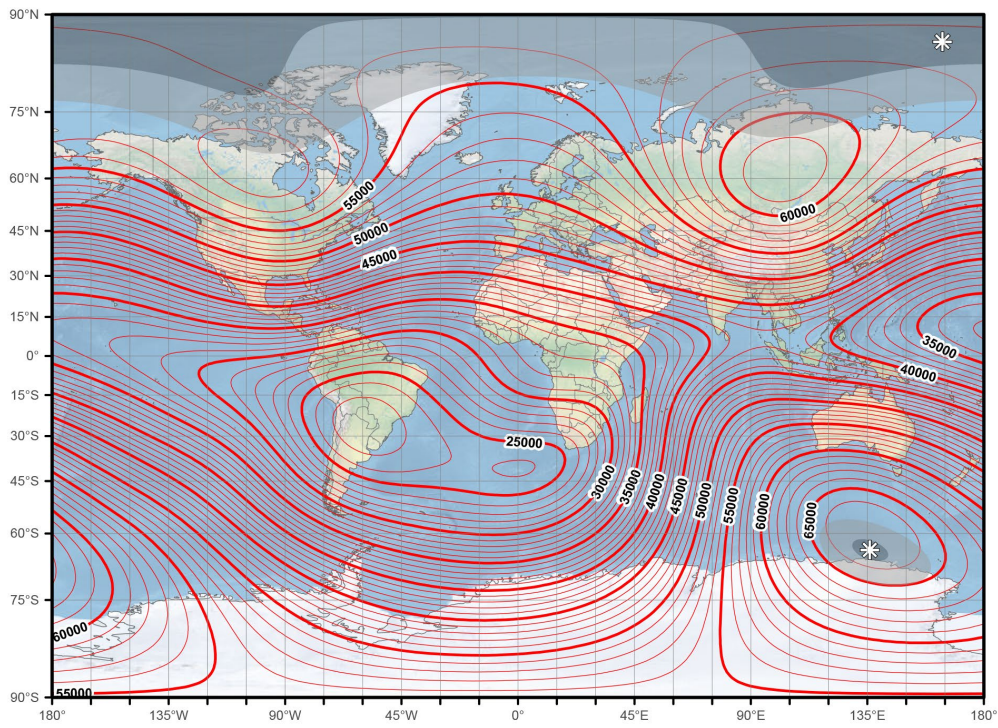
Main field east component (Y). Contour interval is 1000 nT, red contours positive (east); blue negative (west); green zero line. Miller projection.



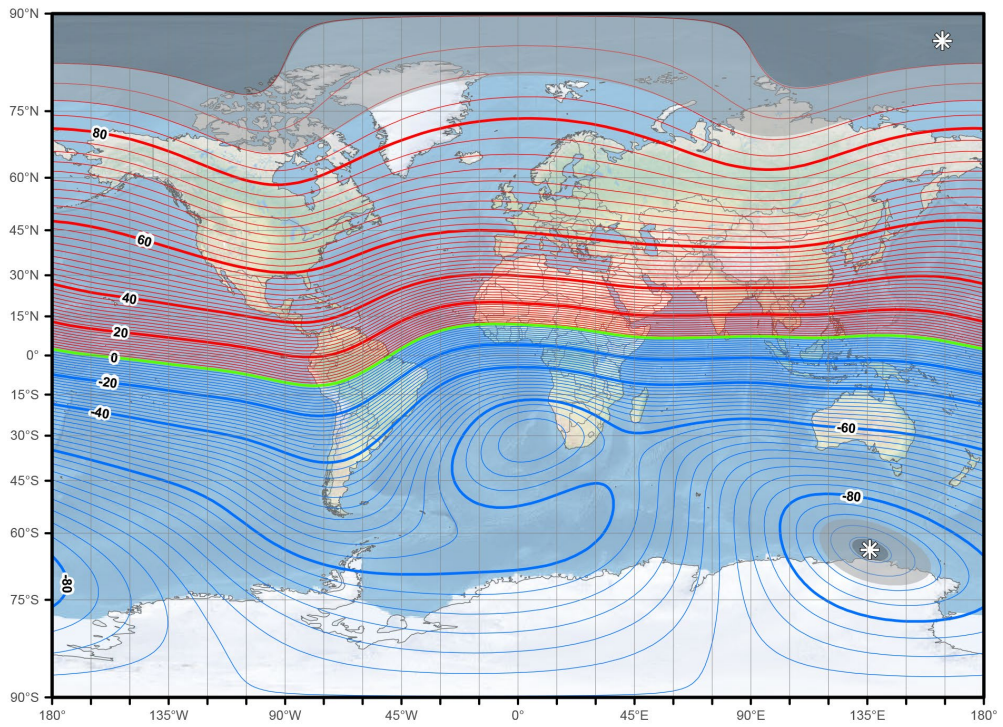
Main field down component (Z). Contour interval is 1000 nT, red contours positive (down); blue negative (up); green zero line. Miller projection.



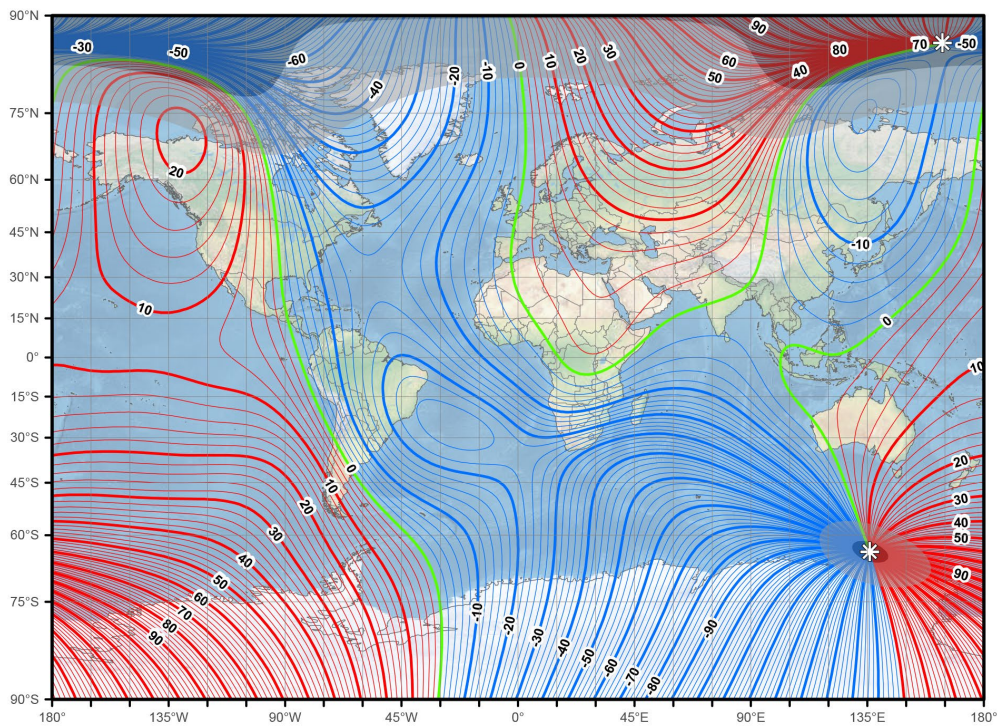
Main field horizontal intensity (H). Contour interval is 1000 nT. Miller projection.



Main field total intensity (F). Contour interval is 1000 nT. Miller projection.

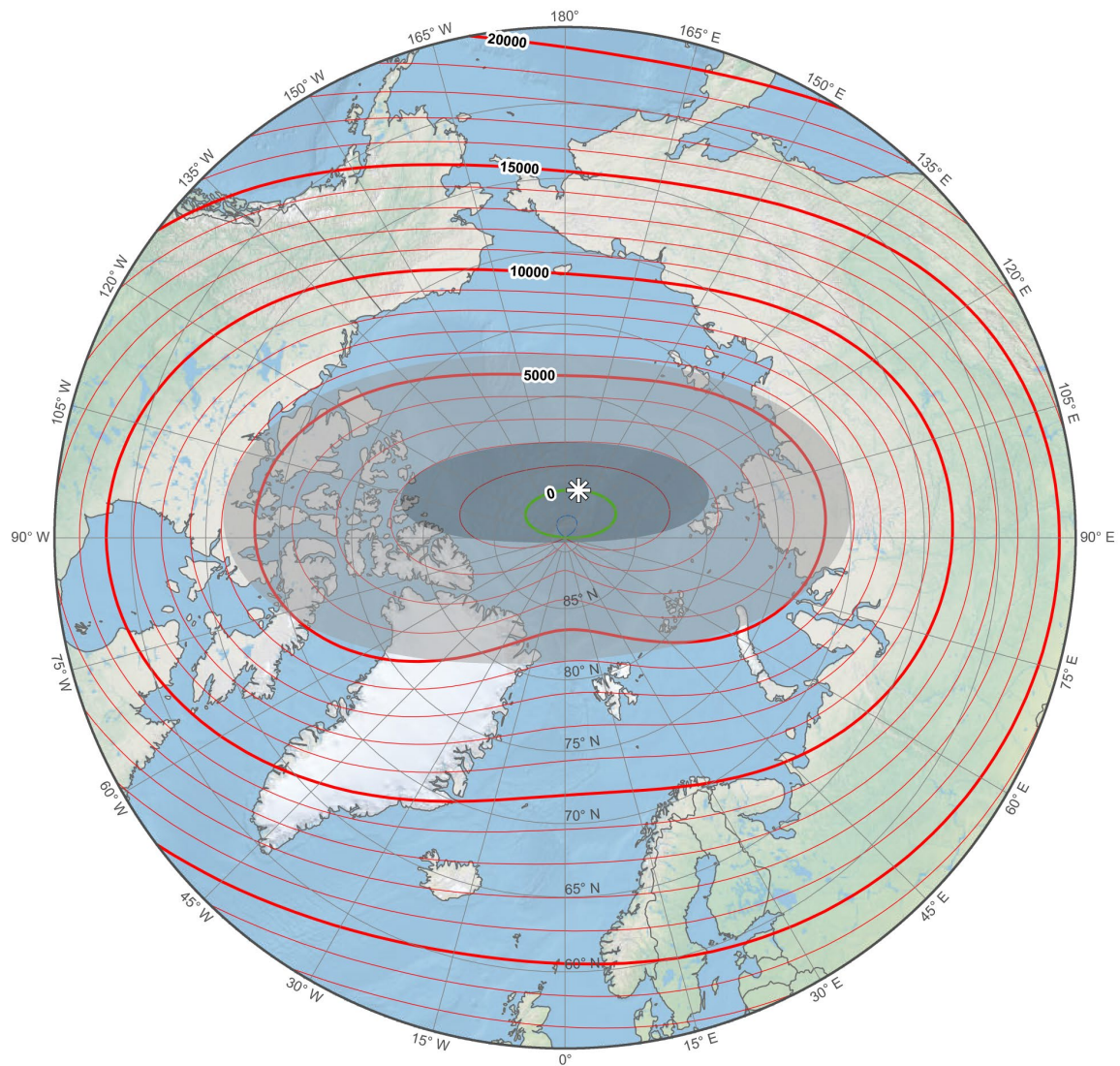


Main field inclination (I). Contour interval is 2 degrees, red contours positive (down); blue negative (up); green zero line. Miller projection.

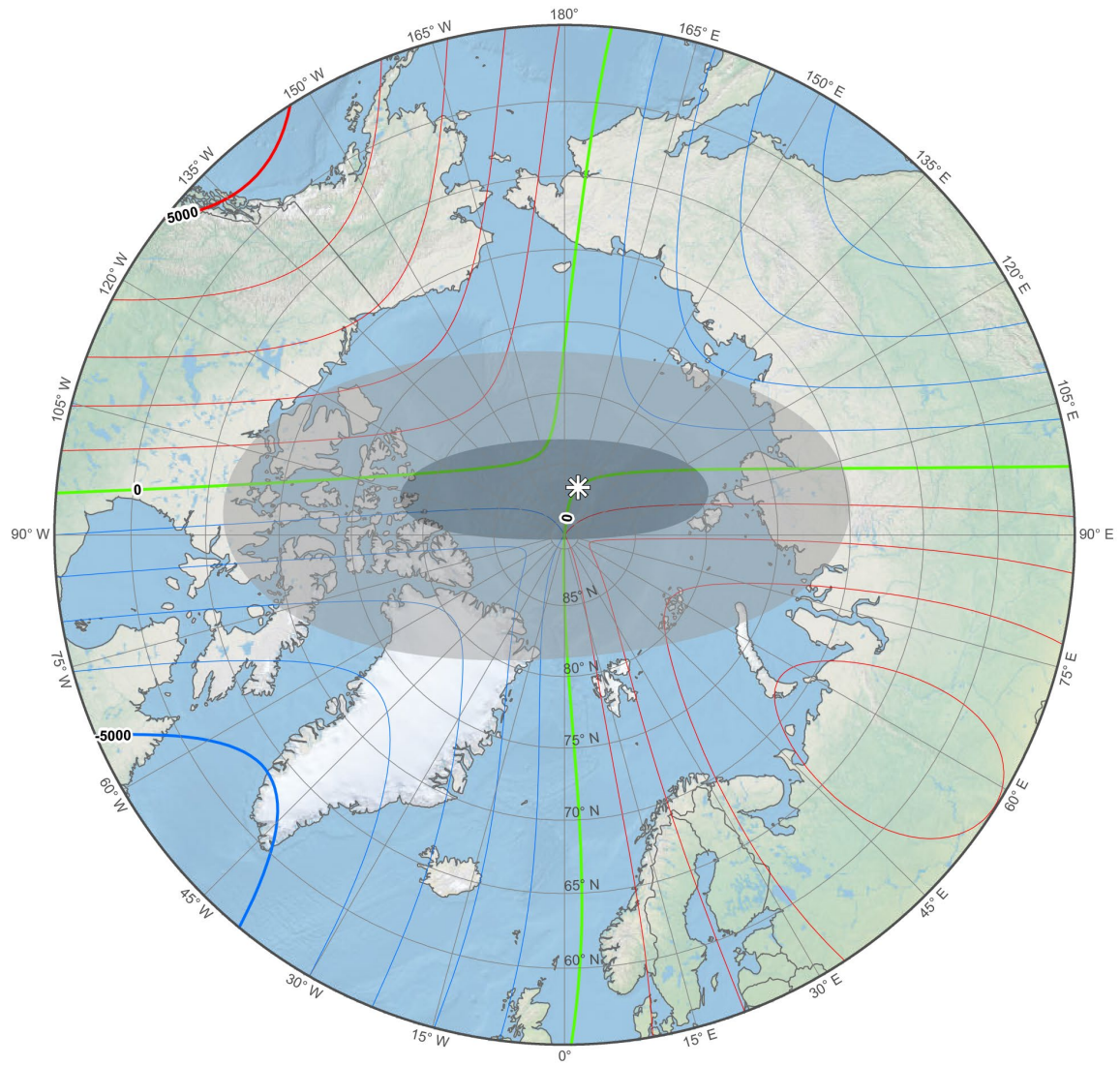


Main field declination (D). Contour interval is 2 degrees, red contours positive (east); blue negative (west); green zero (agonic) line. Miller projection.

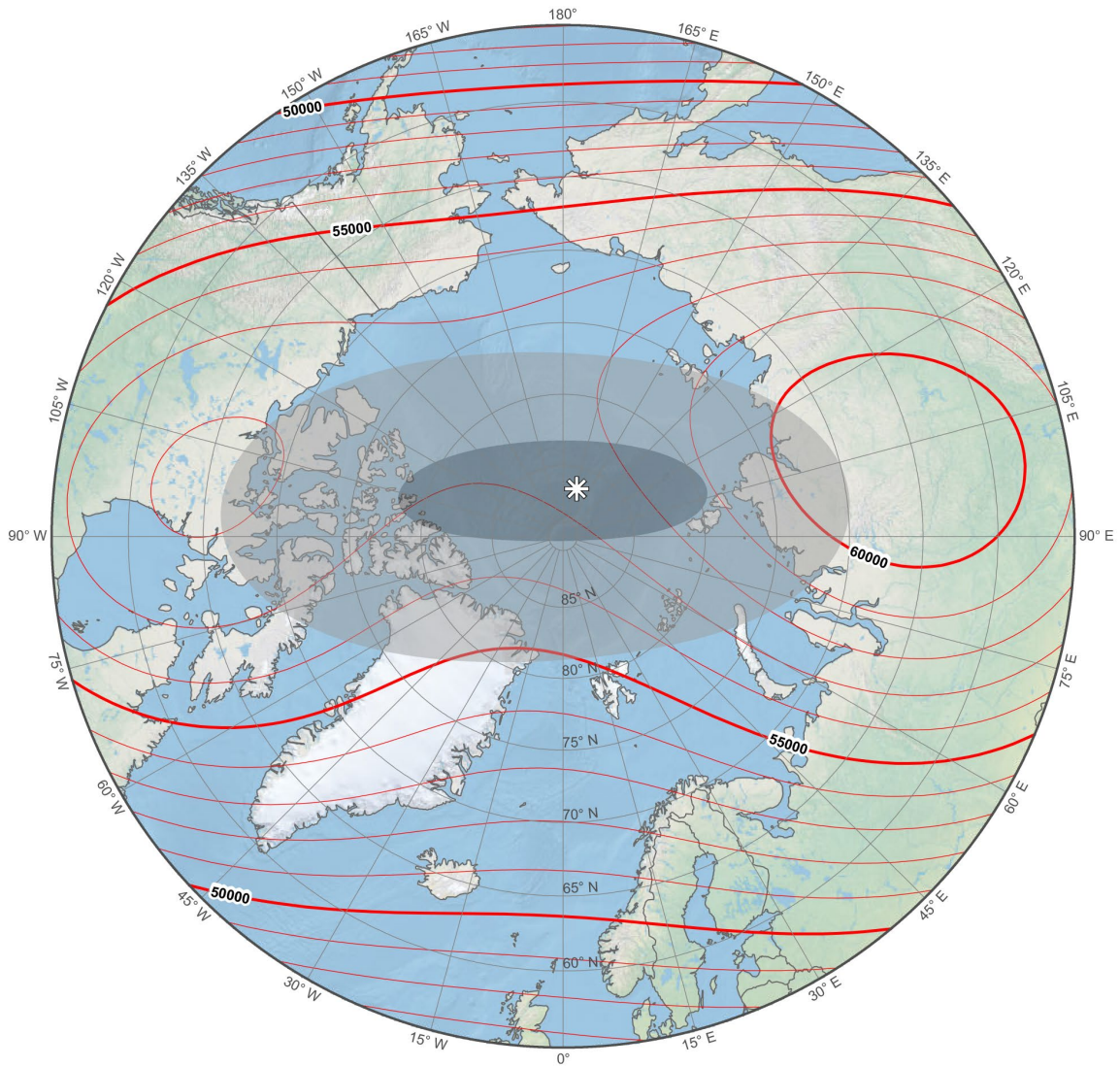
MAIN FIELD MAPS: NORTH POLAR STEREOGRAPHIC PROJECTION



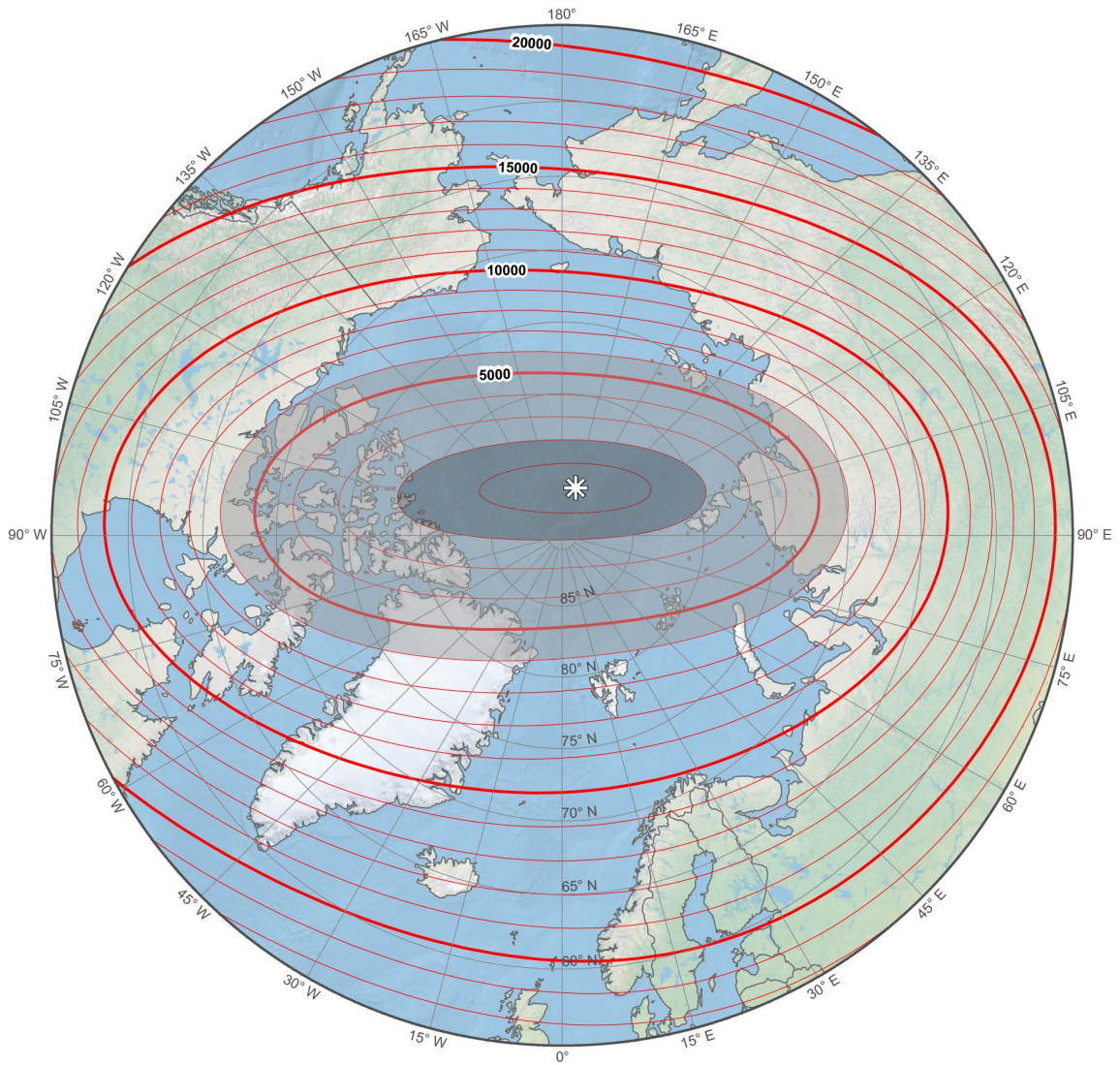
Main field north component (X). Contour interval is 1000 nT. North polar region. Polar Stereographic Projection.



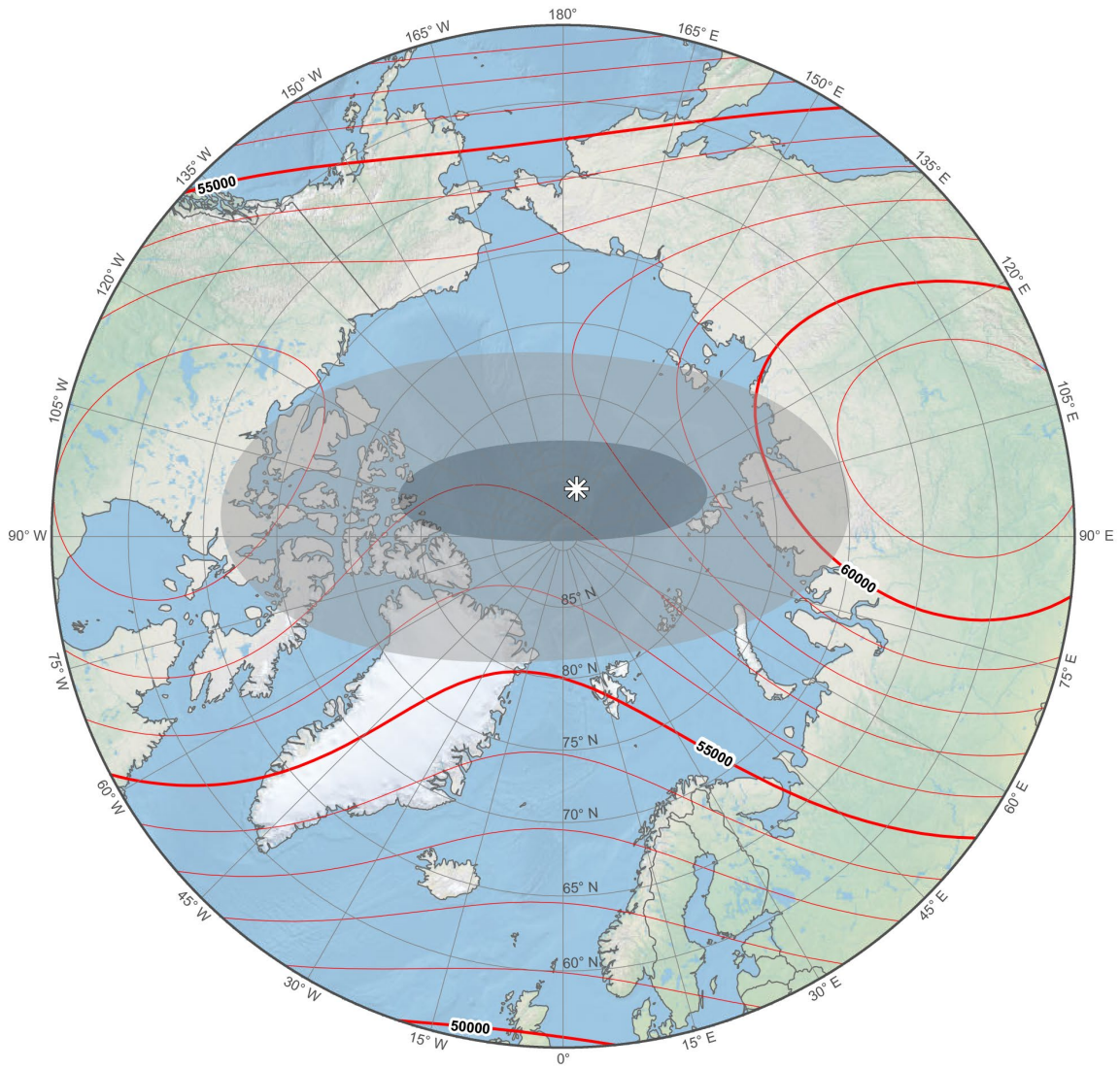
Main field east component (Y). Contour interval is 1000 nT, red contours positive (east); blue negative (west); green zero line. North polar region. Polar Stereographic Projection.



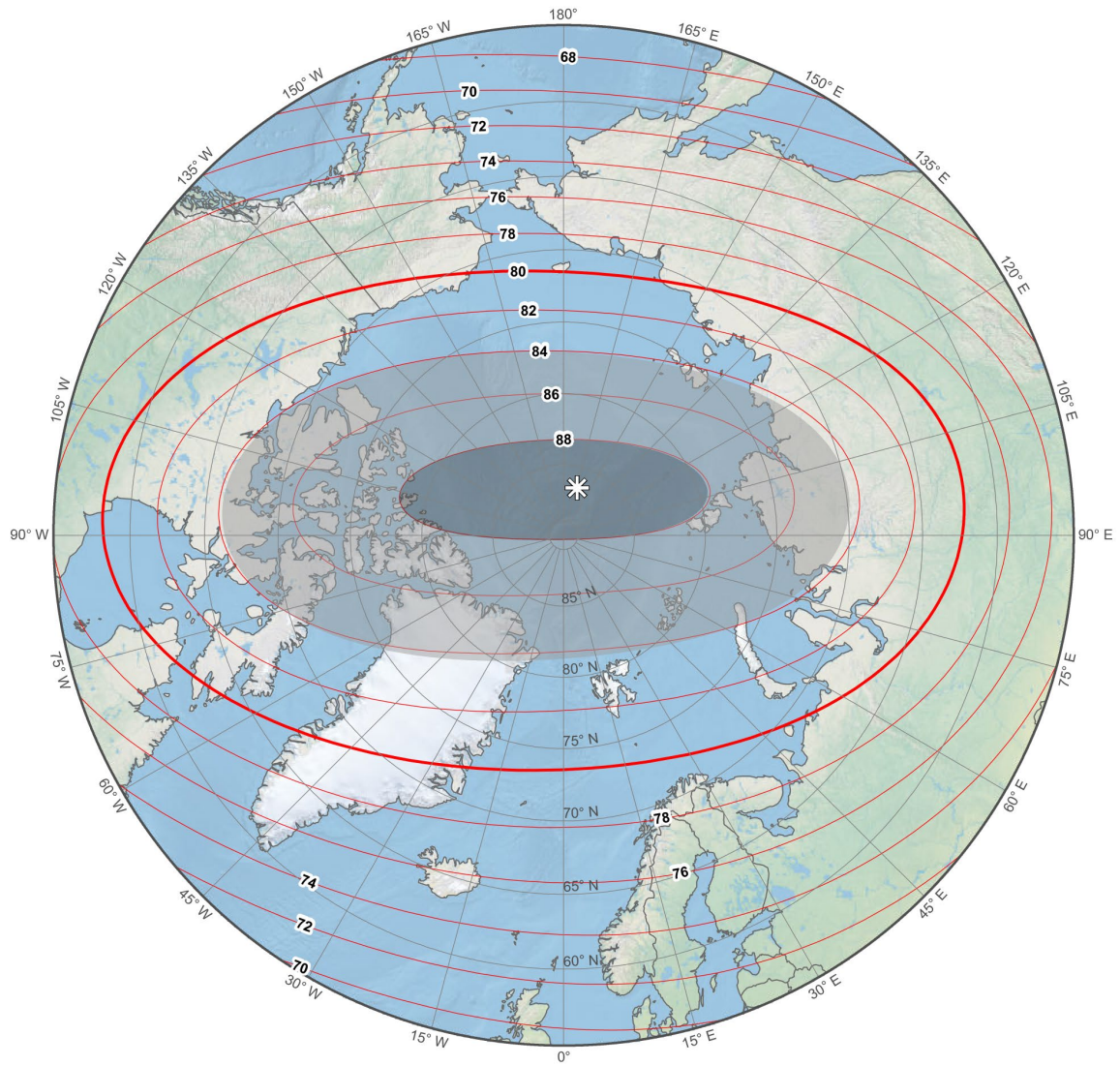
Main field down component (Z). Contour interval is 1000 nT. North polar region. Polar Stereographic Projection.



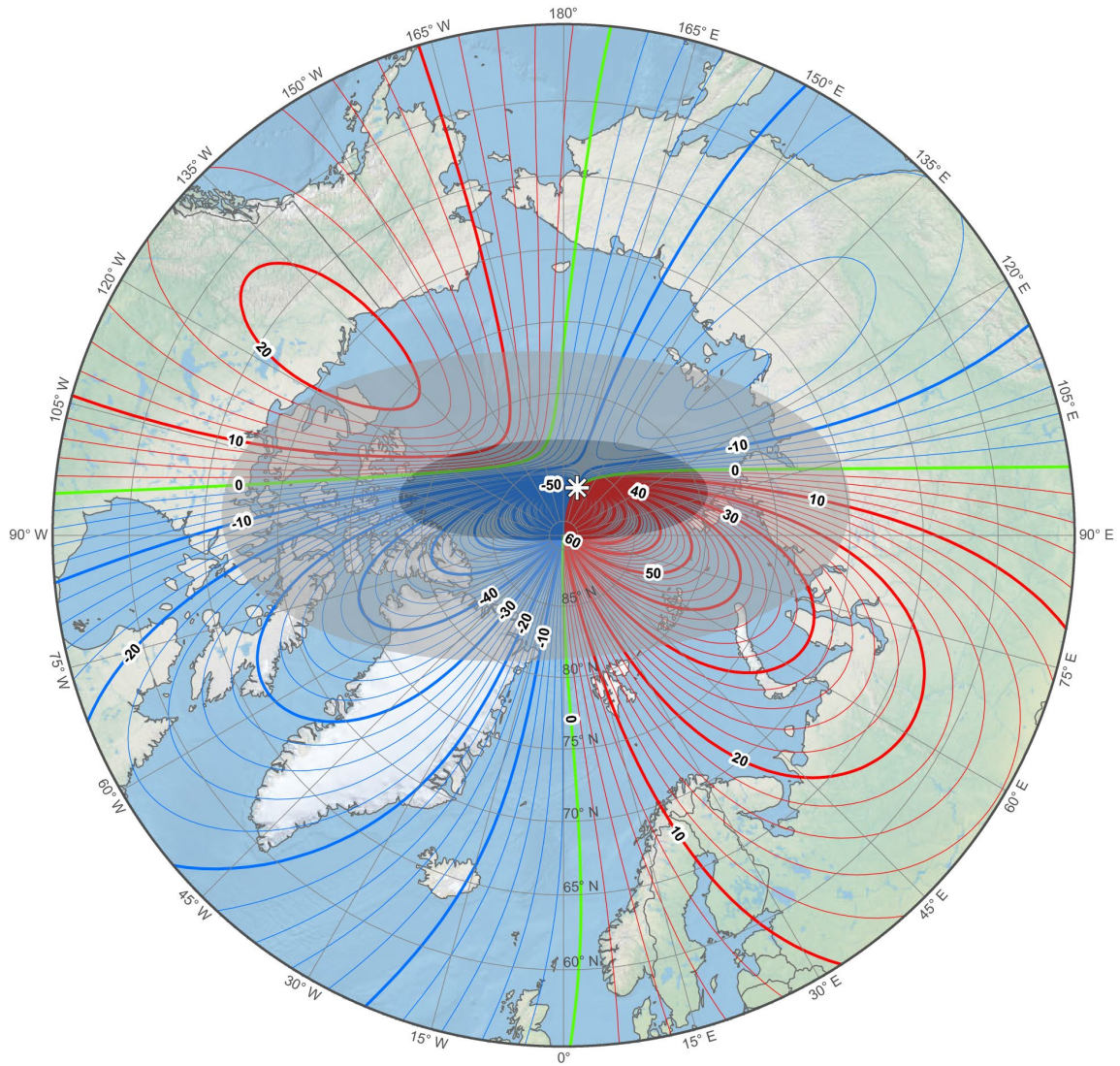
Main field horizontal intensity (H). Contour interval is 1000 nT. North polar region. Polar Stereographic Projection.



Main field total intensity (F). Contour interval is 1000 nT. North polar region. Polar Stereographic Projection.

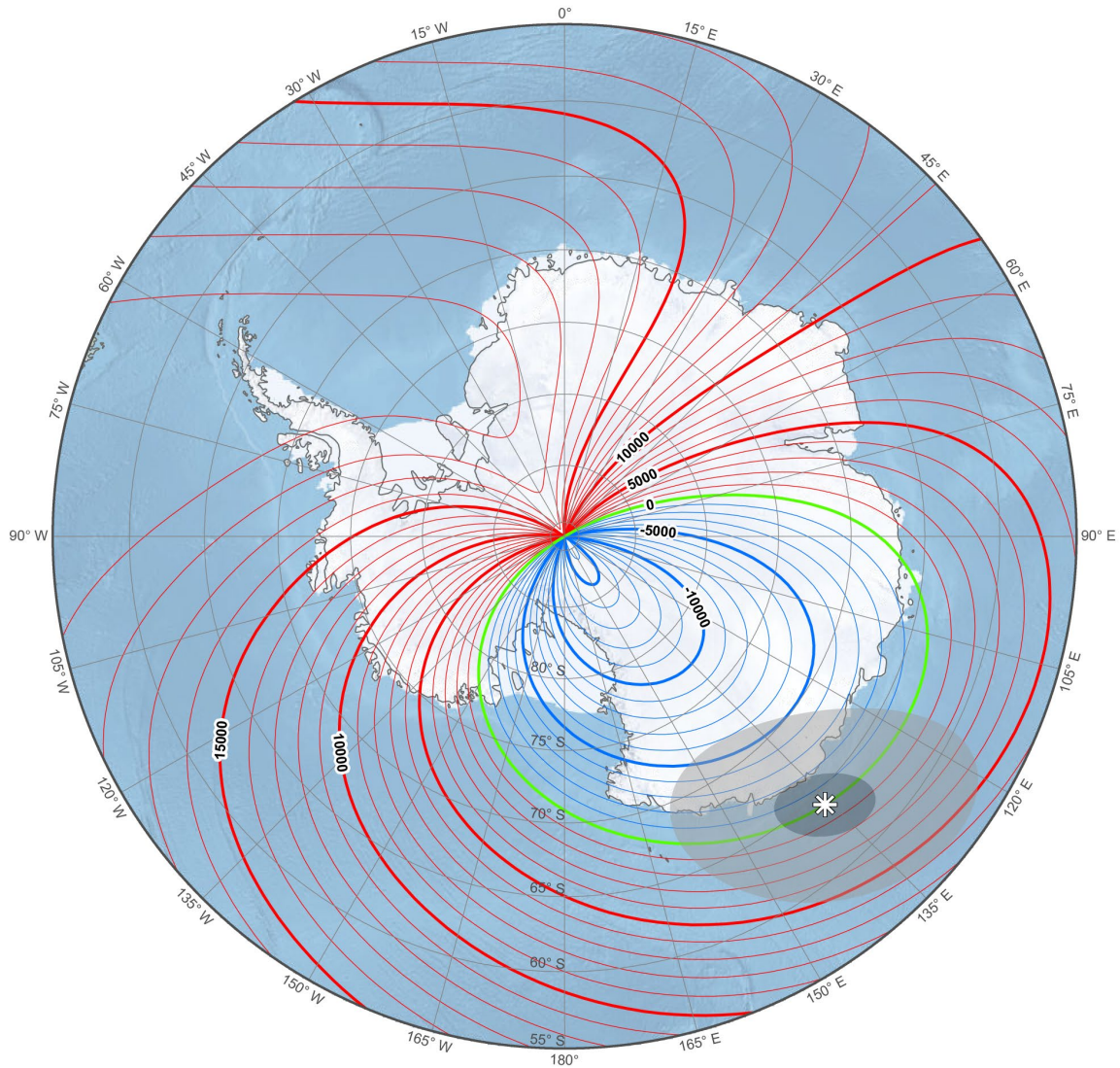


Main field inclination (I). Contour interval is 2 degrees. North polar region. Polar Stereographic Projection.

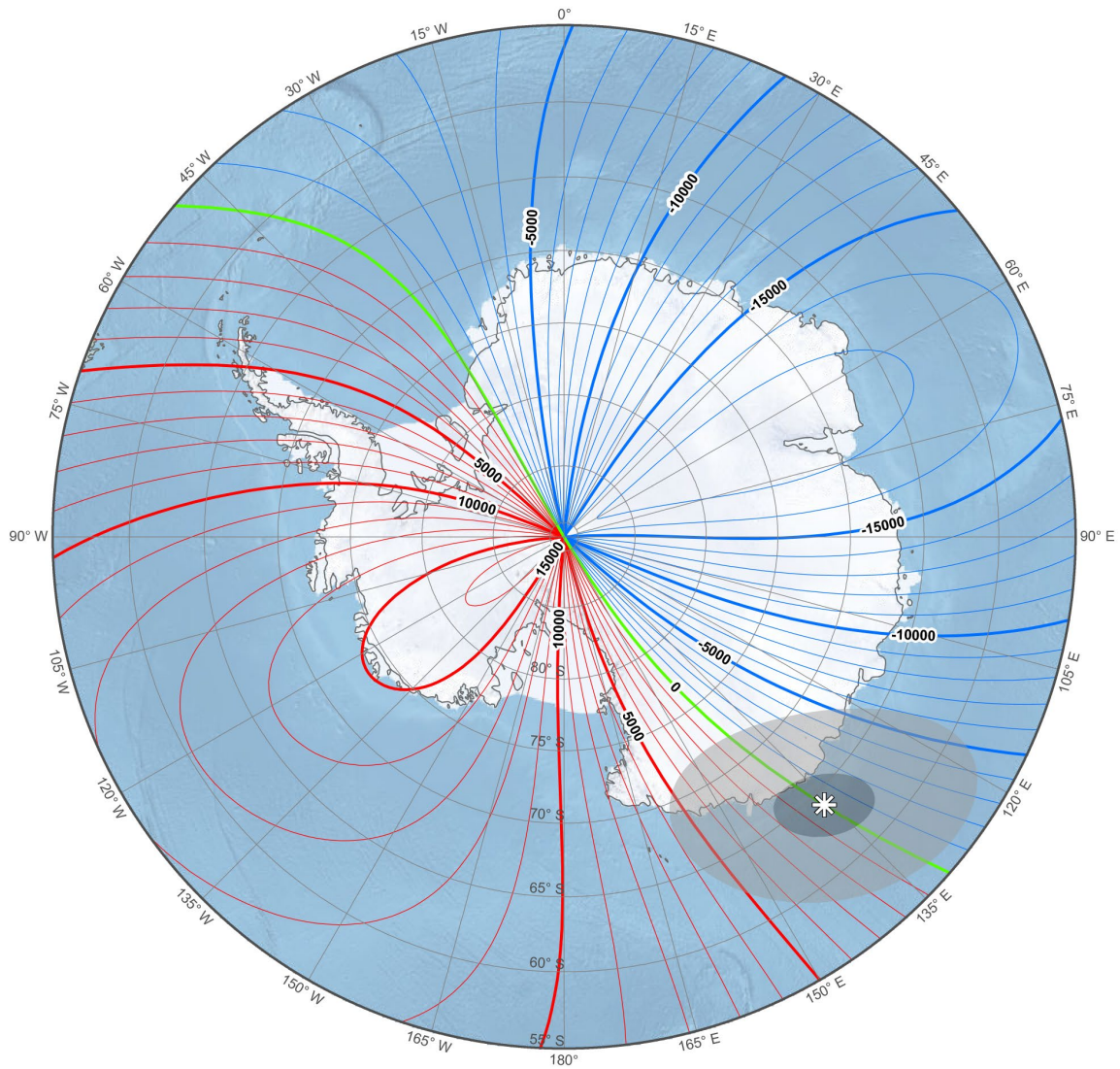


Main field declination (D). Contour interval is 2 degrees, red contours positive (east); blue negative (west); green zero (agonic) line. North polar region. Polar Stereographic Projection.

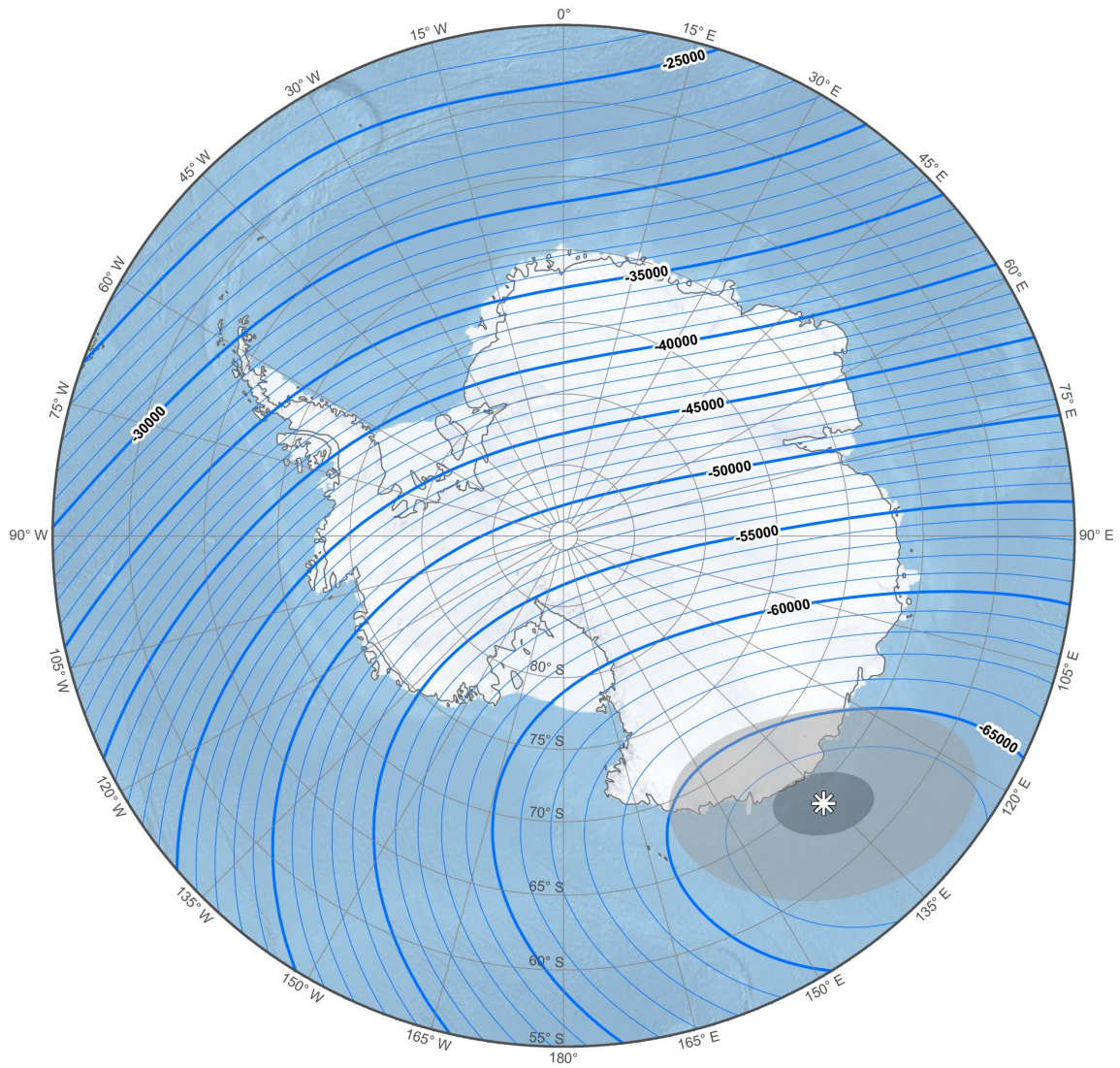
MAIN FIELD MAPS: SOUTH POLAR STEREOGRAPHIC PROJECTION



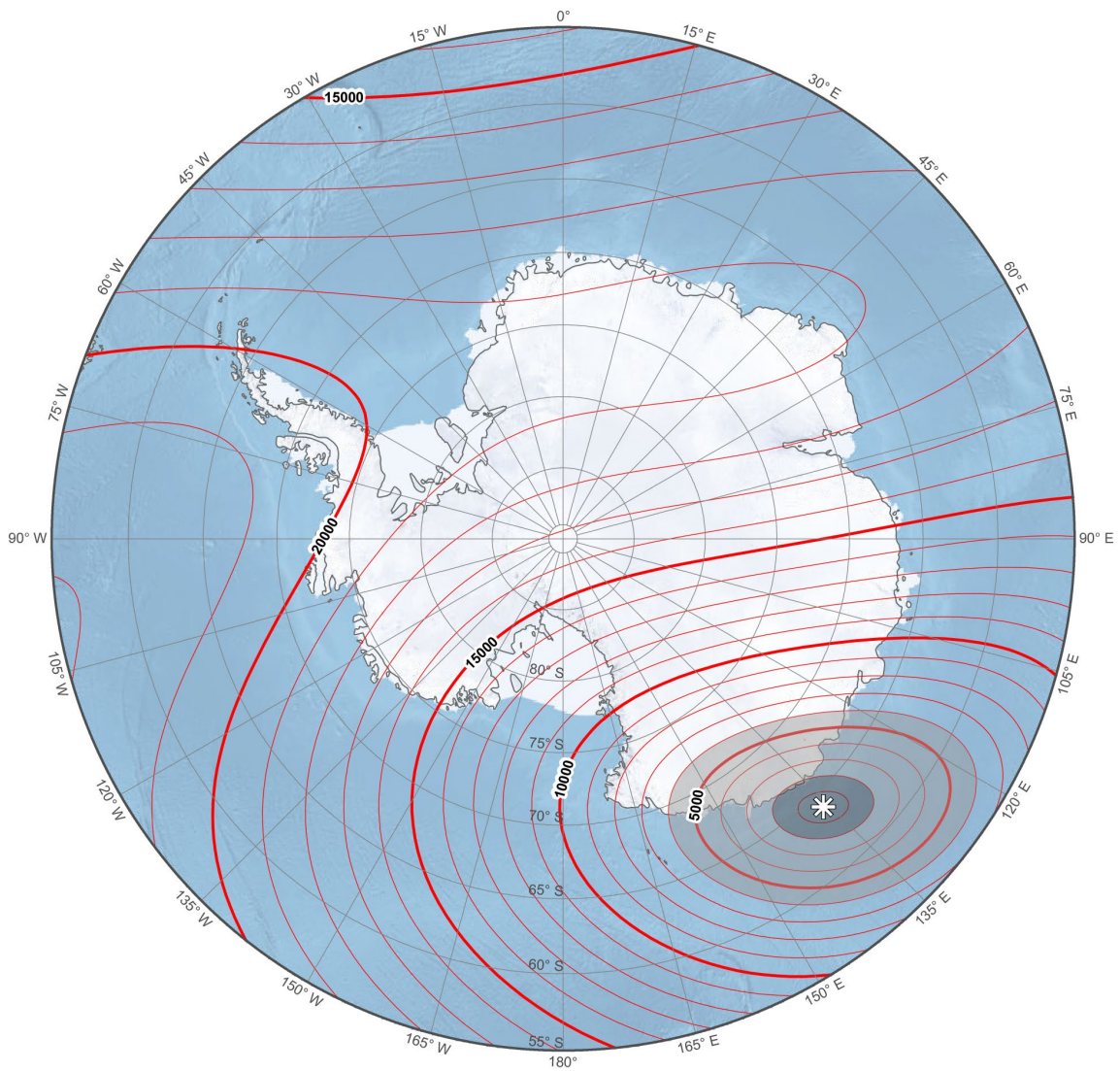
Main field north component (X). Contour interval is 1000 nT, red contours positive (north); blue negative (south); green zero line. South polar region. Polar Stereographic Projection.



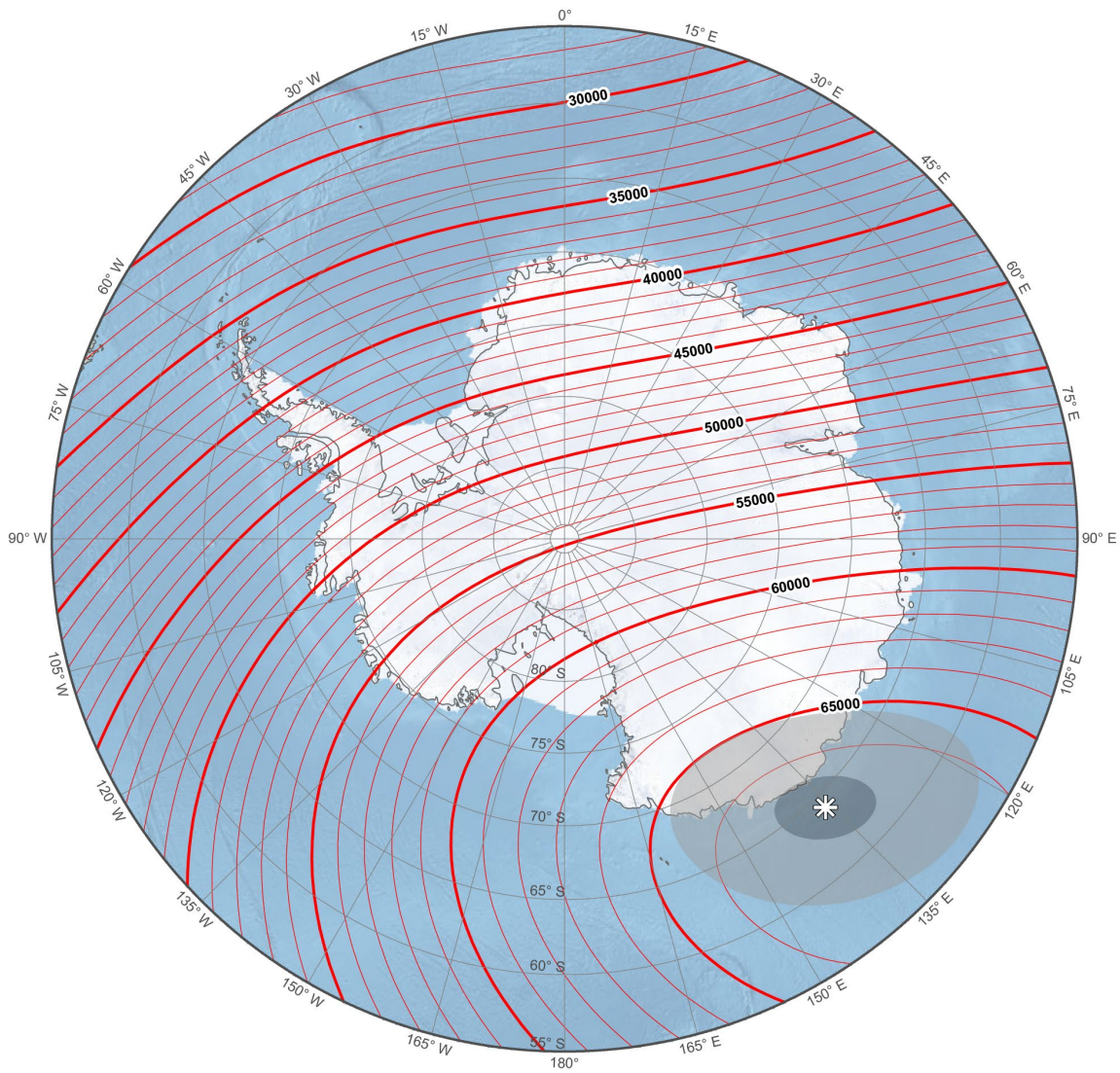
Main field east component (Y). Contour interval is 1000 nT, red contours positive (east); blue negative (west); green zero line. South polar region. Polar Stereographic Projection.



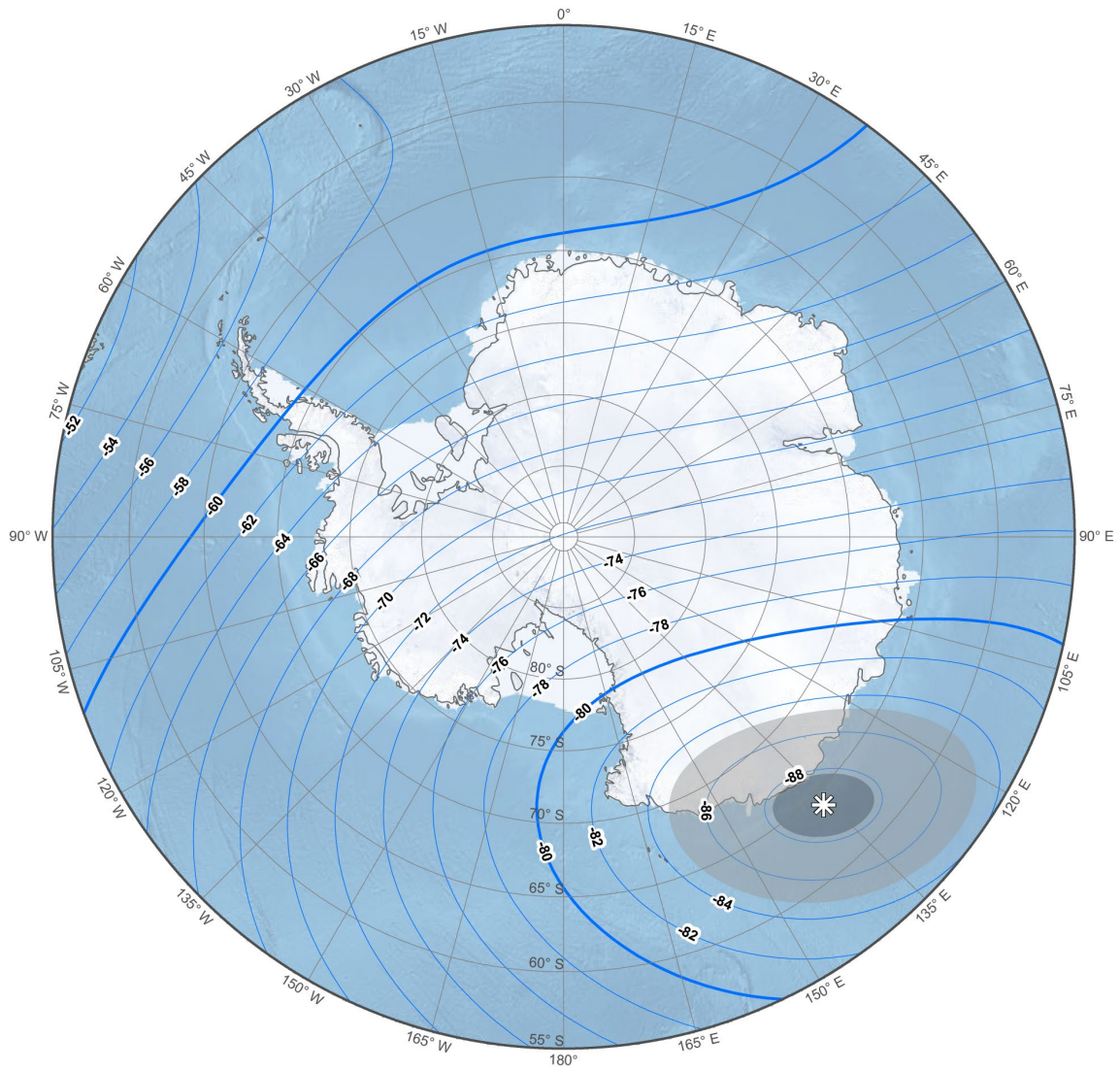
Main field down component (Z). Contour interval is 1000 nT. South polar region. Polar Stereographic Projection.



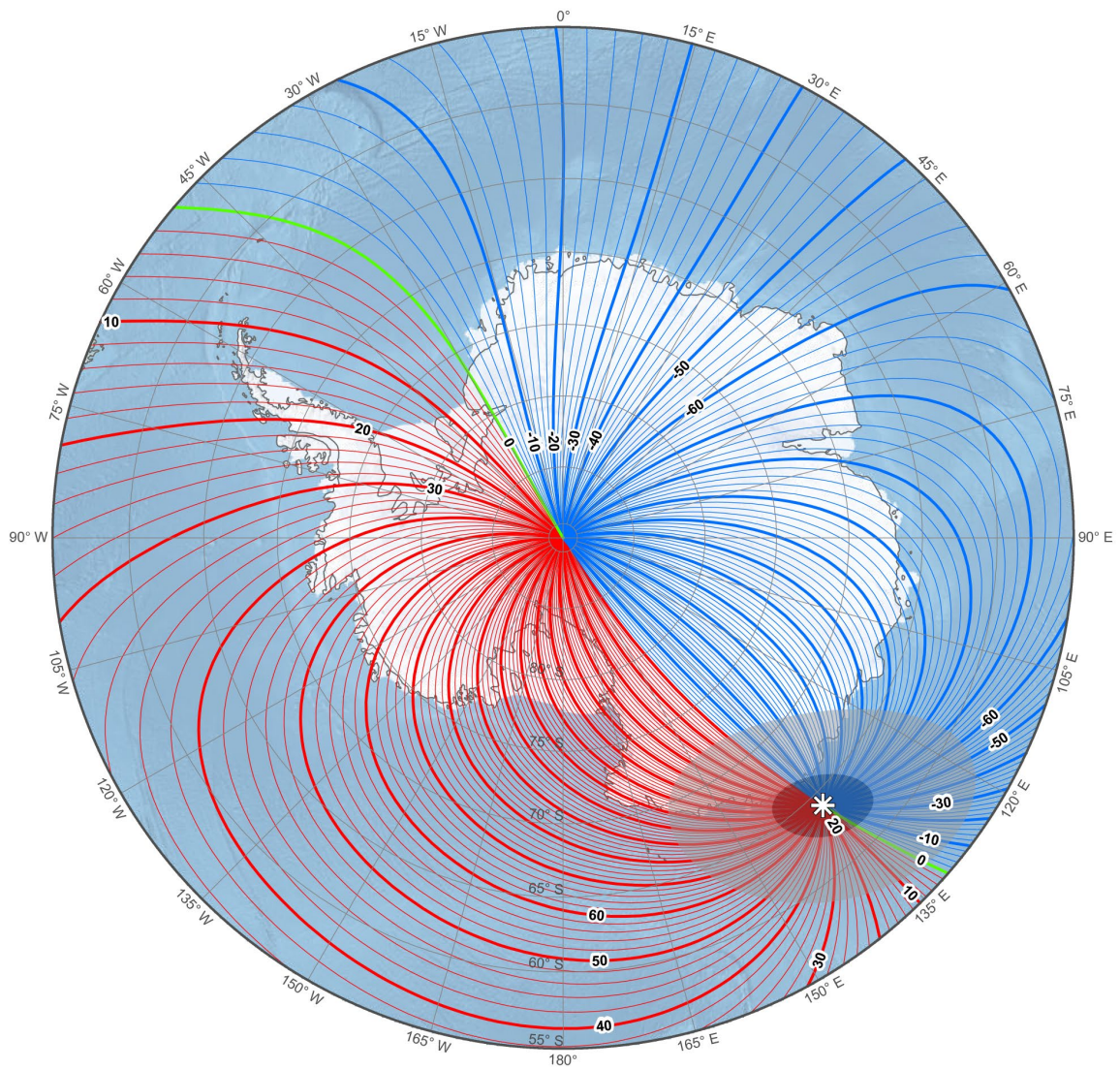
Main field horizontal intensity (H). Contour interval is 1000 nT. South polar region. Polar Stereographic Projection.



Main field total intensity (F). Contour interval is 1000 nT. South polar region. Polar Stereographic Projection.

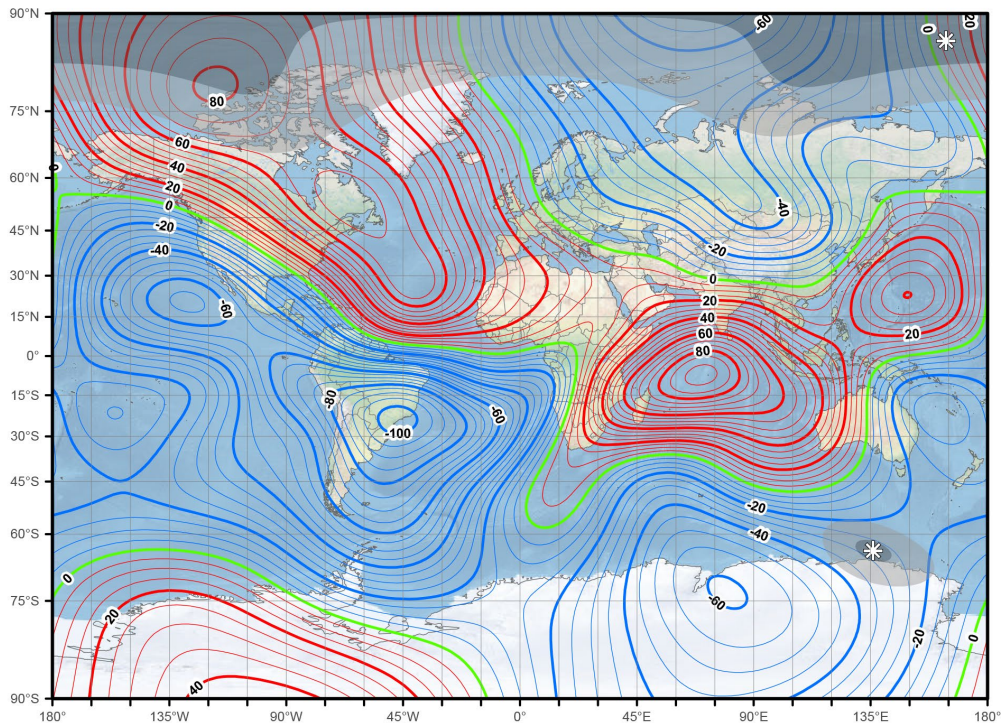


Main field inclination (I). Contour interval is 2 degrees. South polar region. Polar Stereographic Projection.

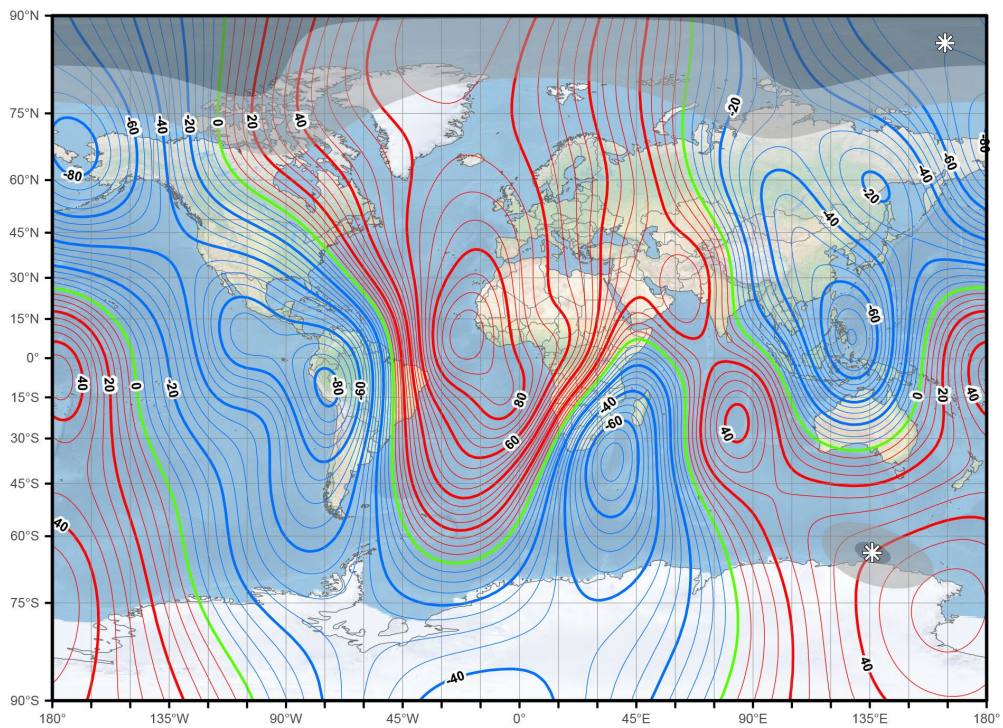


Main field declination (D). Contour interval is 2 degrees, red contours positive (east); blue negative (west); green zero (agonic) line. South polar region. Polar Stereographic Projection.

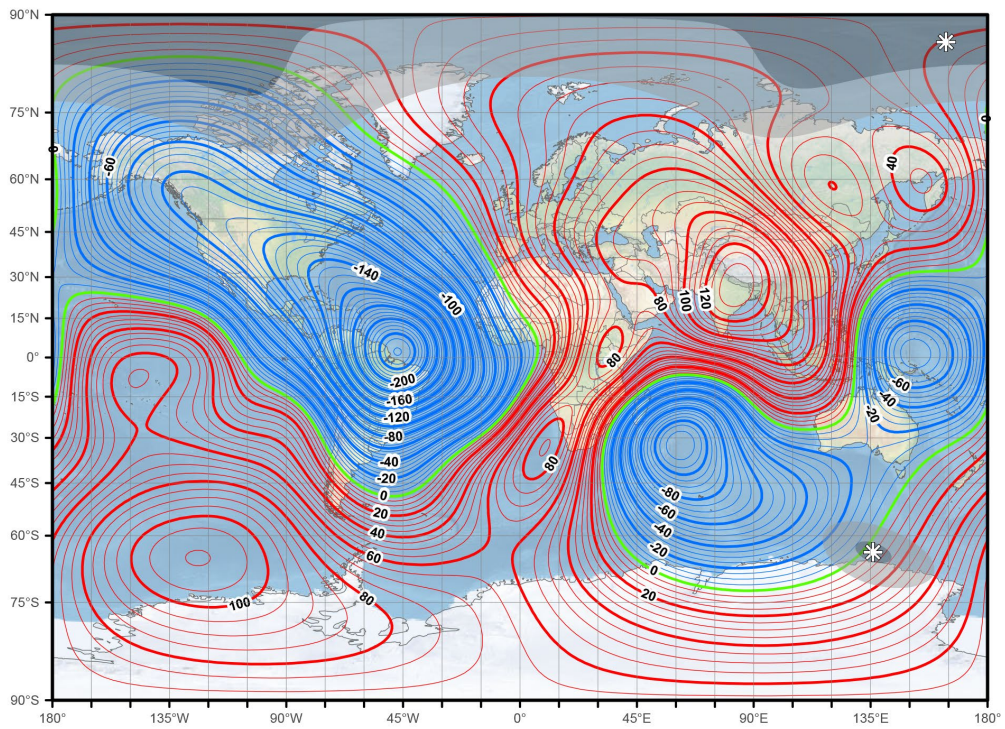
SECULAR VARIATION MAPS: MILLER PROJECTION



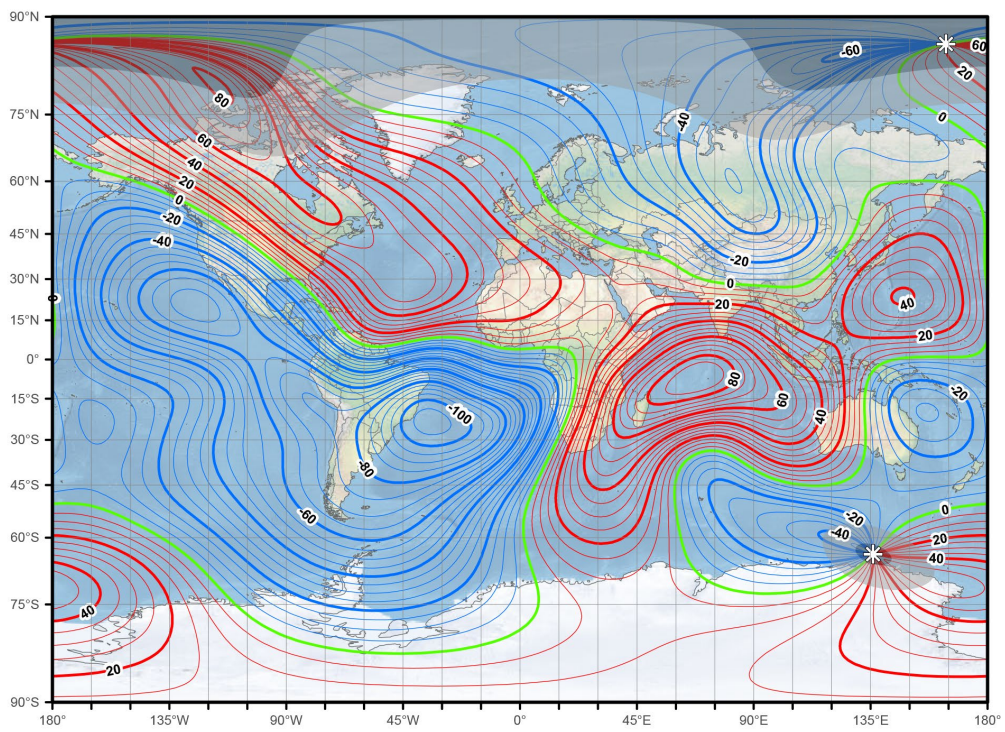
Annual change north component (X). Contour interval is 5 nT / year, red contours positive (north) change; blue negative (south) change; green zero change. Miller Projection.



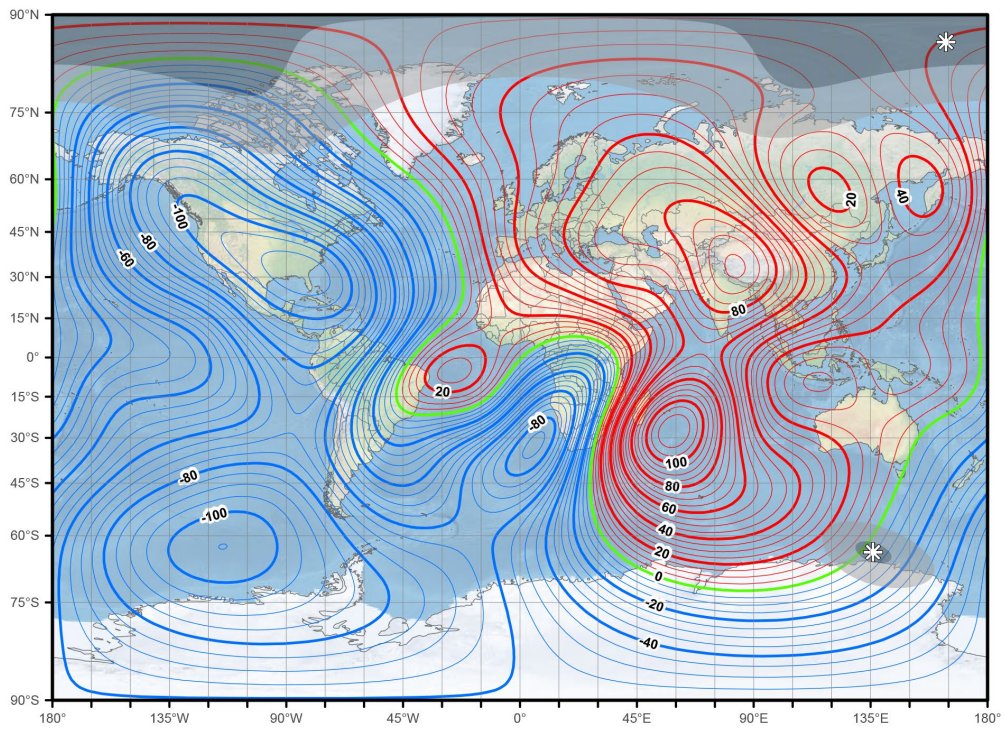
Annual change east component (Y). Contour interval is 5 nT / year, red contours positive (east) change; blue negative (west) change; green zero change. Miller Projection.



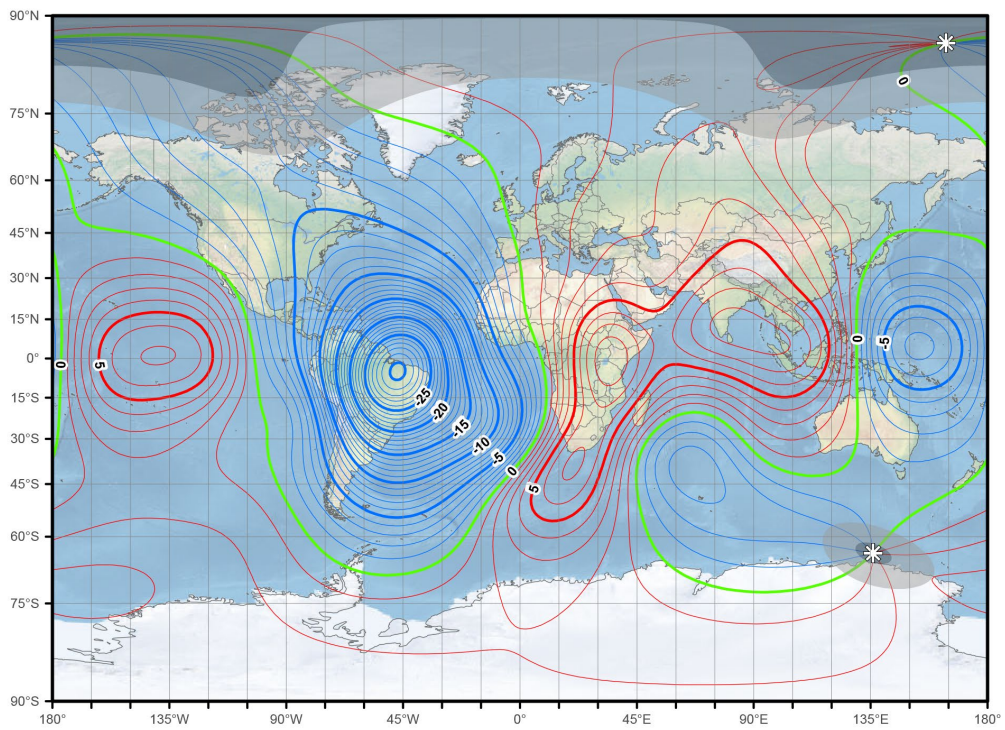
Annual change down component (Z). Contour interval is 5 nT / year, red contours positive (down) change; blue negative (up) change; green zero change. Miller Projection.



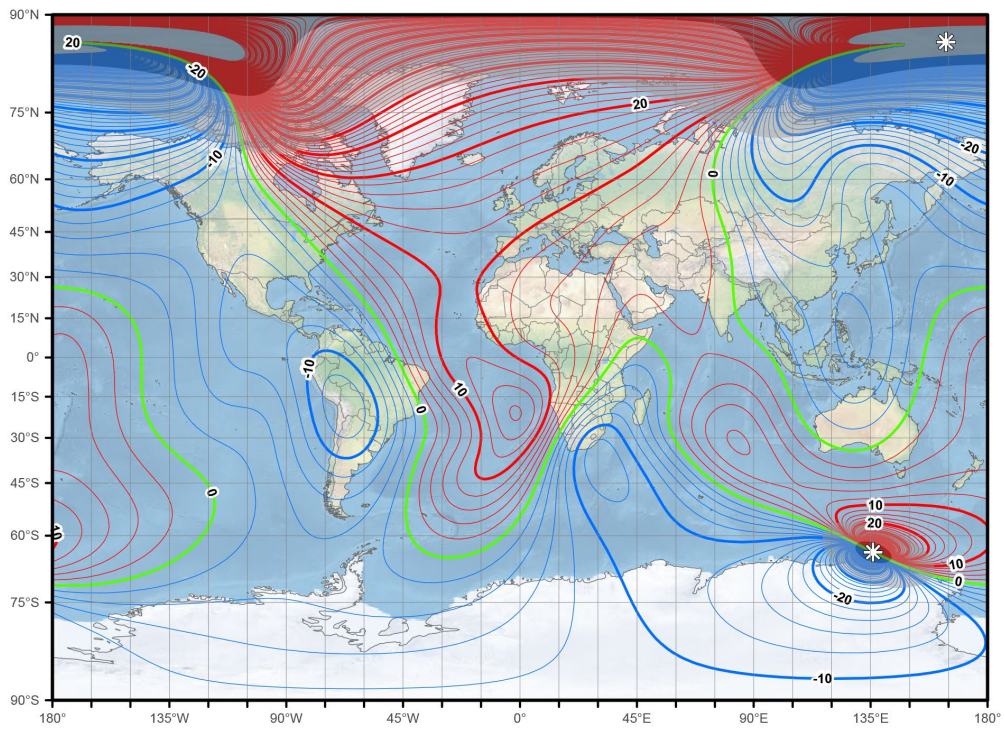
Annual change horizontal intensity (H). Contour interval is 5 nT / year, red contours positive change; blue negative change; green zero change. Miller Projection.



Annual change total intensity (F). Contour interval is 5 nT / year, red contours positive change; blue negative change; green zero change. Miller Projection.

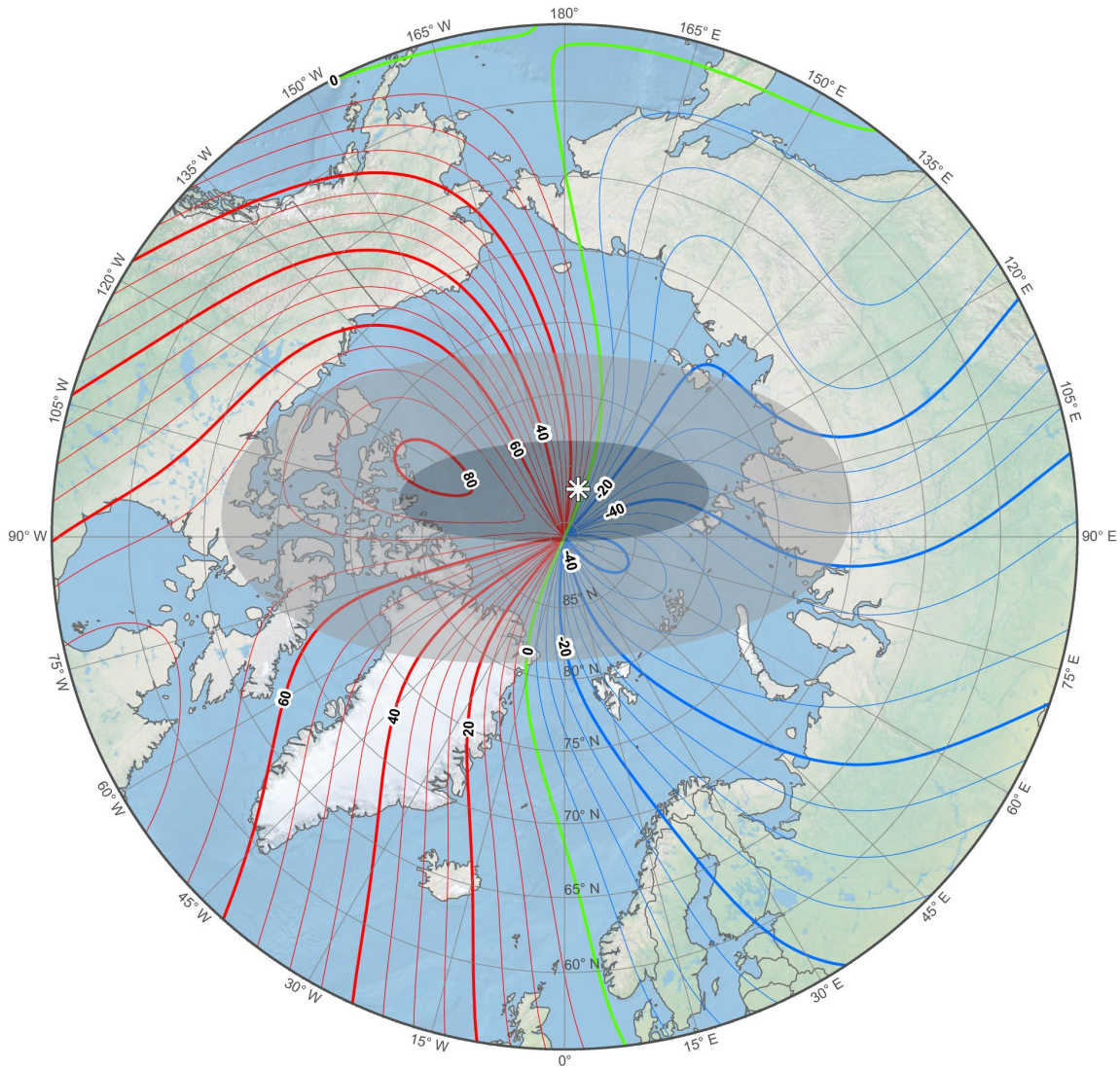


Annual change inclination (I). Contour interval is 1 arc-minute / year, red contours positive (downward) change; blue negative (upward) change; green zero change. Miller Projection.

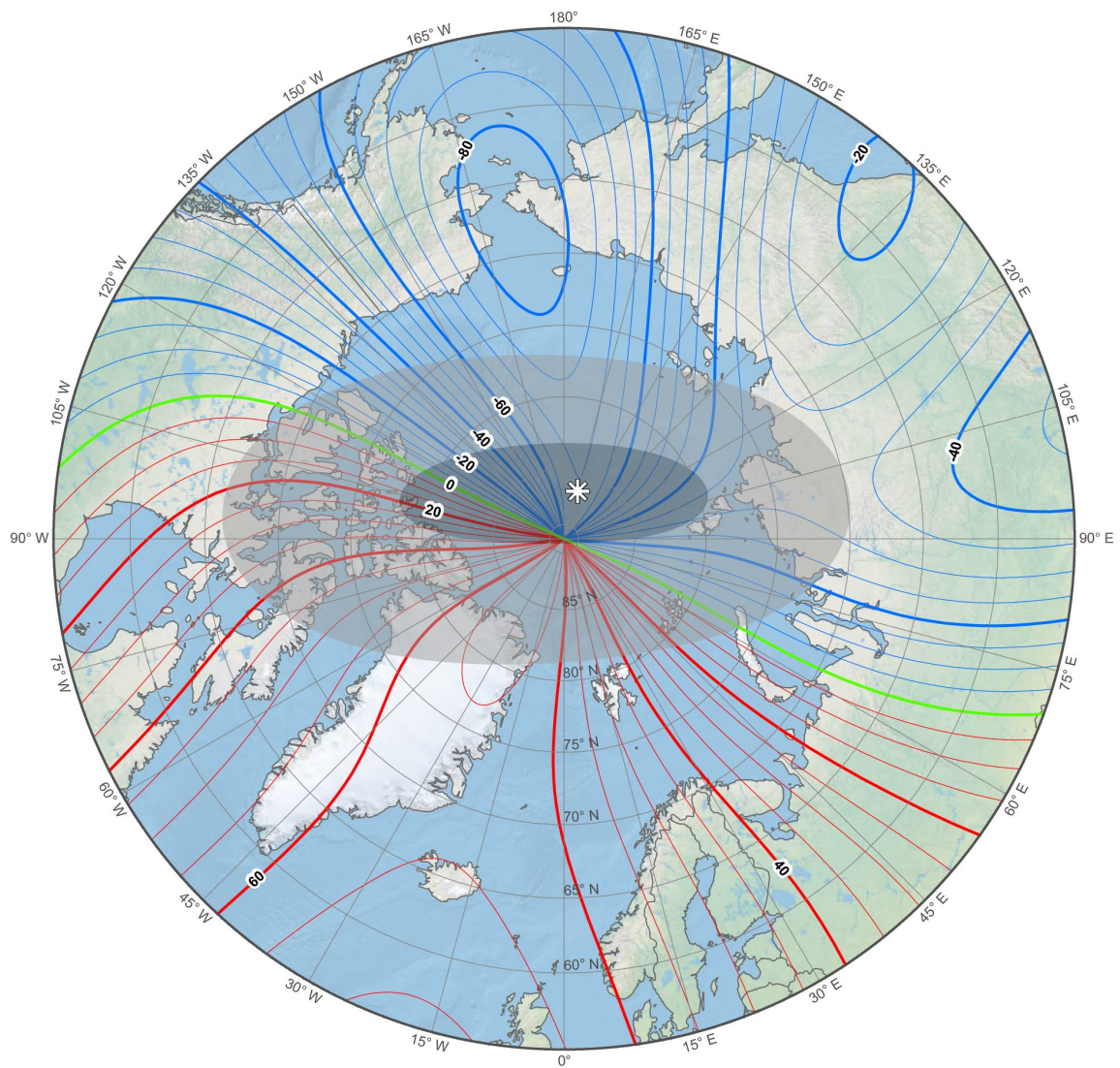


Annual change declination (D). Contour interval is 2 arc-minutes / year, red contours positive (clockwise) change; blue negative (counter-clockwise) change; green zero change. Miller Projection.

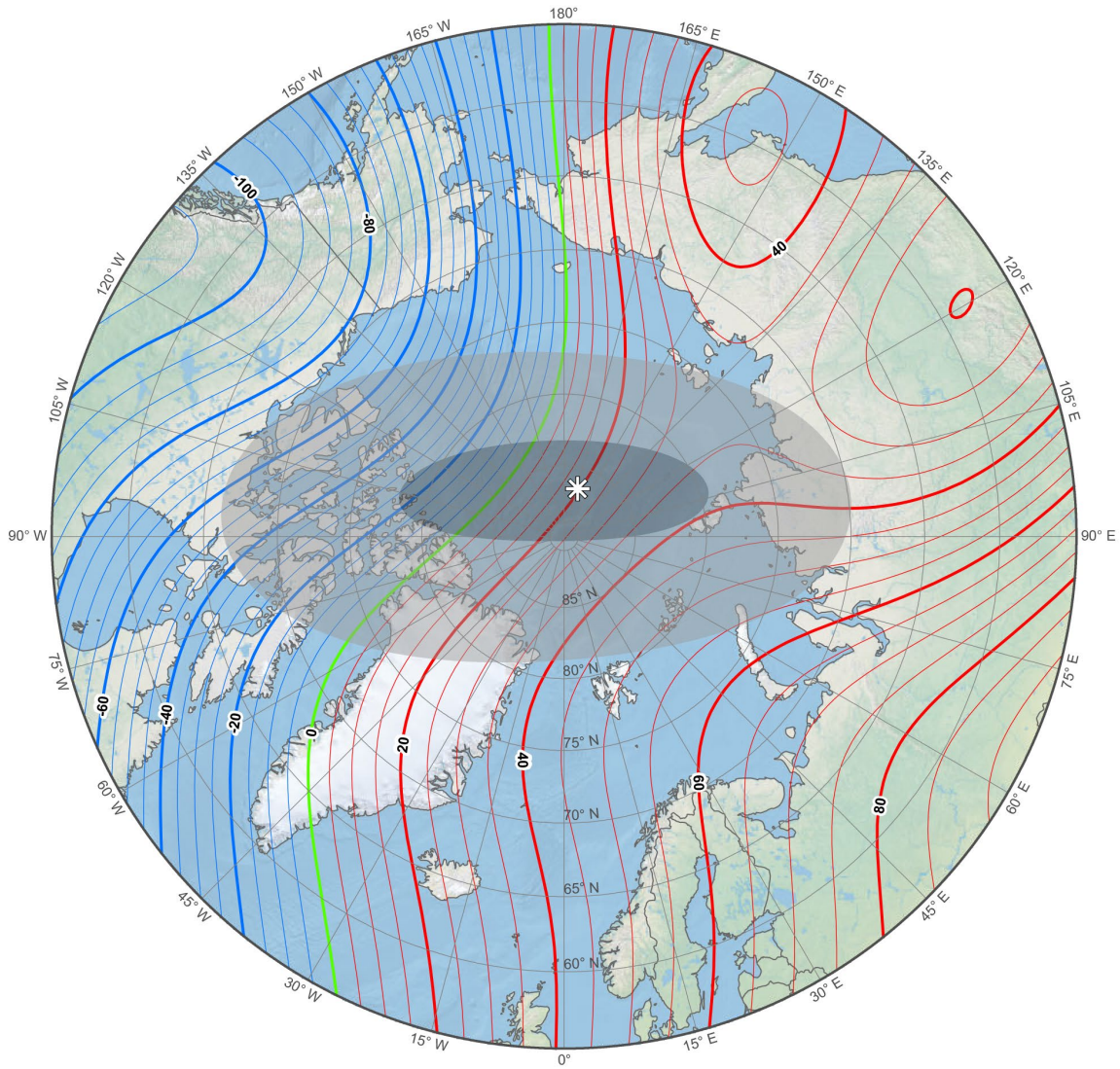
SECULAR VARIATION MAPS: NORTH POLAR STEREOGRAPHIC PROJECTION



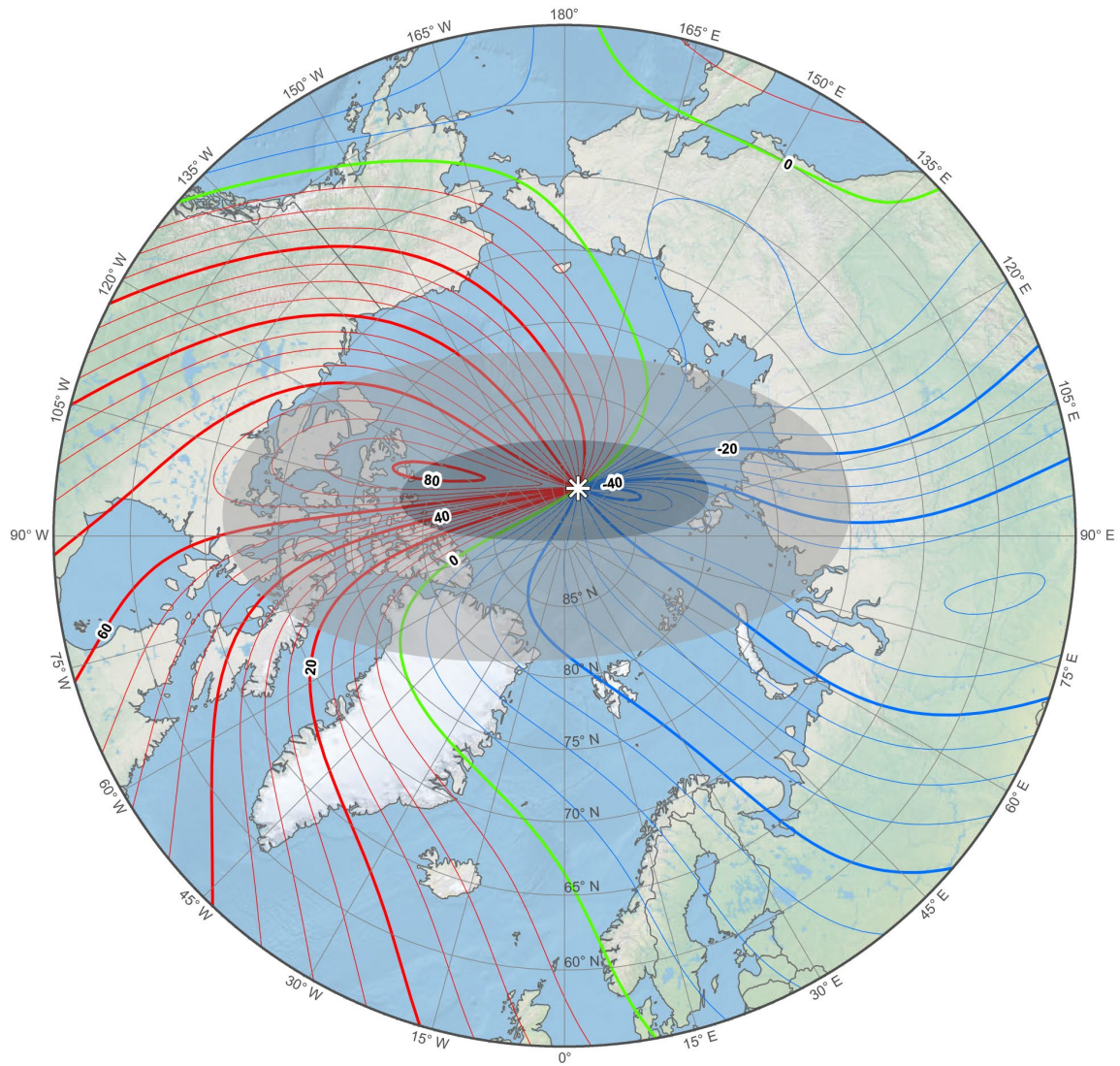
Annual change north component (X). Contour interval is 5 nT / year, red contours positive (north) change; blue negative (south) change; green zero change. North Polar Region. Polar Stereographic Projection.



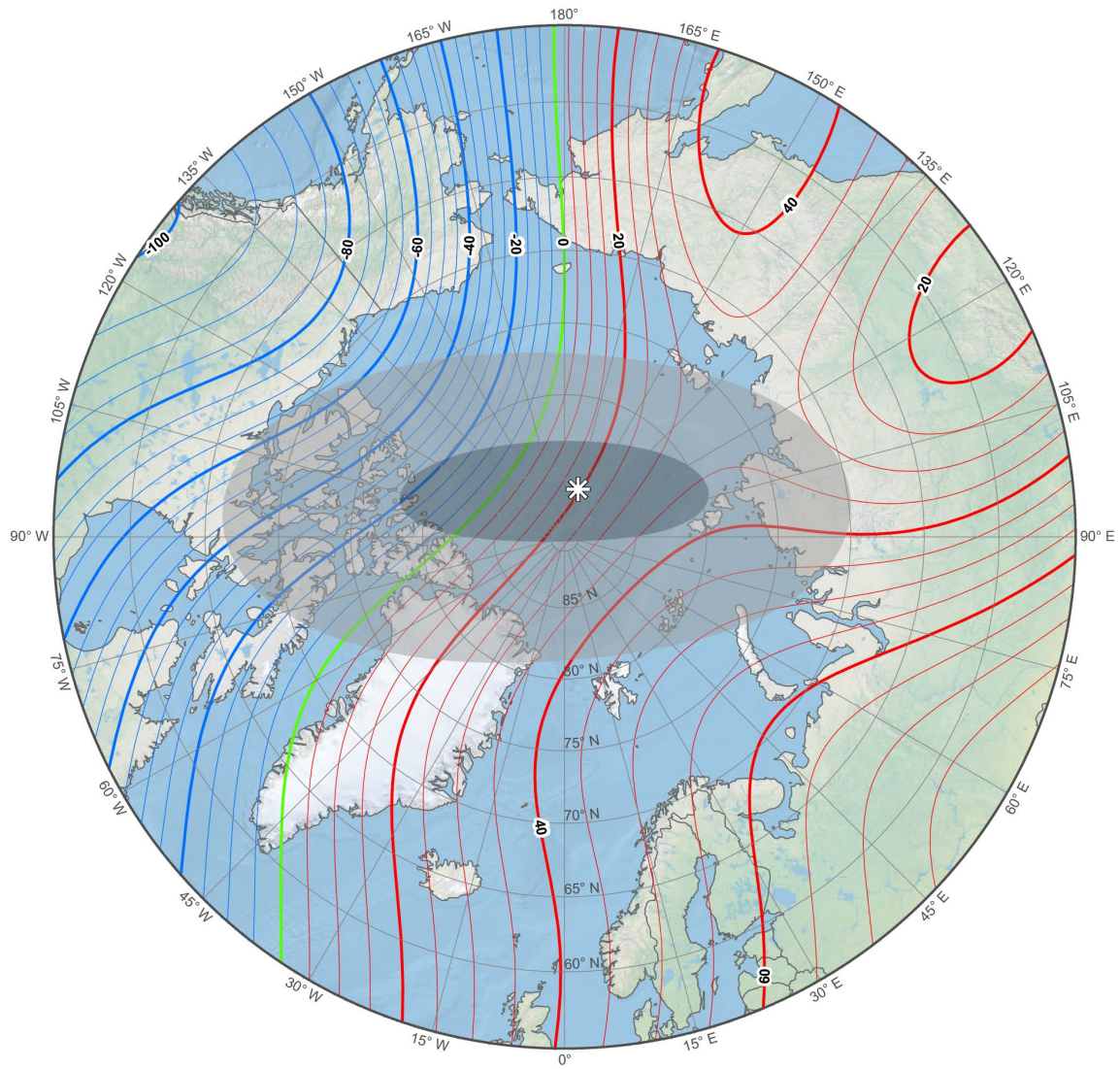
Annual change east component (Y). Contour interval is 5 nT / year, red contours positive (east) change; blue negative (west) change; green zero change. North Polar Region. Polar Stereographic Projection.



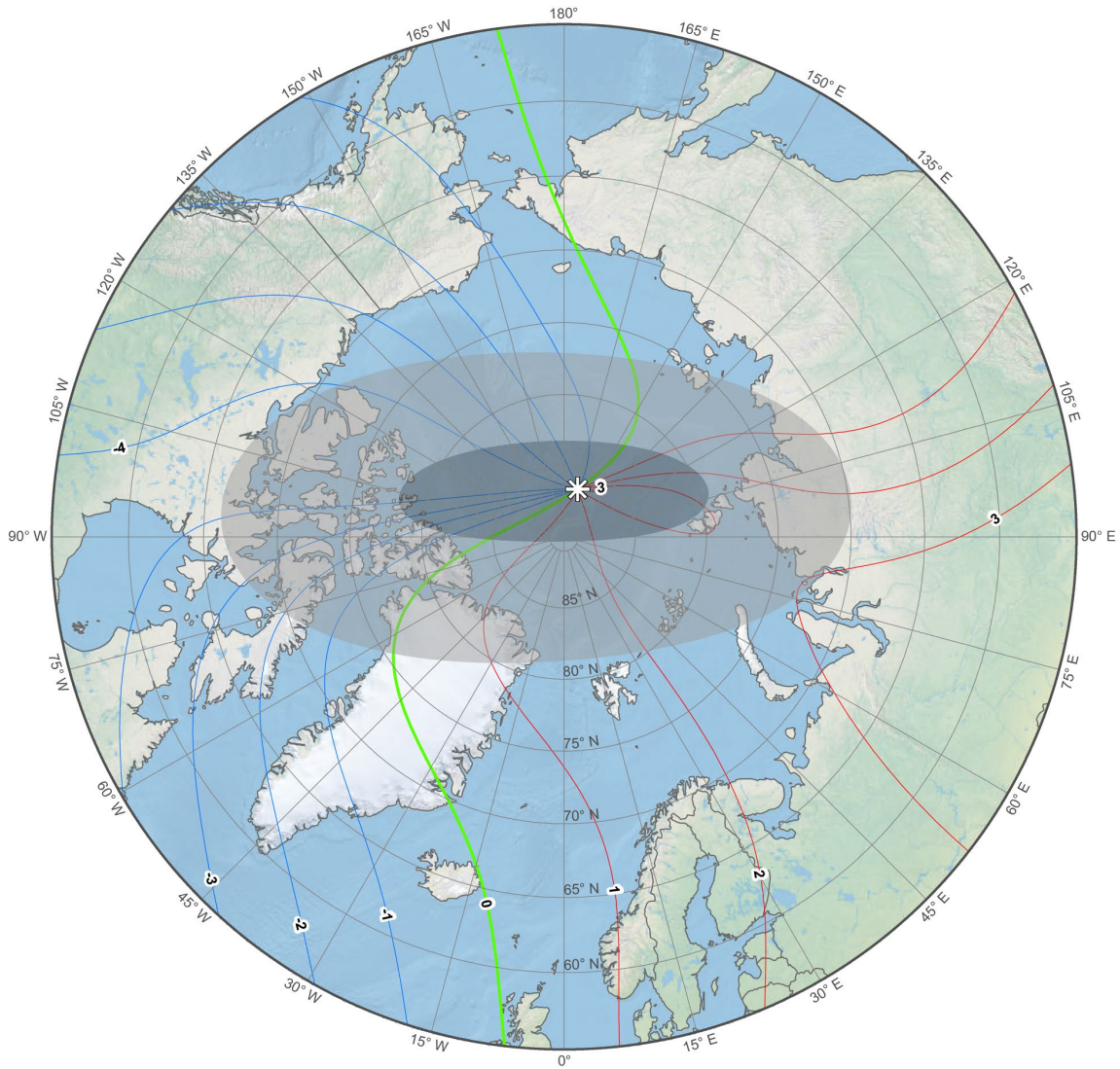
Annual change down component (Z). Contour interval is 5 nT / year, red contours positive (down) change; blue negative (up) change; green zero change. Polar Stereographic Projection.



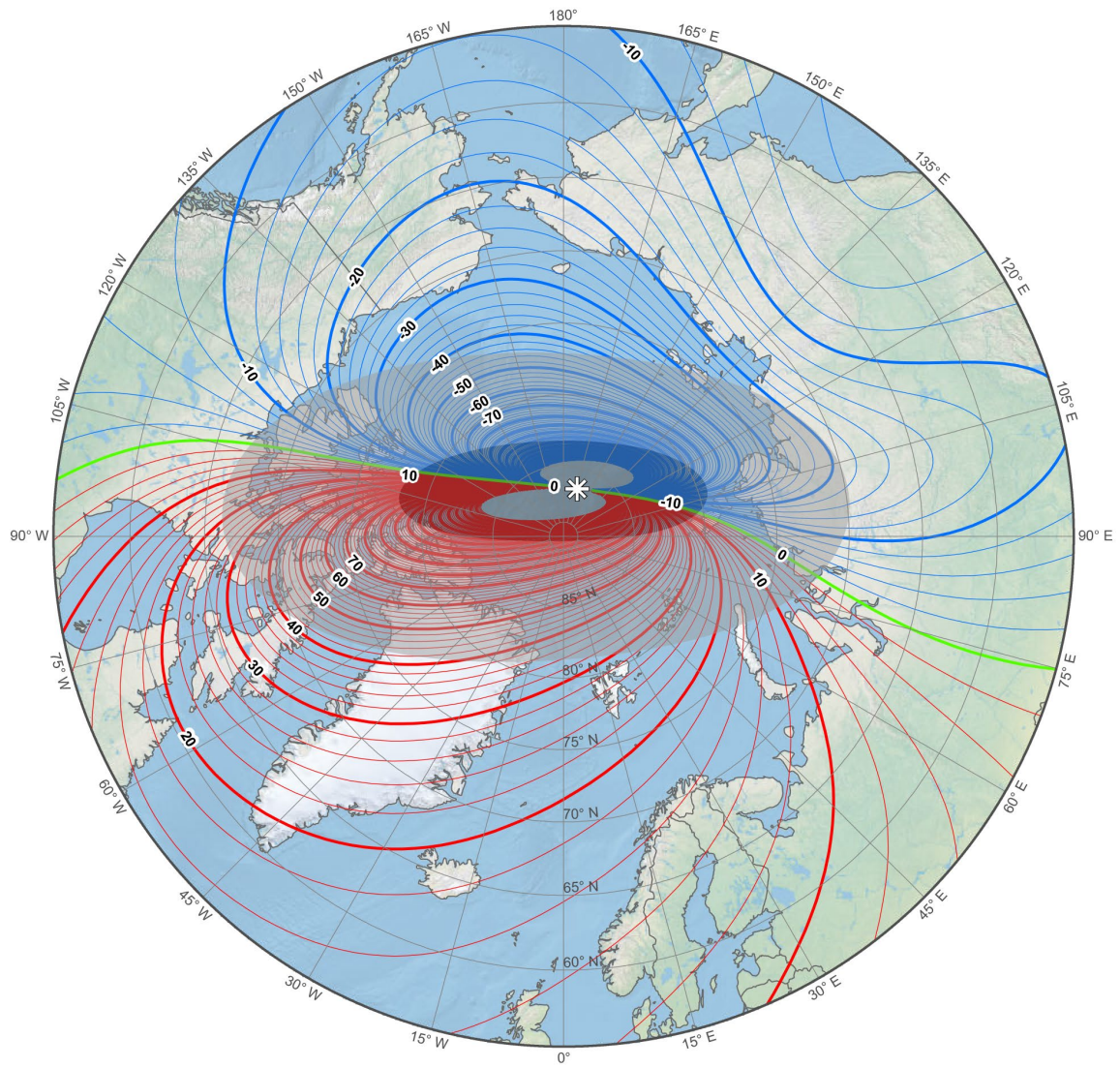
Annual change horizontal intensity (H). Contour interval is 5 nT / year, red contours positive change; blue negative change; green zero change. North Polar Region. Polar Stereographic Projection.



Annual change total intensity (F). Contour interval is 5 nT / year, red contours positive change; blue negative change; green zero change. North Polar Region. Polar Stereographic Projection.

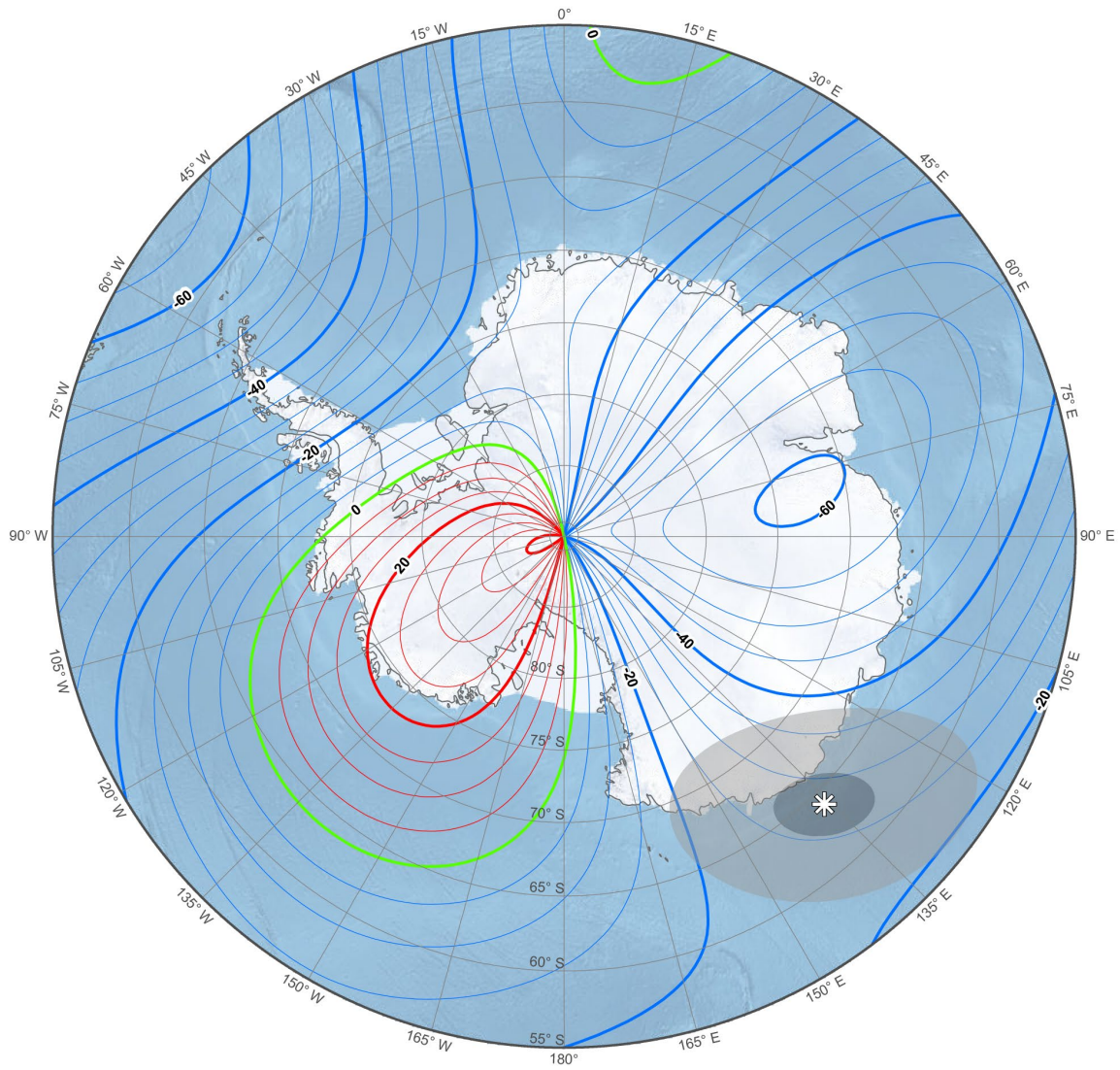


Annual change inclination (I). Contour interval is 1 arc-minute / year, red contours positive (downward) change; blue negative (upward) change; green zero change. North Polar Region. Polar Stereographic Projection.

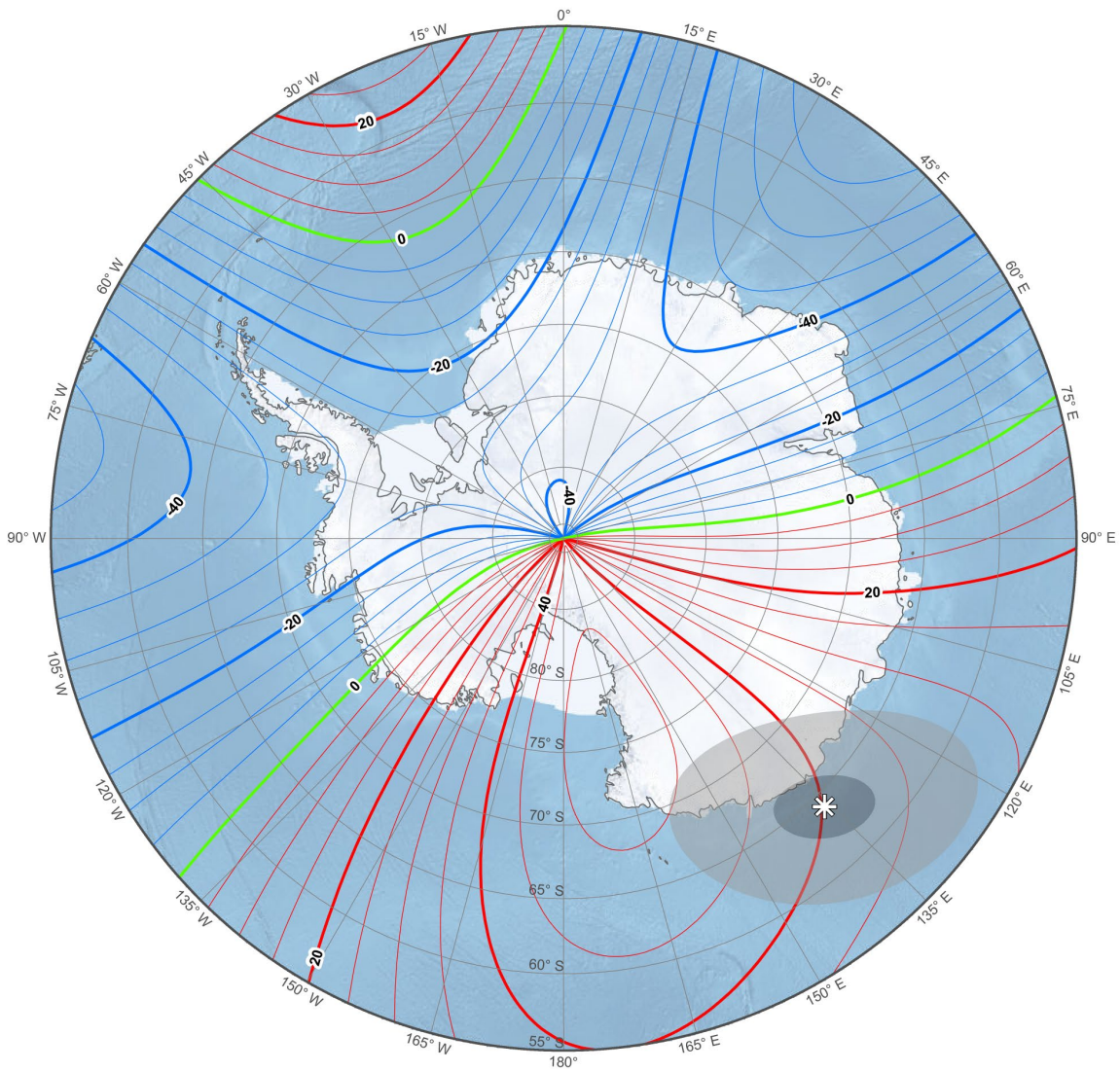


Annual change declination (D). Contour interval is 2 arc-minutes / year, red contours positive (clockwise) change; blue negative (counter- clockwise) change; green zero change. North Polar Region. Polar Stereographic Projection.

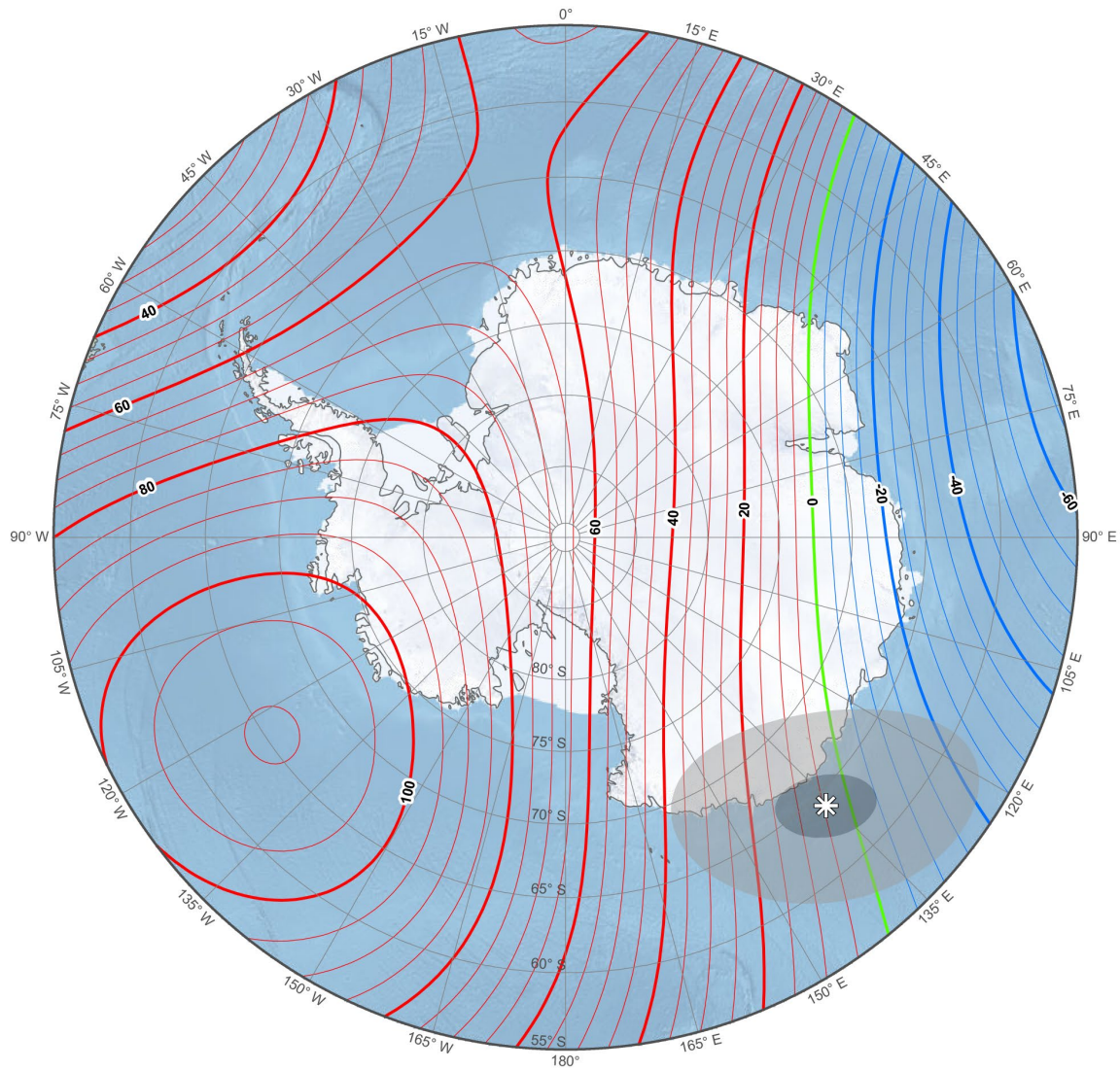
SECULAR VARIATION MAPS: SOUTH POLAR STEREOGRAPHIC PROJECTION



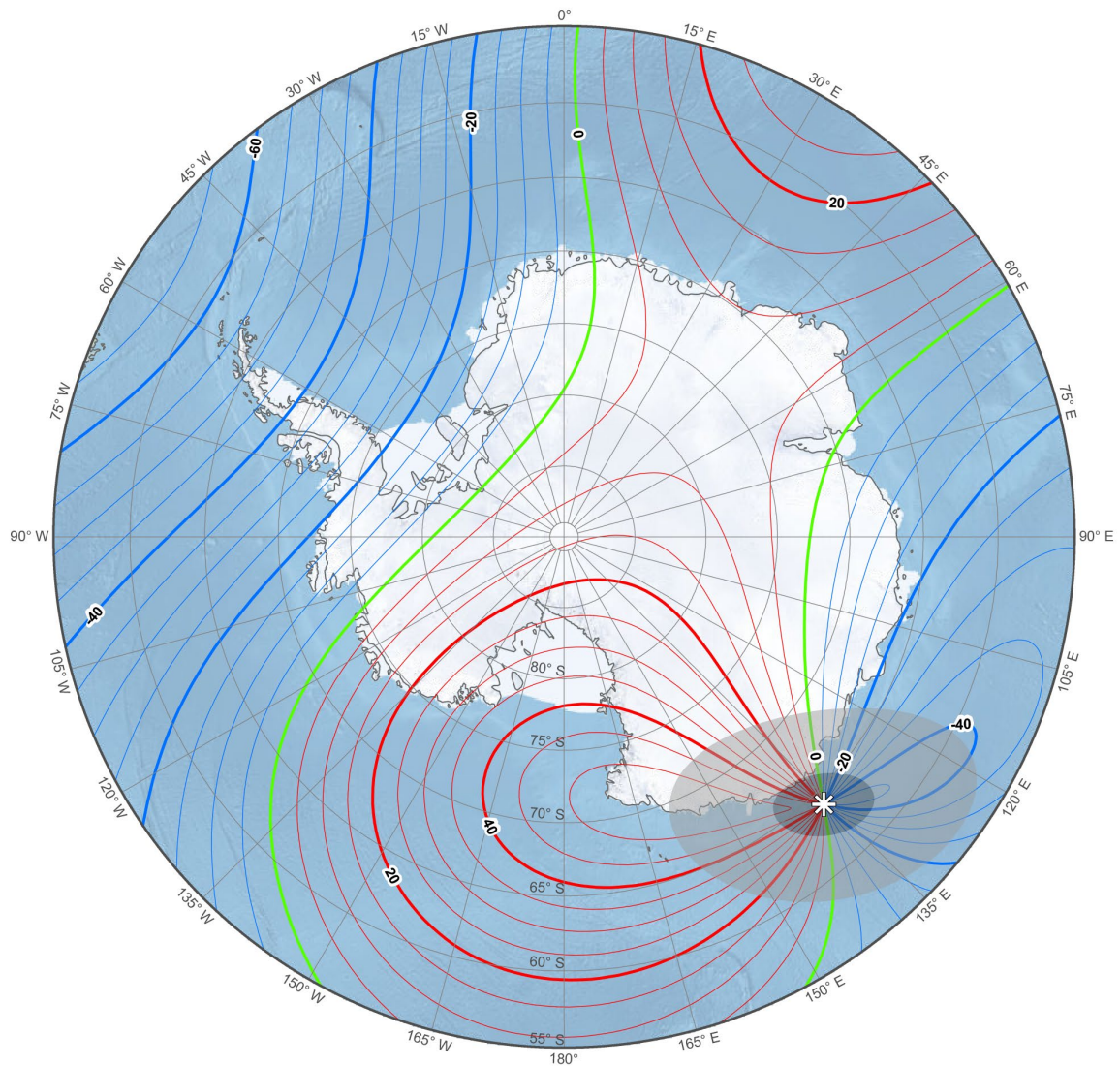
Annual change north component (X). Contour interval is 5 nT / year, red contours positive (north) change; blue negative (south) change; green zero change. South Polar Region. Polar Stereographic Projection.



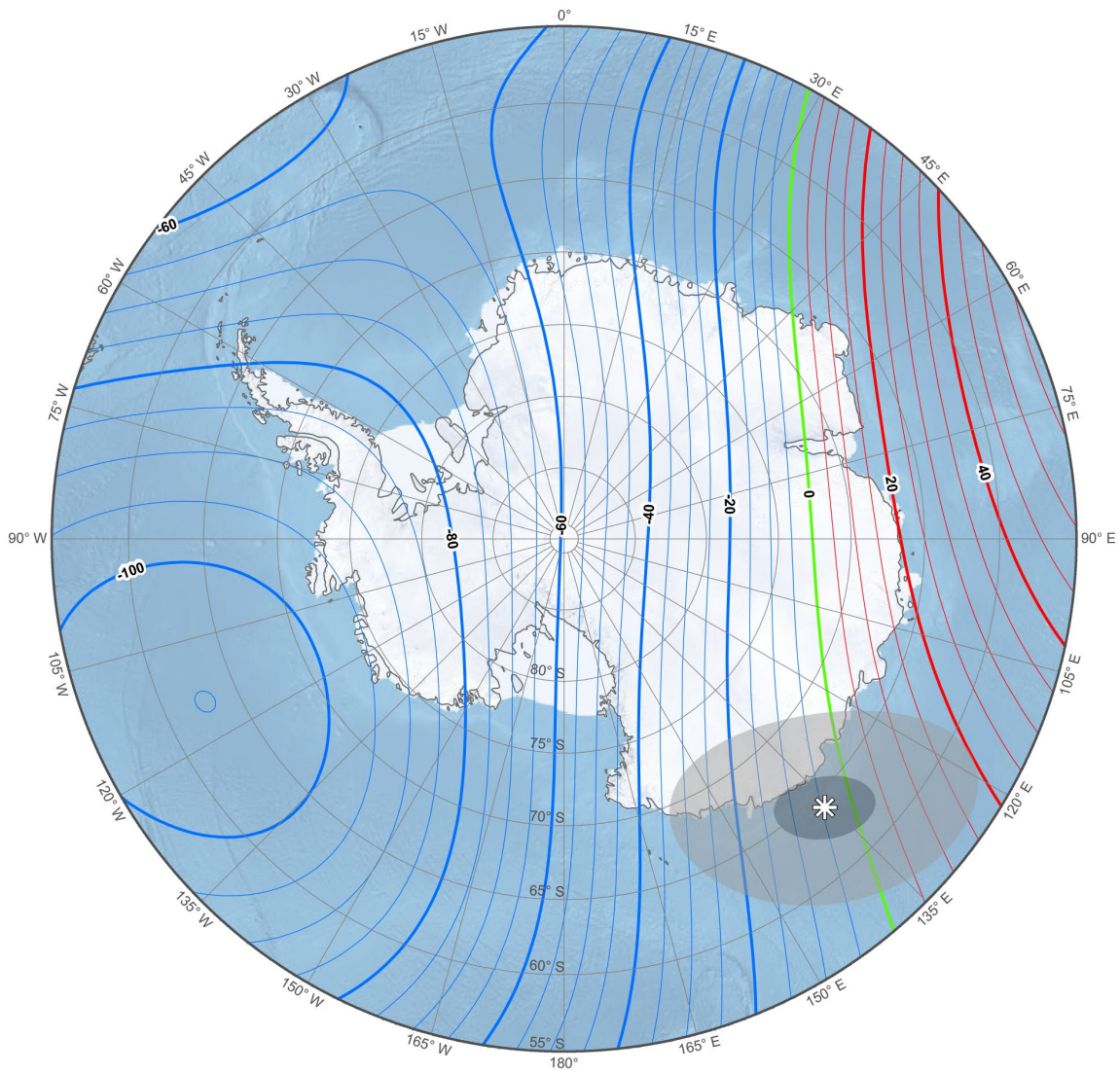
Annual change east component (Y). Contour interval is 5 nT / year, red contours positive (east) change; blue negative (west) change; green zero change. South Polar Region. Polar Stereographic Projection.



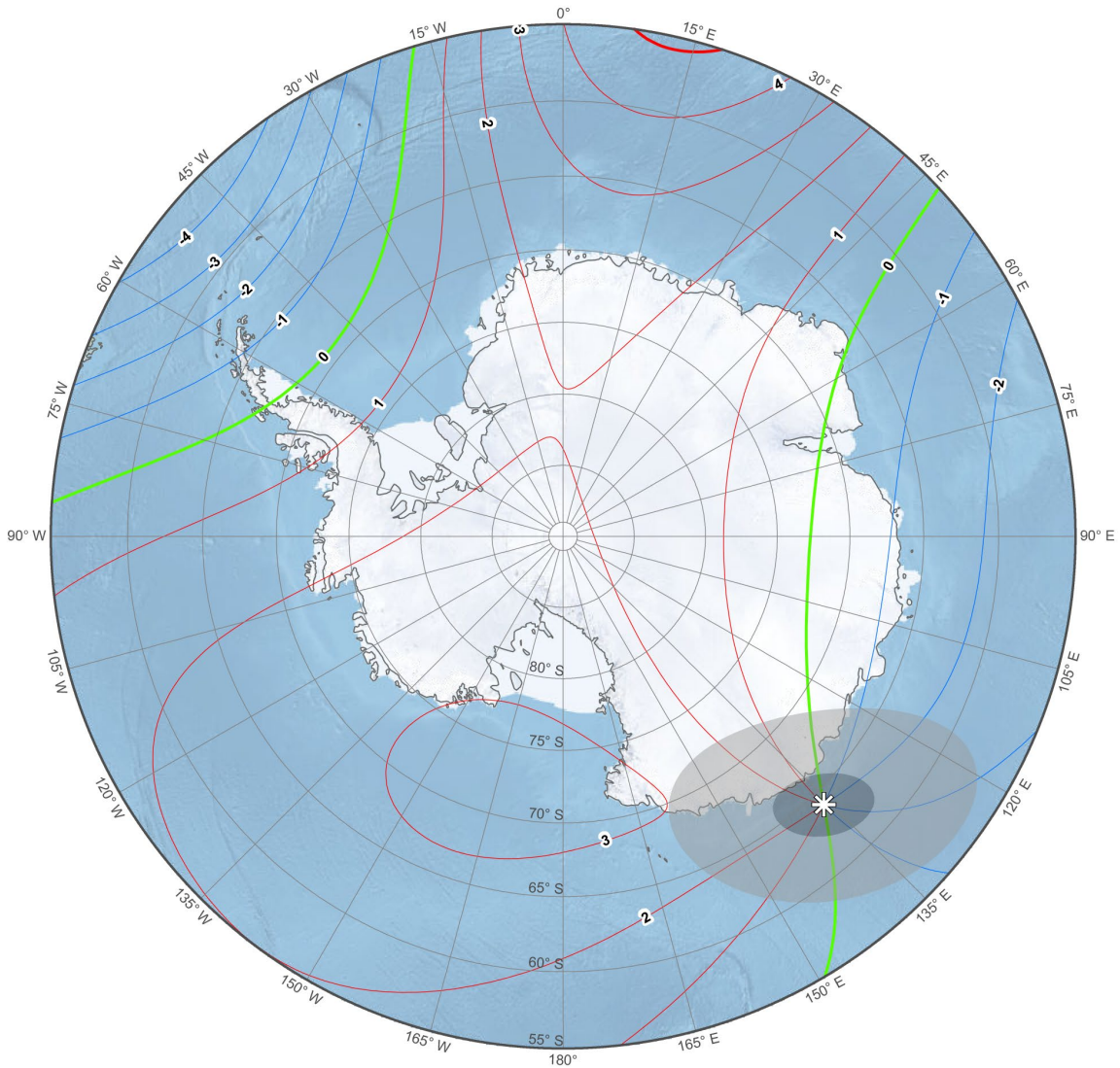
Annual change down component (Z). Contour interval is 5 nT / year, red contours positive (down) change; blue negative (up) change; green zero change. South Polar Region. Polar Stereographic Projection.



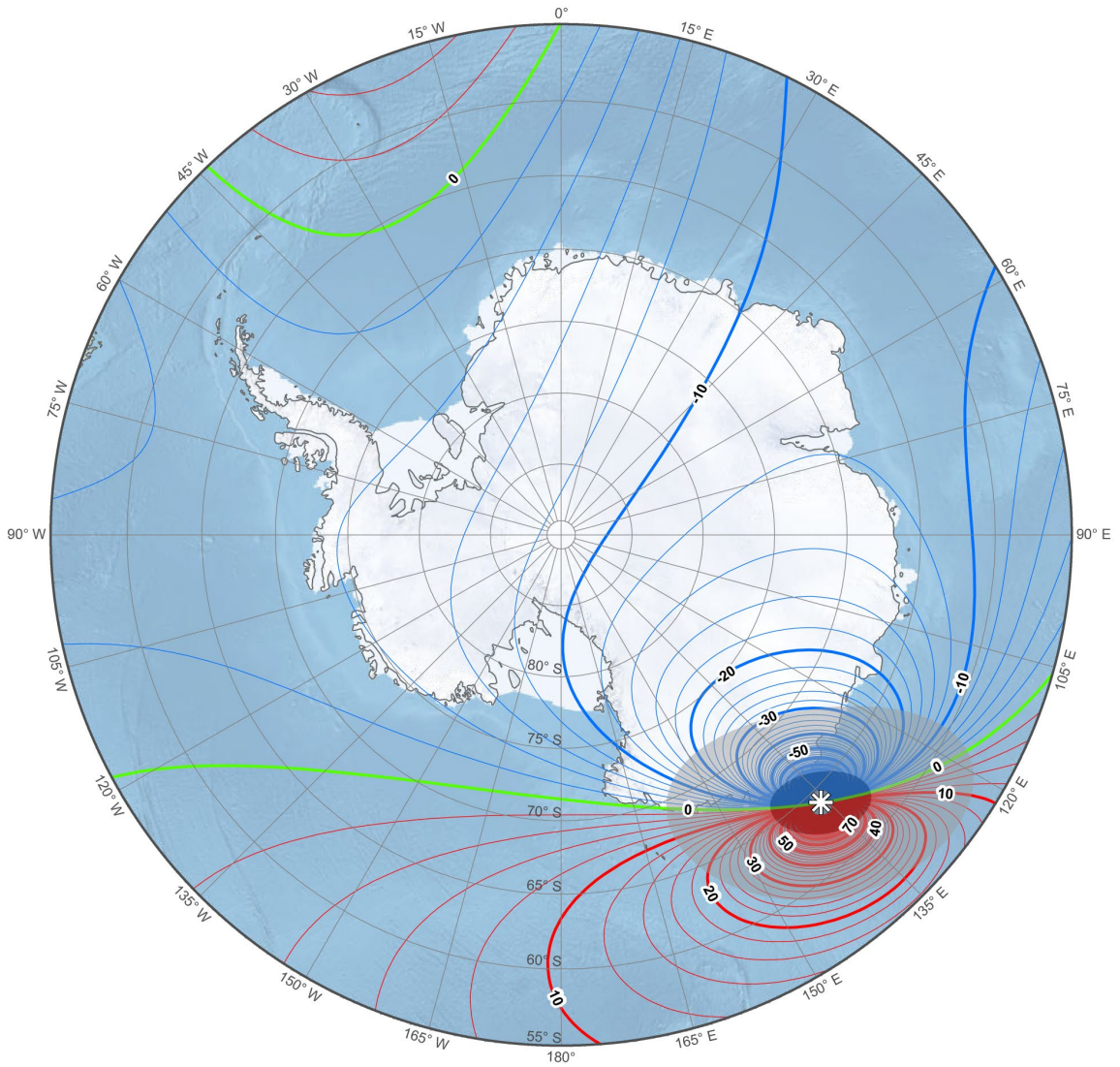
Annual change horizontal intensity (H). Contour interval is 5 nT / year, red contours positive change; blue negative change; green zero change. South Polar Region. Polar Stereographic Projection.



Annual change total intensity (F). Contour interval is 5 nT / year, red contours positive change; blue negative change; green zero change. South Polar Region. Polar Stereographic Projection.

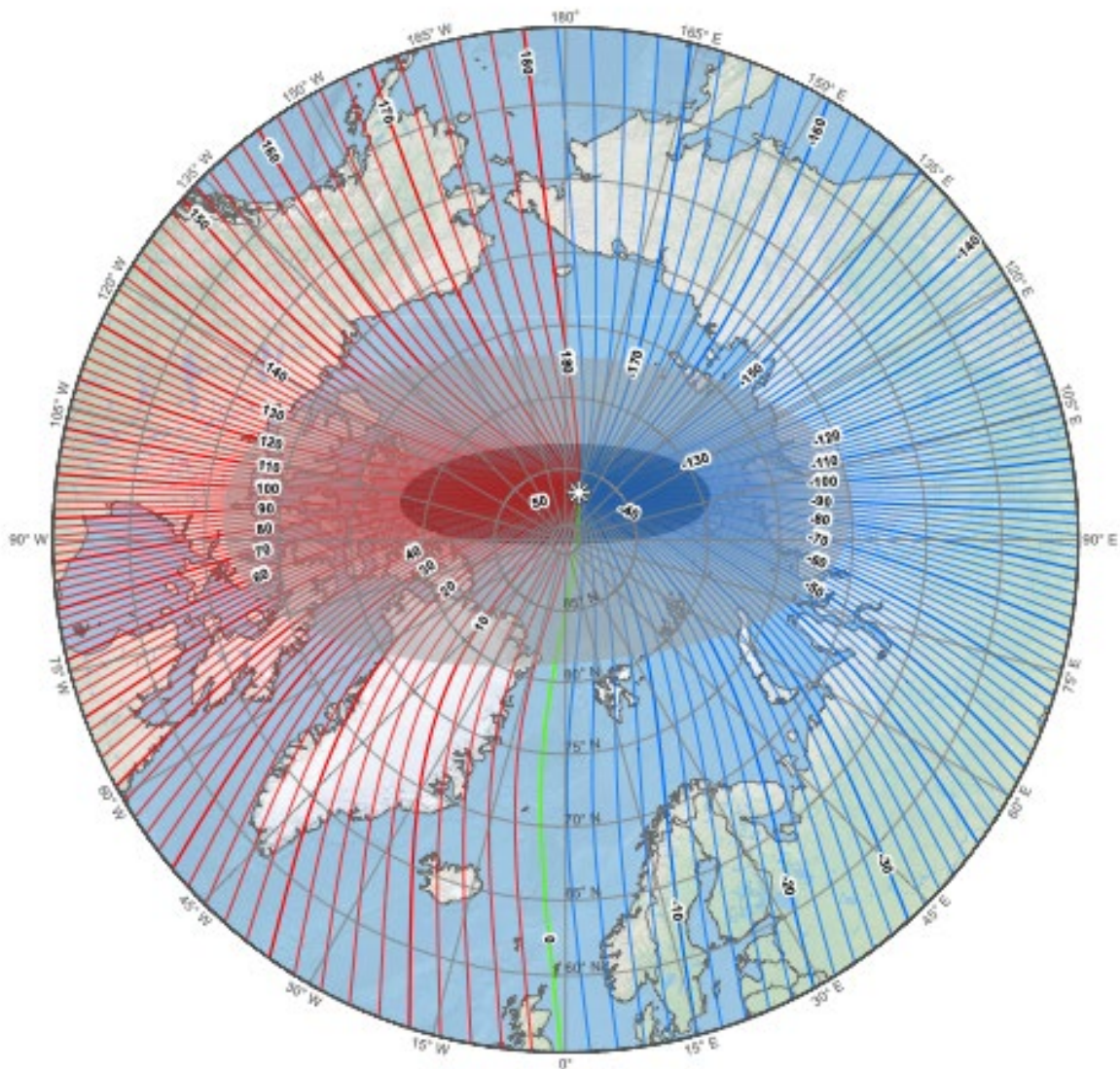


Annual change inclination (I). Contour interval is 1 arc-minute / year, red contours positive (downward) change; blue negative (upward) change; green zero change. South Polar Region. Polar Stereographic Projection.

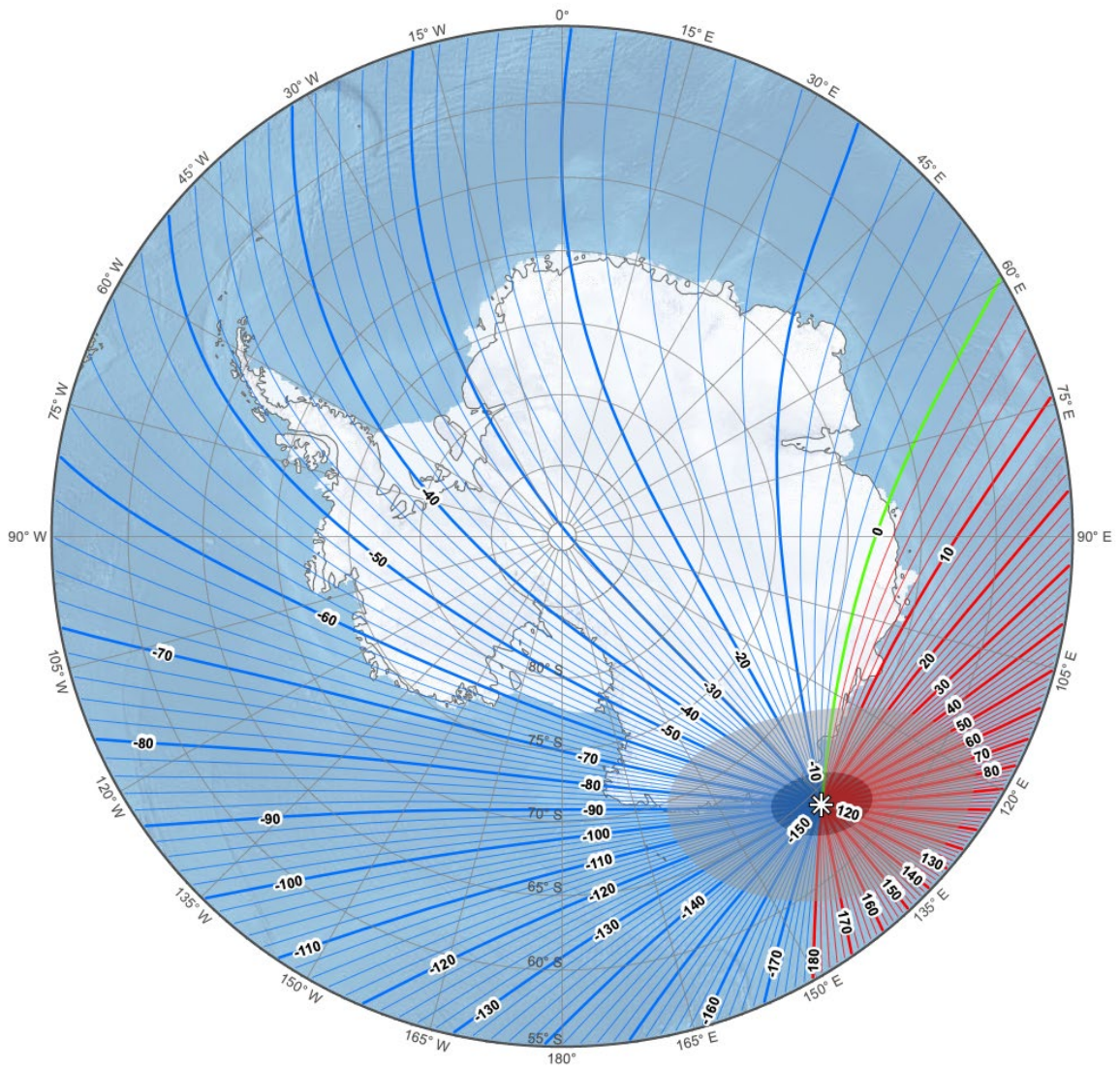


Annual change declination (D). Contour interval is 2 arc-minutes / year, red contours positive (clockwise) change; blue negative (counter-clockwise) change; green zero change. South Polar Region. Polar Stereographic Projection.

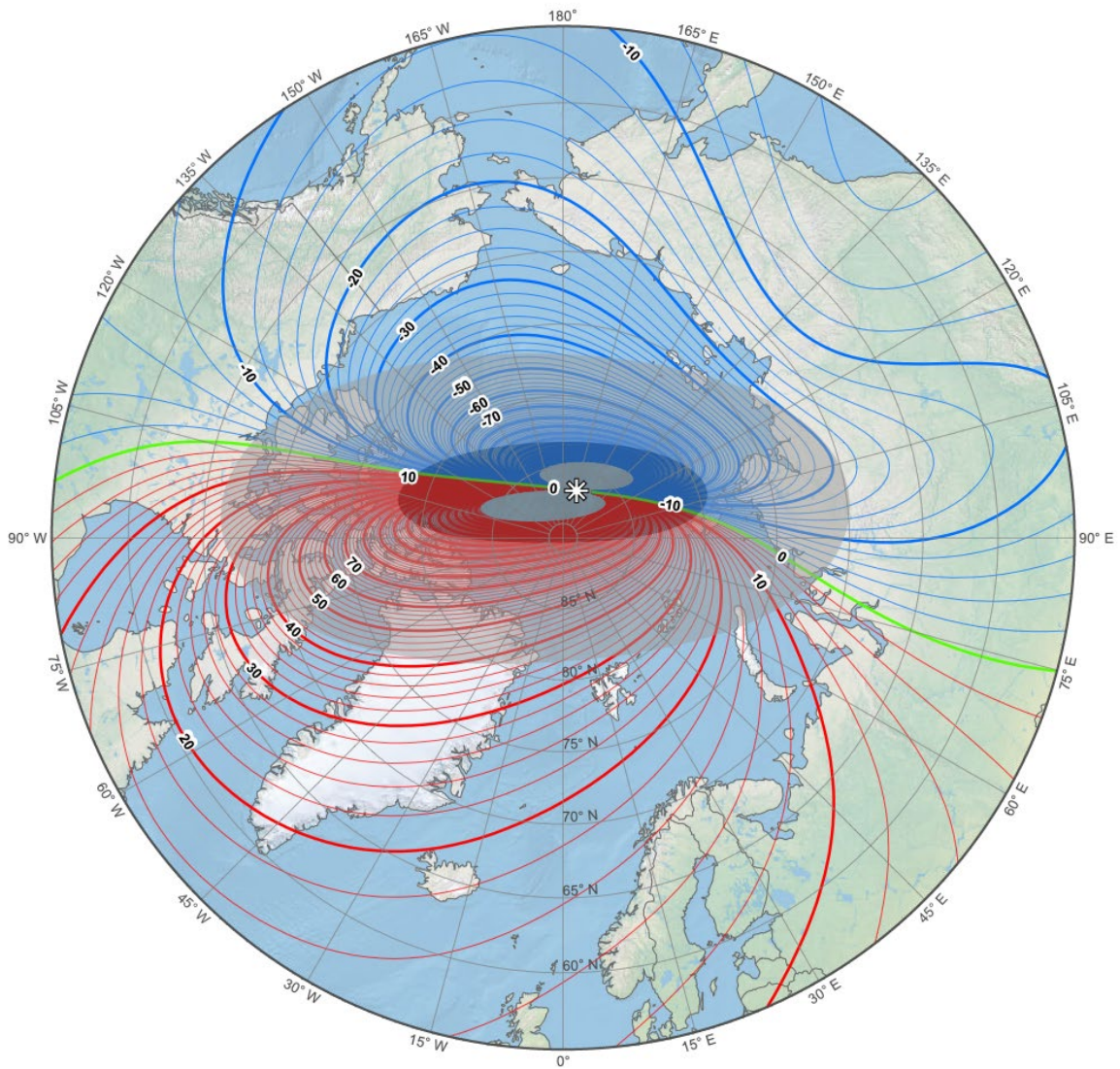
GRID VARIATION MAPS: POLAR STEREOGRAPHIC PROJECTION



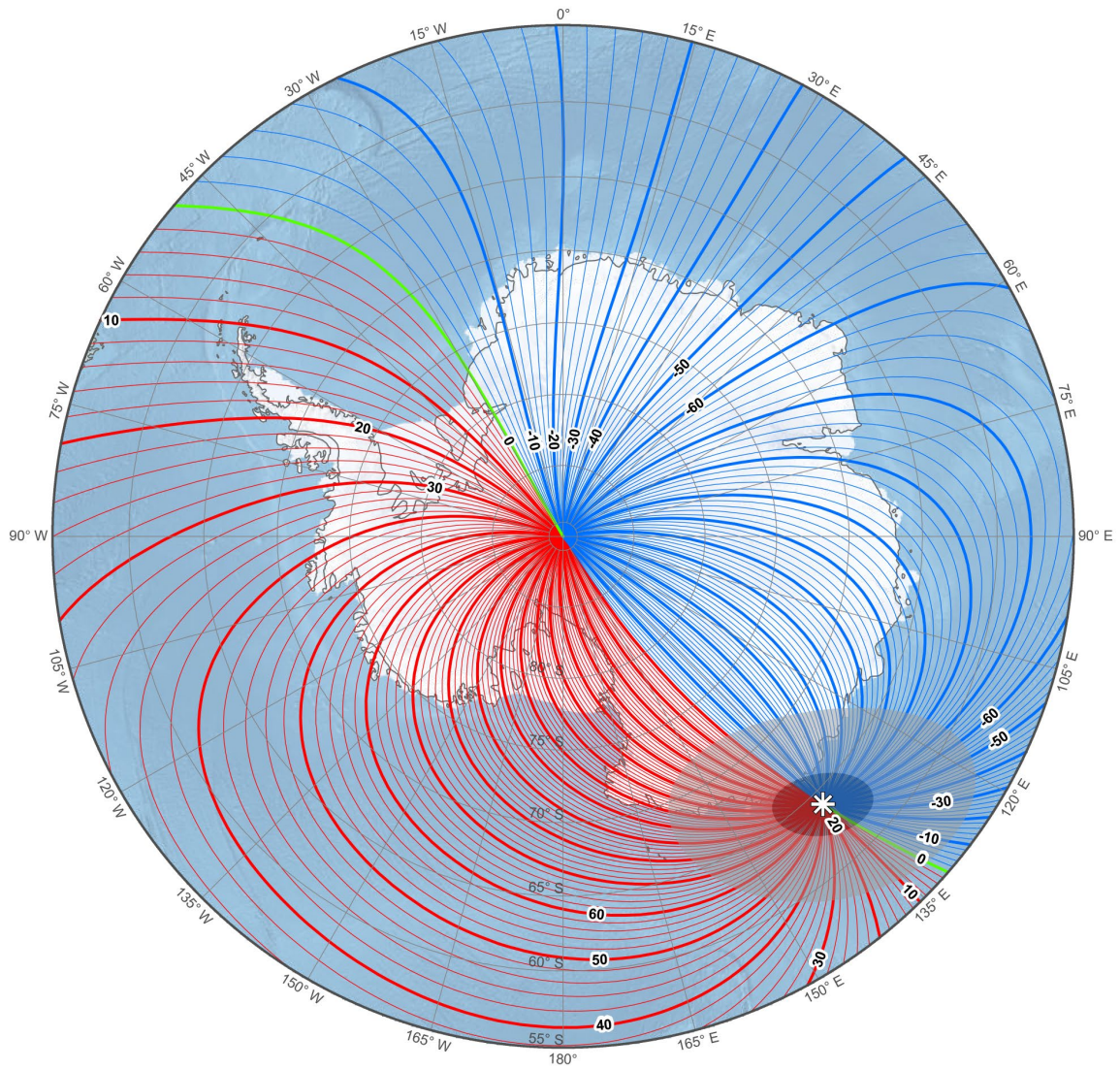
Main field grid variation (GV). Contour interval is 2 degrees, red contours positive; blue negative; green zero line.
North Polar Region. Polar Stereographic Projection.



Main field grid variation (GV). Contour interval is 2 degrees, red contours positive; blue negative; green zero line. South Polar Region. Polar Stereographic Projection.

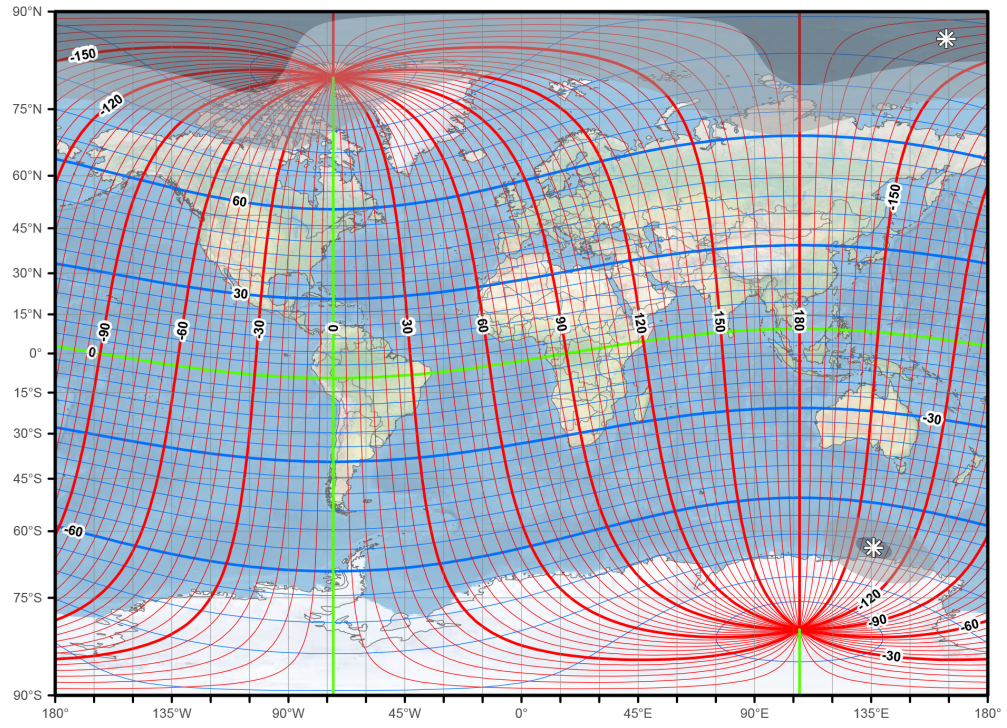


Annual change grid variation (GV). Contour interval is 2 arc-minutes / year, red contours positive (clockwise); blue negative (counter-clockwise); green zero line. North Polar Region. Polar Stereographic Projection.



Annual change grid variation (GV). Contour interval is 2 arc-minutes / year, red contours positive (clockwise); blue negative (counter-clockwise); green zero line. South Polar Region. Polar Stereographic Projection.

GEOMAGNETIC LONGITUDE AND LATITUDE



Geomagnetic longitude and latitude. Miller projection.

5. REFERENCES AND BIBLIOGRAPHY

- Abramowitz, M. and I.A. Stegun, 1972. *Handbook of Mathematical Functions with Formulas, Graphs, and Mathematical Tables*. Washington, D.C.: U.S. Dept. of Commerce, National Bureau of Standards.
- Alken, P., S. Maus, H. Lühr, R.J. Redmon, F. Rich, B. Bowman and S.M. O'Malley, 2014. Geomagnetic main field modeling with DMSP. *J. Geophys. Res. Space Physics*, 119, 4010-4025. [doi:10.1002/2013JA019754](https://doi.org/10.1002/2013JA019754)
- Alken, P., S. Maus, A. Chulliat and C. Manoj, 2015. NOAA/NGDC Candidate Models for the 12th generation International Geomagnetic Reference Field. *Earth Planets Space*, 67:68. [doi:10.1186/s40623-015-0215-1](https://doi.org/10.1186/s40623-015-0215-1)
- Aubert, J. and C.C. Finlay, 2019. Geomagnetic jerks and rapid hydromagnetic waves focusing at Earth's core surface. *Nat. Geosci.*, 12, 393-398. [doi:10.1038/s41561-019-0355-1](https://doi.org/10.1038/s41561-019-0355-1)
- Backus, G., R.L. Parker and C. Constable, 1996. *Foundations of Geomagnetism*. Cambridge (UK): Cambridge University Press.
- Brauer, P., J.M.G. Merayo, O.V. Nielsen, F. Primdahl, J.R. Petersen, 1997. Transverse field effect in fluxgate sensors. *Sensors and Actuators A*, 59, 70-74. [doi:10.1016/S0924-4247\(97\)01416-7](https://doi.org/10.1016/S0924-4247(97)01416-7)
- Brown, W.J., J.E. Mound and P.W. Livermore, 2013. Jerks abound: An analysis of geomagnetic observatory data from 1957 to 2008. *Phys. Earth Planet. Inter.*, 22, 62-76. [doi:10.1016/j.pepi.2013.06.001](https://doi.org/10.1016/j.pepi.2013.06.001)
- Chulliat, A. and S. Maus, 2014. Geomagnetic secular acceleration, jerks, and a localized standing wave at the core surface from 2000 to 2010. *J. Geophys. Res.*, 119, 1531-1543. [doi:10.1002/2013JB010604](https://doi.org/10.1002/2013JB010604)
- Chulliat, A., S. Macmillan, P. Alken, C. Beggan, M. Nair, B. Hamilton, A. Woods, V. Ridley, S. Maus and A. Thomson, 2015. *The US/UK World Magnetic Model for 2015-2020: Technical Report*, National Geophysical Data Center, NOAA. [doi:10.7289/V5TB14V7](https://doi.org/10.7289/V5TB14V7)
- Chulliat, A., J. Matzka, A. Masson and S.E. Milan, 2017. Key Ground-Based and Space-Based Assets to Disentangle Magnetic Field Sources in the Earth's Environment. *Space Sci. Rev.*, 206, 123-156. [doi:10.1007/s11214-016-0291-y](https://doi.org/10.1007/s11214-016-0291-y)
- Chulliat, A., W. Brown, P. Alken, S. Macmillan, M. Nair, C. Beggan, A. Woods, B. Hamilton, B. Meyer and R. Redmon, 2019. *Out-of-Cycle Update of the US/UK World Magnetic Model for 2015-2020: Technical Note*, National Centers for Environmental Information, NOAA. [doi:10.25921/xhr3-0t19](https://doi.org/10.25921/xhr3-0t19)
- Clarke, E., O. Baillie, S.J. Reay and C.W. Turbitt, 2013. A method for the near real-time production of quasi-definitive magnetic observatory data. *Earth Planets Space*, 65, 1363-1374. [doi:10.5047/eps.2013.10.001](https://doi.org/10.5047/eps.2013.10.001)
- Defense Mapping Agency, 1981. *Product Specifications for Global Navigation and Planning Charts*. Document PS/IAD/200.
- Department of Defense, 2019. *Performance Specification – World Magnetic Model (WMM)*. Document MIL-PRF-89500B. Retrieved from <https://assist.dla.mil/>

- Finlay, C.C., N. Olsen, S. Kotsiaros, N. Gillet and L. Tøffner-Clausen, 2016. Recent geomagnetic secular variation from Swarm and ground observatories as estimated in the CHAOS-6 geomagnetic field model. *Earth Planets Space*, 68:112. [doi:10.1186/s40623-016-0486-1](https://doi.org/10.1186/s40623-016-0486-1)
- Friis-Christensen, E., H. Lühr and G. Hulot, 2006. Swarm: A constellation to study the Earth's magnetic field. *Earth Planets Space*, 58, 351-358. [doi:10.1186/BF03351933](https://doi.org/10.1186/BF03351933)
- Gradshteyn, I.S. and I.M. Ryzhik, 1994. *Table of Integrals, Series and Products* (5th ed.). San Diego: Academic Press.
- Heiskanen, W. and H. Moritz, 1967. *Physical Geodesy*. San Francisco: W.H. Freeman and Company.
- Huber, P.J., 1996. *Robust Statistical Procedures*. Philadelphia: Society for Industrial and Applied Mathematics.
- Jankowski, J. and C. Sucksdorff, 1996. *Guide for Magnetic Measurements and Observatory Practice*. Boulder: International Association of Geomagnetism and Aeronomy. Retrieved from <http://www.iaga-aiga.org/data/uploads/pdf/guides/iaga-guide-observatories.pdf>
- Kan, J.R. and L.C. Lee, 1979. Energy coupling function and solar wind magnetosphere dynamo. *Geophys. Res. Lett.*, 6, 577–580. [doi:10.1029/GL006i007p00577](https://doi.org/10.1029/GL006i007p00577)
- Langel, R.A., 1987. The main field. In *Geomagnetism*, edited by J.A. Jacobs, Academic Press, 249-512.
- Lemoine, F.G., S.C. Kenyon, J.K. Factor, R.G. Trimmer, N.K. Pavlis, D.S. Chinn, C.M. Cox, S.M. Klosko, S.B. Luthcke, M.H. Torrence, Y.M. Wang, R.G. Williamson, E.C. Pavlis, R.H. Rapp and T.R. Olson, 1998. *The development of the joint NASA GSFC and NIMA Geopotential Model EGM96*. Technical Report NASA/TP-1998-206861, NASA Goddard Space Flight Center, Greenbelt, Maryland.
- Lesur, V., M. Hamoudi, Y. Choi, J. Dymant and E. Thebault, 2016. Building the second version of the World Digital Magnetic Anomaly Map (WDMAM). *Earth Planets Space*, 68, 27. [doi:10.1186/s40623-016-0404-6](https://doi.org/10.1186/s40623-016-0404-6)
- Lühr, H. and S. Maus, 2010. Solar cycle dependence of quiet-time magnetospheric currents and a model of their near-Earth magnetic fields. *Earth Planets Space*, 62, 843-848. [doi:10.5047/eps.2010.07.012](https://doi.org/10.5047/eps.2010.07.012)
- Macmillan, S., 2007. Observatories, Overview. In *Encyclopedia of Geomagnetism and Paleomagnetism*, edited by D. Gubbins and E. Herrero-Bervera, Springer, 708-711.
- Macmillan, S. and N. Olsen, 2013. Observatory data and the Swarm mission. *Earth Planets Space*, 65, 1355-1362. [doi:10.5047/eps.2013.07.011](https://doi.org/10.5047/eps.2013.07.011)
- Maus, S. and P. Weidelt, 2004. Separating magnetospheric disturbance magnetic field into external and transient internal contributions using 1D conductivity model of the Earth. *Geophys. Res. Lett.*, 31, L12614. [doi:10.1029/2004GL020232](https://doi.org/10.1029/2004GL020232)
- Maus, S. and H. Lühr, 2005. Signature of the quiet-time magnetospheric magnetic field and its electromagnetic induction in the rotating Earth. *Geophys. J. Int.*, 162, 755-763. [doi:10.1111/j.1365-246X.2005.02691.x](https://doi.org/10.1111/j.1365-246X.2005.02691.x)
- Maus, S., F. Yin, H. Lühr, C. Manoj, M. Rother, J. Rauberg, I. Michaelis, C. Stolle and R. D. Müller, 2008. Resolution of direction of oceanic magnetic lineations by the sixth-generation lithospheric magnetic field model from CHAMP satellite magnetic measurements. *Geochem. Geophys. Geosyst.*, 9, Q07021. [doi:10.1029/2008GC001949](https://doi.org/10.1029/2008GC001949)

- Maus, S. et al., 2009. EMAG2: A 2-arc min resolution Earth Magnetic Anomaly Grid compiled from satellite, airborne, and marine magnetic measurements. *Geochem. Geophys. Geosyst.*, 10, Q08005. [doi:10.1029/2009GC002471](https://doi.org/10.1029/2009GC002471)
- Meyer, B., A. Chulliat and R.W. Saltus, 2017. Derivation and Error Analysis of the Earth Magnetic Anomaly Grid at 2 Arc-Minute Resolution Version 3 (EMAG2v3), *Geochem. Geophys. Geosyst.*, 18, 4522-4537. [doi:10.1002/2017GC007280](https://doi.org/10.1002/2017GC007280)
- Merrill, R.T., M.W. McElhinny and P.L. McFadden, 1996. *The Magnetic Field of the Earth: Paleomagnetism, the Core and the Deep Mantle*. San Diego: Academic Press.
- NATO Standardization Agency, 2011. *STANAG 7172 Use of Geomagnetic Models* (2nd ed).
- Newell, P.T., T. Sotirelis, K. Liou, C.-I. Meng and F.J. Rich, 2007. A nearly universal solar wind-magnetosphere coupling function inferred from 10 magnetospheric state variables, *J. Geophys. Res.*, 112(A1). [doi:10.1029/2006JA012015](https://doi.org/10.1029/2006JA012015)
- Newitt, L., A. Chulliat and J.-J. Orgeval, 2009. Location of the North Magnetic Pole in April 2007. *Earth Planets Space*, 61, 703-710. [doi:10.1186/BF03353178](https://doi.org/10.1186/BF03353178)
- Olsen, N., L. Tøffner-Clausen, T.J. Sabaka, P. Brauer, J.M.G. Merayo, J.L. Jørgensen, J.-M. L ger, O.V. Nielsen, F. Primdahl and T. Risbo, 2003. Calibration of the Ørsted vector magnetometer. *Earth Planets and Space*, 55, 11-18. [doi:10.1186/BF03352458](https://doi.org/10.1186/BF03352458)
- Olsen, N., H. L hr, C.C. Finlay, T.J. Sabaka, I. Michaelis, J. Rauberg and L. Tøffner-Clausen, 2014. The CHAOS-4 geomagnetic field model. *Geophys. J. Int.*, 197, 815-827. [doi:10.1093/gji/ggu033](https://doi.org/10.1093/gji/ggu033)
- Parkinson, W.D., 1983. *Introduction to Geomagnetism*. Edinburgh: Scottish Academic Press.
- Peltier, A. and A. Chulliat, 2010. On the feasibility of promptly producing quasi-definitive magnetic observatory data. *Earth Planets Space*, 62, e5-e8. [doi:10.5047/eps.2010.02.002](https://doi.org/10.5047/eps.2010.02.002)
- Sugiura, M., 1964. Hourly values of the equatorial Dst for the IGY. *Ann. Int. Geophys. Yr.*, 35, 9-45.
- Thomson, A.W.P. and V. Lesur, 2007. An improved geomagnetic data selection algorithm for global geomagnetic field modelling. *Geophys. J. Int.*, 169, 951-963. [doi:10.1111/j.1365-246X.2007.03354.x](https://doi.org/10.1111/j.1365-246X.2007.03354.x)
- Thomson, A.W.P., B. Hamilton, S. Macmillan and S.J. Reay, 2010. A novel weighting method for satellite magnetic data and a new global magnetic field model. *Geophys. J. Int.*, 181, 250-260. [doi:10.1111/j.1365-246X.2010.04510.x](https://doi.org/10.1111/j.1365-246X.2010.04510.x)
- Tøffner-Clausen, L., V. Lesur, N. Olsen and C. C. Finlay, 2016. In-flight scalar calibration and characterisation of the Swarm magnetometry package. *Earth Planets Space*, 68:129. [doi:10.1186/s40623-016-0501-6](https://doi.org/10.1186/s40623-016-0501-6)